Blue-laser excitation studies of ZnO thin films and rare-earth doped ZnO powders

Nkosiphile Andile Bhebhe

A dissertation submitted to the Faculty of Science, University of the Witwatersrand, Johannesburg, in fulfillment of the academic requirements for the degree of Master of Science.

Johannesburg, March 2016

Declaration

I declare that the analysis and results presented here are my original work and was carried under the guidance of Dr. M. Mujaji (supervisor) and Dr. D. Wamwangi (co-supervisor). The use of other sources in this work has been duly acknowledged.

This dissertation is being submitted for a Master of Science at the University of the Witwatersrand, Johannesburg and has not been submitted before for any degree or examination at any other University.

_____

Nkosiphile Andile Bhebhe

(Signature of candidate)

8th day of August 2016

Abstract

Zinc oxide (ZnO) continues to receive widespread attention due to its excellent optical and electronic properties; it demonstrates the combined characteristics of high transmittance and electrical conductivity. Despite the tremendous drive for its application in optoelectronic devices, the full nature of the point defects and defect complexes have not been characterised comprehensively. In this work, luminescence characteristics of the intrinsic defects in ZnO thin films and the rare-earth ions Eu^{3+} and Tb^{3+} in ZnO powders are investigated under blue-laser excitation.

The thin films used in this study were deposited using the radio-frequency magnetron sputtering method over a 2 hour duration under varied power and substrate bias conditions. The powders were synthesized by the chemical bath deposition method with dopant concentrations of 1.0 mol%. Grazing incidence X-ray diffraction (XRD) was used to determine the lattice properties of the samples. Photoluminescence studies were primarily conducted at room temperature (300 K) with the 457.9 nm, 476.5 nm and 488.0 nm laser lines as excitation sources.

For the ZnO thin films, XRD patterns of a hexagonal wurtzite structure with a *c/a* ratio of about 1.60 and a *u*-parameter of 0.38 were obtained. Photoluminescence measurements show a broad emission band in the 500.0-900.0 nm range, centred at 656.0 nm. Annealed films yielded relatively more intense photoluminescence spectra than the as-prepared films. The intrinsic point defects and defect level transitions responsible for the broad emission are discussed.

For the ZnO powders, the XRD patterns of the annealed samples of pristine ZnO, ZnO:Eu^{3+} and ZnO:Tb^{3+} are similarly consistent with a hexagonal wurtzite ZnO phase. Energy dispersive spectroscopy (EDS) confirmed the presence of the Eu^{3+} and Tb^{3+} dopants in the respective ZnO host while scanning electron microscopy (SEM) measurements showed the morphology of the sample powders. Photoluminescence spectra of pelletized samples, obtained in the 460.0-900.0 nm range, exhibit relatively intense Eu^{3+} and Tb^{3+} emission bands superimposed on a broad emission background. The RE^{3+} emission bands are

attributed to the $^5D_0 \rightarrow {}^7F_J$ (J = 0, 1, 2, 3, 4) and the $^5D_4 \rightarrow {}^7F_J$ (J = 0, 1, 2, 3, 4, 5, 6) electronic transitions of Eu^{3+} and Tb^{3+}, respectively, while the background emission is attributed to intrinsic defects. Crystal-field energy levels for the Eu^{3+} ion and the Tb^{3+} ion occupying a C_{3v} symmetry site were deduced from fitting Gaussian curves to the RE^{3+} emission bands. Possible channels for transfer of energy from the intrinsic defects to Eu^{3+} and Tb^{3+} are discussed.

This dissertation is dedicated to my parents…

Onesmus Bhebhe and Bertha Bhebhe

I am forever grateful for your unconditional love and support.

eNzinda, M'zi'mkhulu, Maziwa yi Nkosi abanye bengaziwa!!!

Acknowledgements

The completion of this dissertation is a result of the contributions by many interested individuals. As such I would like to first and foremost express my sincere gratitude to my supervisors, Dr. M. Mujaji and Dr. D. Wamwangi, for their continued guidance throughout this research project, the time they put into the much needed consultations, their expertise and experience as well as their constructive feedback from reading through the drafts of this dissertation. I thank you for your encouragement and support towards my academic development.

I would also like to express my gratitude to:

- Mr. C. Sandrock, Mr. J. Augustine, Mr. L. Mafemba, Mr. V. Govender and other School of Physics workshop staff for their technical contribution to this work.
- Prof. F. B. Dejene and Dr. L. F. Koao from the Department of Physics, at the University of the Free State, Qwaqwa campus for the collaboration in synthesizing the rare-earth doped zinc oxide powders.
- Prof. D. Billing and the School of Chemistry, at the University of the Witwatersrand for granting access to the X-ray diffraction facility.
- Prof. A. Ziegler for granting access to the microscopy and micro-analysis unit in the School of Molecular and Cell Biology, at the University of the Witwatersrand and Mr. J. Gerber for his assistance and training on how to use the scanning electron microscopy and energy dispersive spectroscopy instrument.
- Prof. D. Naidoo for allowing access to the hydraulic press and to Mr. G. Peter and Mr. M. Ncube who assisted with the pressing of the zinc oxides powders into pellets.
- Mr T. Mashego for his assistance with the cutting of the quartz substrates into the required sizes for thin film deposition.
- A special thanks to Dr. H. Masenda, Mr. R. McIntsosh, Miss. S. Ncube and Mr. K. Jakata for their valuable suggestions in the draft version of the dissertation. Thanks to my fellow students, friends and family: Bukani,

Adeleke, Sav, Wilfred, Mncedisi, Emmaculate, Mbongeni, Yola, Nkosinathi, Nyasha, Samukele, Mthabisi, Hlengiwe, Stephen, Sikhu, Mzi, Gugu and Anele for their encouragement and support during my studies.

- Financial support from the DST-NRF Centre of Excellence in Strong Materials (CoE-SM) and the University of the Witwatersrand, Johannesburg is gratefully acknowledged.
- The School of Physics staff for their administrative contribution towards the completion of my studies.
- Above all I would like to thank the Almighty for in Him we live, move and have our being.

Table of contents

Table of Contents

List of figures

List of tables

Chapter 1

Introduction

The ability of semiconductors to present both conducting and insulating properties make them unique candidates for optoelectronic applications. Their intrinsic and extrinsic properties have made them suitable for a number of applications which include photovoltaics [1] and solid state lighting [2]. The continued advancement in technology and science has resulted in more wear-extreme operating conditions for electronic equipment. This has driven the need for novel optoelectronic devices that can withstand thermally and chemically aggressive environments. Among the many semiconducting materials, zinc oxide (ZnO) and gallium nitride (GaN) have been identified as the prospective candidates for operation under extreme ambient. This has stimulated continued research interest in these wide bandgap semiconductors [3]. ZnO is non-toxic and is capable of withstanding high radiation environments [4]. Despite the similar structural properties of ZnO and GaN, there is more research interest in ZnO because of its superior features. These include a high melting temperature (2248 K) [5] and a higher exciton binding energy of 483 cm^{-1} (60 meV) [6], making ZnO a potential candidate for developing satellite electronic devices [4]. Bulk single ZnO crystals have been considered as a promising candidate for high temperature resistant and high power transistor devices [7]. However the growth of bulk ZnO crystals generally require high temperature and high pressure conditions as well as time-consuming procedures [5]. This has led to the use of less expensive and easy to fabricate forms of ZnO such as thin films and powders [8,9].

The development of more efficient optoelectronic devices that require only small amounts of fabrication material has stimulated research interest in thin film technology. ZnO thin films continue to be intensively investigated as possible candidates for application in devices such as light-emitting diodes [10] and laser diodes [11]. However, to efficiently utilize the properties of ZnO thin films for

optical applications, its intrinsic properties have to be clearly understood. It is therefore necessary to investigate and determine the inherent defects of ZnO which are responsible for its optical and electrical characteristics. The nature of these point defects which rely on the thin-film preparation conditions is therefore an important area of study as the ZnO optical properties are intrinsic defect dependent [12]. Variations in growth conditions such as deposition power, DC substrate bias and ambient gas may (i) improve or deteriorate the quality of a thin film and (ii) influence the electrical and optical properties of the film [13]. For example, as-grown ZnO has been linked to unintentional impurities usually from group-III elements such as aluminium, rendering ZnO its n-type semiconductor properties [14].

Powder technology has provided an alternative economical route of synthesizing semiconductor materials which enables the incorporation of dopants such as rare-earth ions (RE^{3+}) [15]. ZnO powders have been identified as suitable materials for potential laser diode development especially when doped with highly luminescent dopants such as RE^{3+} ions [16]. Having understood the inherent properties of ZnO, their relation to the incorporation of impurity dopants (RE^{3+}) still needs to be established. For this reason, studies of RE^{3+} ion doped ZnO powders are still being pursued [2,9]. The antenna approach has been particularly useful as RE^{3+} emission has been realized in ZnO:RE^{3+} with excitation wavelengths in the ultra-violet-to-visible regions [17]. In this approach, the host material (ZnO) indirectly excites the RE^{3+} ions through intrinsic defect dependent energy transfer mechanisms [18]. These native defects are briefly discussed in the next section.

1.1 Brief background

Zinc oxide has a hexagonal wurtzite structure (figure 1.1 (a)) with lattice parameters a = 3.25 Å and c = 5.21 Å [3]. It has a wide direct band gap of 3.44 eV at 10 K [19] and 3.37 eV at room temperature [20]. The direct bandgap occurs at the centre of the Brillouin zone (Γ point) as shown on the electronic band structure of ZnO in figure 1.1 (b) [21]. Common native point defects in ZnO are in the form of an atom being absent from its accustomed lattice site (Schottky defect) or an atom residing in an empty space within the lattice (Frenkel defect)

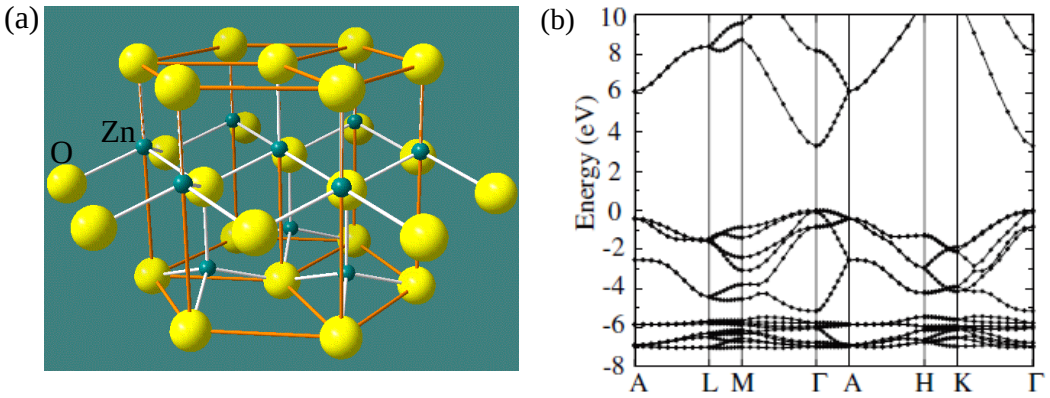

Figure 1. 1 (a) The hexagonal wurtzite structure of ZnO. (b) The band structure of ZnO [21].

or an oxygen (O^{2-} radius = 1.40 Å) taking up a zinc (Zn^{2+}radius = 0.74 Å) lattice position and vice versa (antisite) [21].

The formation of point defects results in the introduction of localized defect levels within the band gap of the semiconductor [22]. These defect levels are classified as either shallow levels or deep levels [21]. The shallow level can be either an acceptor level, when it is close to the valence band (VB); or a donor level, when the level is close to the conduction band (CB) [21]. These levels make it possible for electron-hole pairs to be generated in the material by optical excitation, using excitation energies of (2.61 eV (476.5 nm), 2.55 eV (488.0 nm) and 2.41 eV (514.5 nm)) which are well below the energy gap [23]. Vlasenko and Watkins [23] have shown that optical excitation of ZnO was possible with excitation energies ranging from the ultraviolet region up to about 2.41 eV (514.5 nm) in the visible region. Zinc vacancies (V_{Zn}), zinc interstitials (Zn_i) and oxygen vacancies (V_O) are the common native defects in ZnO due to their relatively low formation energies of 3.70 eV, 6.0 eV and 3.72 eV, respectively [12,21]. Other intrinsic defects, which include zinc antisites (Zn_O), oxygen antisites (O_{Zn}) and oxygen interstitials (O_i) occur in low concentrations due to their relatively high formation energies of 9.5 eV and 8.5 eV, respectively [21].

1.2 Problem statement

The continued search for materials that emits in the visible region, for potential solid-state laser development and for other optoelectronic device applications,

has led to the investigation of the optical properties of both undoped and rare-earth doped ZnO thin films and powders. At present, reported studies on the luminescence properties of both undoped and rare-earth doped ZnO using ultra-violet excitation include those of Eu^{3+}, Tb^{3+} and Er^{3+} doped ZnO [2,9,24]. Ultra-violet excitation provides sufficient energy to excite valence electrons to the conduction band. The observed emission comprises of [25]:

i. transitions from excitons just below the conduction band to the valence band,
ii. transitions from the conduction band to deep levels and
iii. transitions from donor states to acceptors states or the valence band.

In the literature, not much has been reported on the investigation of possible direct excitation of electrons from the valence band to defect levels within the bandgap, i.e. sub-band excitation. One plausible reason for this is that most of the reported studies are focused on the phosphorescence aspect, for which UV excitation is considered more appropriate. In this study, blue-laser excitation studies of undoped (no rare-earths) ZnO thin films will be carried out with the aim of determining the luminescence characteristics of intrinsic defects in ZnO. In addition, the effect of variations in the deposition conditions of ZnO thin films on the luminescence will be investigated. These luminescent defect level transitions will be related to the indirect excitation of the rare-earth ions through energy transfer from intrinsic defects in ZnO. Photoluminescence studies of Eu^{3+} and Tb^{3+} doped ZnO powders have also been limited to ultra-violet excitation and visible region emission. These emissions are essential for white light production in solid state lighting at low operating powers, i.e. for phosphors. As such, visible region excitation and visible region emission still requires extensive investigation. Furthermore, crystal-field energy levels of Eu^{3+} ions and Tb^{3+} ions in ZnO powders have not been reported previously. The specific objectives are presented in the next section.

1.3 Study objectives

From the previously discussed problem statement, the main objectives of this project are as follows:

- To investigate the visible luminescence properties of undoped ZnO thin films deposited by the radio-frequency (rf) magnetron sputtering method using blue-laser excitation.
- To determine the effect of the thin-film deposition variables such as deposition power, dc voltage biasing, argon/nitrogen gas flow and post-deposition annealing on the photoluminescence properties of ZnO thin films.
- To determine the visible region emission bands of Eu^{3+} and Tb^{3+} ions in ZnO powders synthesized by the chemical bath deposition method using blue-laser excitation.
- To deduce the crystal-field energy level schemes for Eu^{3+} and for Tb^{3+} ions in ZnO.

1.4 Dissertation outline

This research project will focus on investigating the luminescence properties of undoped ZnO thin films and rare-earth doped ZnO powders synthesized by radio-frequency magnetron sputtering and the chemical bath deposition methods, respectively. Based on the ZnO thin film photoluminescence results, an understanding of the point defects and defect complexes responsible for the luminescence nature of undoped ZnO thin films will be established. The characteristic defect emission for the pristine ZnO thin films will then be used to identify the defect level transitions responsible for indirect excitation of the Eu^{3+} and Tb^{3+} ions doped into the ZnO powders.

The current chapter gives an introduction to the research work together with a brief background on ZnO defects, the problem statement and research objectives. In chapter two a literature review of the optical properties as well as some theoretical background on the ZnO defects are presented. The luminescent properties of the trivalent rare-earth ions and the respective crystal-field selection rules are also discussed. Chapter three gives a detailed description of the synthesis methods and experimental techniques used in this study. The results of the XRD characterisation and photoluminescence properties of the ZnO thin films deposited under different conditions are presented in chapter four. In

chapter five, the characterisation and blue-laser excitation studies of pristine ZnO as well as the Eu^{3+} and Tb^{3+} doped ZnO powders will be presented. Finally, the conclusions and suggestions for future research work are presented in Chapter six.

Chapter 2

Literature review

2.1 Introduction

Spectroscopy is a research technique which involves the study of how materials absorb, emit or scatter incident radiation [26]. The incident radiation can be in the form of particles such as electrons, protons and neutrons or electromagnetic radiation [26]. The first spectroscopy experiment was carried out in the seventeenth century by Isaac Newton. The experiment involved the dispersion of incident radiation from the sun using a prism resulting in multiple colours, each with a characteristic wavelength. These colours form the visible region of the electromagnetic spectrum which ranges from 390.0 nm to about 750.0 nm [26]. The discovery of infrared and ultra-violet radiation by Herschel and Ritter, respectively, followed in the nineteenth century [26].

From the above forms of incident radiation, this study is mainly concerned with the ability of a material to absorb and emit electromagnetic radiation (photoluminescence). Photoluminescence spectroscopy only works well with optically active materials i.e. materials which can respond when probed with a light source. The subsequent emission gives information on the optical and electronic properties of the material under investigation. These optical characteristics can also be used to deduce the electronic states of defects or impurities associated with the material.

2.2 Photoluminescence in semiconductors

Photoluminescence is one of the many sources of cold body radiation where light emission is realised without intentionally heating the material as is the case for incandescence. It is the need for more cold body emitters that has motivated the continued search for efficient luminescent solid state materials. Photoluminescence can be defined as the subsequent emission from a material when pumped by some resonant incident electromagnetic radiation [25]. The emitted radiation is a result of electronic inter-band transitions between excited

initial and terminal energy levels within the material. It is from these radiative transitions that the signature optical characteristics of a material can be determined. However for photoluminescence to occur the material of interest has to be optically active, i.e. the relevant excited energy levels can be populated by the incident radiation. The population of the excited electronic levels is only realised if the incident radiation energy matches the energy difference between the ground state level (E_0) and the excited state level (E_3) in figure 2.1 (i). Transitions can only be radiative if the energy difference between the emitting and terminating energy levels is sufficiently large for electron decay through photon emission (figure 2.1 (ii)). Otherwise the transitions are non-radiative (figure 2.1 (iii)) and energy is dissipated through the emission of phonons [25]. Photon energy (E) is given by the product of the radiation frequency (ν) and Planck's constant (h) as shown in equation (2.1) [25].

$$E = h\nu \tag{2.1}$$

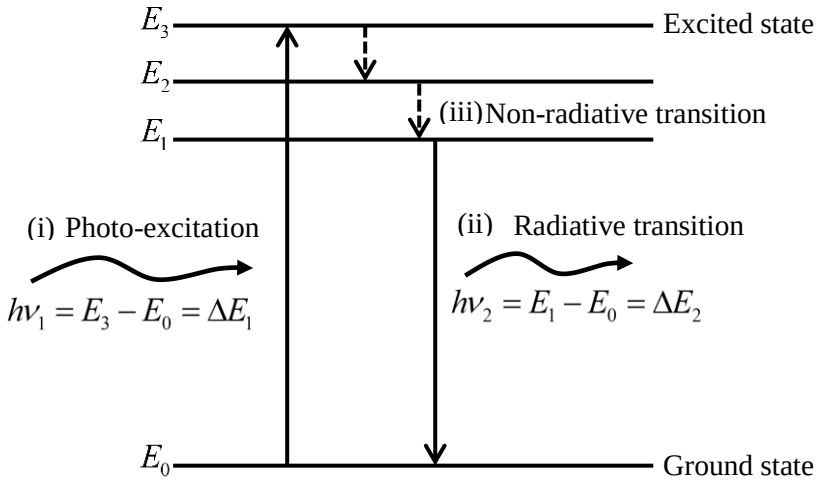

Figure 2.1 Excitation and emission processes: (i) an incident photon of energy $h\nu_1$ excites an electron from the ground state energy level, E_0, to the excited energy level, E_3. (ii) Radiative transitions from the E_1 energy level to the ground state level by emitting a photon of energy $h\nu_2$. (iii) Intra-band non-radiative transitions shown by the dashed lines from the E_3 energy level to the E_1 energy level.

The energy of the emitted photon is equivalent to the energy difference between the emitting and terminal electronic energy levels (figure 2.1 (iii)). Since the photo-excitation and emission energies are characteristic of the energy levels of the material, it is possible to observe excitons at low temperatures as well as deduce the electronic levels associated with a particular material from absorption and emission spectroscopy [25].

A diverse range of materials which include organic dyes, insulators with dopant transition metals or rare-earths and semiconductors possess luminescence properties [25]. Some of these luminescence properties are strongly linked to the existence of defects or intentionally induced impurities within the material [25]. Of the above materials, wide bandgap semiconductors such as ZnO are of particular interest as they simultaneously present high transmission within the visible region and a high electrical conductivity. The conductivity of a material can be defined by the size of the energy bandgap and the mobility of the charge carriers. In the case of insulators, the energy bandgap is very wide such that at room temperature, the strongly bound valence electrons have insufficient energy to occupy the CB (figure 2.2(i)) [27]. For conducting materials, the valence electrons can move freely between atoms since the overlap between the VB and CB avails partially empty or filled electronic states at room temperature (figure 2.2(ii)) [27].

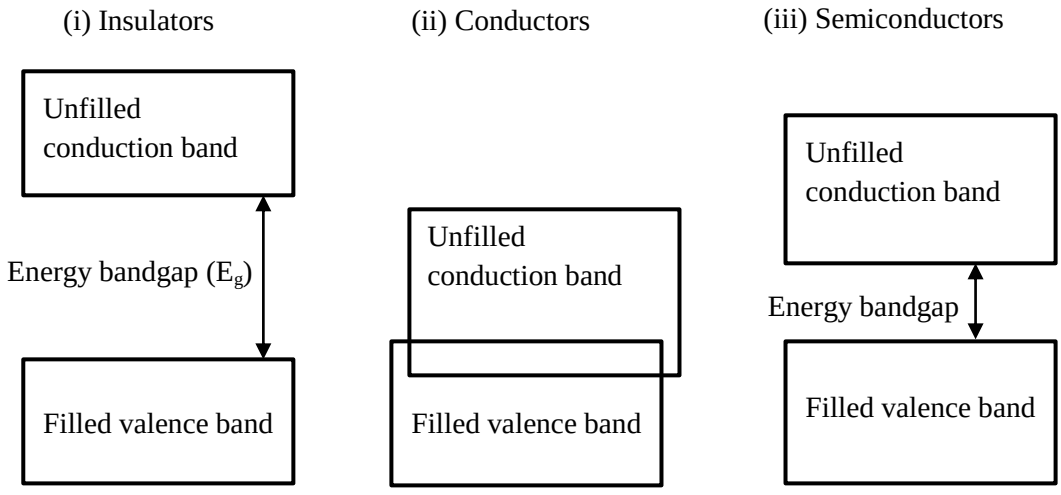

Figure 2.2 An illustration of the valence band, conduction band and energy bandgap in (i) insulators, (ii) conductors and (iii) semiconductors.

However in semiconductor materials the valence electrons are not as strongly bound and the energy bandgap is relatively narrow as compared to that of insulators. Therefore some of the valence electrons can occupy the CB at room temperature enabling semiconductors to exhibit some level of conductivity (figure 2.2 (iii)) [27].

The energy gap between the CB and VB in semiconductors can be classified as a direct or an indirect bandgap. The direct and indirect bandgaps are illustrated by the energy dispersion as a function of the electron momenta, where

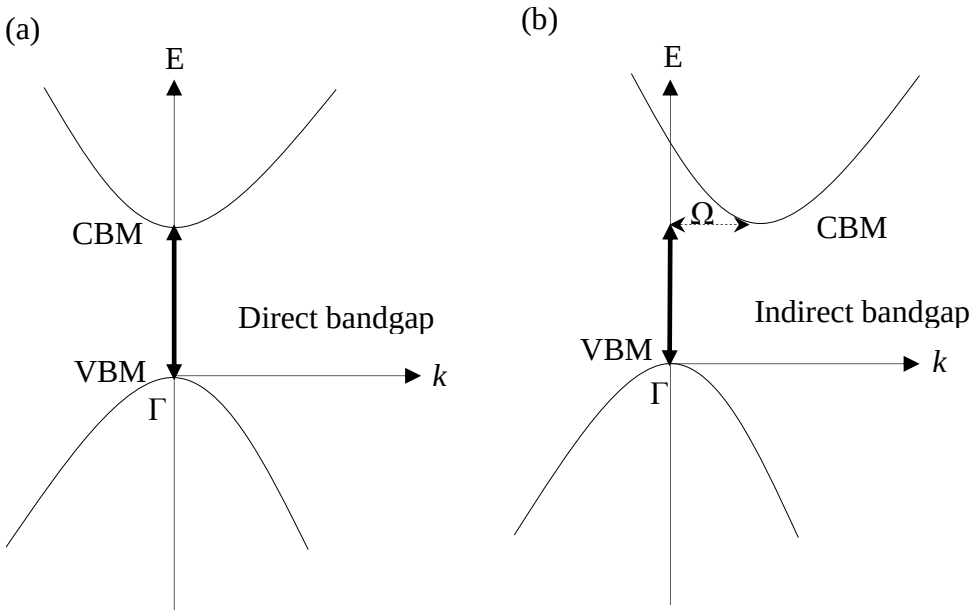

Figure 2.3 A schematic illustration of (a) a direct bandgap and (b) an indirect bandgap in semiconductors.

k is the wave-vector (figure 2.3) such that [28]:

i. A direct bandgap semiconductor is characterized by the CB minimum (CBM) energy being directly above the VB maximum (VBM) as shown in figure 2.3 (a) at the Γ point.

ii. In the case of an indirect bandgap semiconductor, the CBM and the VBM energies occur at translated *k*-values (figure 2.3 (b)) and thus

inter-band transitions are mediated through absorption or emission of a phonon of wave vector Ω.

The energy dispersion relations are based on the energy of the carriers, *E*, and wave-vector, *k*, relation given by equation (2.2) [28],

$$E(k) = E_B \pm \frac{k^2\hbar^2}{2m_e}, \tag{2.2}$$

where m_e is the effective mass of the carrier. When considering the CB where the carriers are electrons, the second term is positive such that E_B is the energy at the conduction band minimum. For the VB (carriers are holes), the second term is negative such that E_B is the energy at the valence band maximum. This expression holds in the limit for small variations in *k*. ZnO has a wide bandgap ranging between 26 568 cm^{-1} (3.30 eV) [29] and 27 132 cm^{-1} (3.37 eV) [30] at room temperature (300 K). As such, the incident radiation has to be in the ultra-violet range (30 769 cm^{-1} – 26 316 cm^{-1} (325.0 nm – 380.0 nm)) for the occurrence of inter-band transitions. However, between the CBM and VBM of semiconductors such as ZnO there are localized electronic energy levels induced by defects which may allow sub-bandgap energy excitations. These defects associated with materials in general will be defined in the subsequent section. An in-depth discussion on the point defects related to ZnO as well as their contribution to the electronic and luminescence characteristics of ZnO will follow thereafter.

2.3 ZnO point defects

A perfect crystalline material has been found to be difficult to attain as materials will always possess some form of lattice imperfections [27]. These defects can be described according to their geometrical position, charge states or size where point defects normally relate to imperfections in the atomic size range [27]. These atomic size defects include vacancies, antisites, interstitials and defect complexes (figure 2.4) and are mainly intrinsic defects. A vacancy defect is one where a regularly occupied atomic lattice site is empty (figure 2.4) while an interstitial defect is one where an atom takes up a site which is normally unoccupied [27] (figure 2.4). An antisite defect occurs when an atom occupies substitutionally

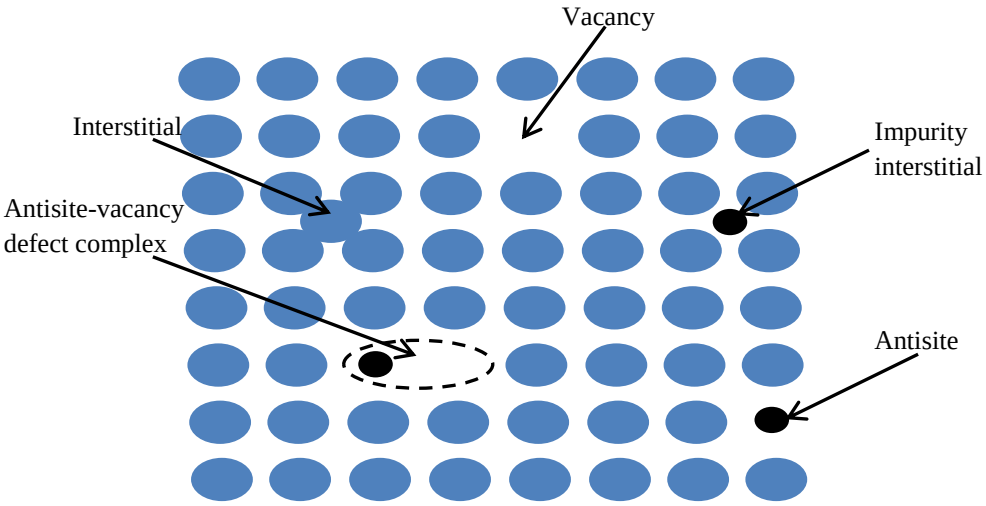

Figure 2.4 Schematic illustration of typical point defects associated with a solid material.

another atom's regular lattice site. A defect complex is one where two point defects occur next to each other for example when a vacancy defect occurs next to an interstitial (figure 2.4). In some cases defects can be in the form of impurity interstitials due to the introduction of foreign atoms into the host lattice [27].

Point defects in the form of zinc vacancies, zinc interstitials, oxygen vacancies, zinc antisites, oxygen interstitials and oxygen antisites have been shown to be responsible for the intrinsic electrical and optical properties of ZnO [21]. The electrical conductivity in semiconductors can be classified according to the nature of the type of majority charge carriers. If the CB has electrons as majority charge carriers with a minority of holes in the VB for recombination then the semiconductor is of the n-type [27]. For the p-type semiconductor, the VB will have a large number of holes with a minority of electrons in the CB [27]. In the literature, experimental [31] and theoretical [32] studies have shown that the n-type characteristic is preferred over the p-type in intrinsic ZnO. The intrinsic n-type property of ZnO has been attributed to native donor defects in the form of zinc interstitials (Zn_i) [31,32] and oxygen vacancies (V_O) [33]. Of the two donor defects, the Zn_i has been identified as a shallow donor level situated at ~ 242 cm^{-1} (30 meV) [31,32] below the CB as such it provides electrons that contribute towards the intrinsic n-type behaviour in ZnO [32]. On the other hand, the V_O has been experimentally determined to be a deep donor

level situated at 6 441 cm^{-1} (0.8 eV) below the CB [34]. Hence these defect levels are less probable to contribute towards n-type ZnO [34]. Although it is difficult to obtain intrinsic p-type ZnO due to the lower formation energies of n-type defects (6.0 eV for Zn_i and 3.72 eV for V_O) compensating the p-type related defects [35,36] as stated in section 1.1, experimental studies on ZnO thin films have reported intrinsic p-type characteristics [36,37]. The intrinsic p-type ZnO can be realized through the use of growth conditions that promote acceptor defects while suppressing the n-type related donor defects [36,37,38]. Although growth parameters that promote acceptor defects such as the zinc vacancy (V_{Zn}), oxygen interstitials (O_i) and oxygen antisites (O_{Zn}) are used, they still occur in low concentrations due to their relatively high formation energies of 7.3 eV, 9.5 eV and 8.5 eV, respectively [36].

Apart from being responsible for the intrinsic n- and p- type characteristics of ZnO, the native donor and acceptor point defects have been related to the luminescence properties in ZnO [39,40,38]. It is the donor-acceptor transitions in particular that have been shown to contribute towards the visible-region emission observed in ZnO with ultra-violet excitation [39,40,38]. In order to obtain a clear understanding of the radiative transitions associated with the donor and acceptor defect levels discussed above, it is important to consider the defect formation energies and their respective transition levels relative to the CBM and VBM. Calculations of defect formation energies and energy level positions of ZnO point defects have been reported [12,21,41] and are useful in explaining the relative ease of realising intrinsic n-type as compared to p-type ZnO [12,21,41]. The concentration of intrinsic defects, c_i, in a solid material depends on the defect formation energy and is given by equation (2.3) [42]

$$c_i = N_{sites} e^{\left(\frac{-E^f}{k_B T}\right)} \tag{2.3}$$

where, N_{sites} = Number of sites per unit volume that can be occupied by a defect

k_B = Boltzmann's constant

T = Temperature

E^f = defect formation energy

From equation (2.3), the concentration of native defects exponentially decays with increase in defect formation energy. These native defects result in transition levels within the bandgap of ZnO that can be determined from the formation energies [21]. Defect levels that are more likely to be thermally ionized at 300 K (room temperature) by virtue of their position within the bandgap are shallow levels and if thermal ionization is less probable then the defect level is considered to be deep level [21]. Shallow levels may be situated either close to the CBM (donor level) or near the VBM (acceptor level) [21]. However these thermally ionized levels are not necessarily responsible for the optical characteristics of ZnO. Defect levels associated with the optical properties of ZnO can also be derived from the defect formation energies [21]. If the defect lattice relaxations significantly change from a particular charge state to a different charge state, the thermally ionized levels will not be considered as optical transition levels [21].

From theoretical calculations, the V_O and V_{Zn} vacancies have the lowest defect formation energies of 29 950 cm^{-1} (3.72 eV) and 29 789 cm^{-1} (3.70 eV), respectively [21]. The Zn_i and the O_i have the next least formation energies of about 48 306 cm^{-1} (6 eV) and 68 434 cm^{-1} (8.5 eV), respectively [12,21]. The Zn_O and the O_{Zn} antisites require relatively high formation energies of approximately 72 459 cm^{-1} (9.0 eV) and 76 485 cm^{-1} (9.5 eV), respectively [21]. Among the intrinsic donor defects, the V_O has been identified to be a deep donor with transition levels at 6 441 cm^{-1} (0.8 eV) and 9 661 cm^{-1} (1.2 eV) below the CBM [34,41,43]. However, there are variations in the energies of the defect levels caused by an under approximation of the ZnO bandgap when calculated by the normally used local-density or the generalized-gradient approximations (GGA) [32,21]. The V_O can also take up a V_O^0, V_O^+ or V_O^{2+} charge state with the V_O^+ charge state being the most unstable [41]. Another donor defect is the Zn_i which can occupy either the tetrahedral or the octahedral site in the wurtzite structure [41,43]. Similarly, the Zn_i (shallow donor) occurs in the Zn_i^0, Zn_i^+ and Zn_i^{2+} charge states within a few wave-numbers from the CBM [31]. This defect has a relative high formation energy for n-type ZnO and is reported to be in the region of 48 306 cm^{-1} (6.0 eV) [41] to 32 204 cm^{-1} (4.0 eV) [43]. The relatively high formation energy can be reduced to 4 026 cm^{-1} (0.5 eV) under p-type

conditions making it difficult to realize p-type ZnO as the holes are compensated by the Zn_i defect [43]. For the zinc antisite defect (Zn_O), the zinc ion (Zn^{2+}-0.74 Å) takes up a lattice site normally occupied by an oxygen ion (O^{2-}-1.40 Å) [43]. Zn_O defects are considered to be either shallow or deep donor levels as they are a defect complex comprising of the V_O (deep donor) and Zn_i (shallow donor) [43]. This defect is more stable when in a 2+ positive charge state [41] and has a relatively low formation energy of ~4.5 eV under p-type conditions thereby compensating for holes [43]. The Zn_O defect formation energy is relatively high for the n-type in comparison to the other two donor defects (Zn_i and V_O) [12,32]. The above donor defects (Zn_O, Zn_i and V_O) are expected to form easily under zinc-rich preparation conditions [21].

The inherent ZnO acceptor defects include the zinc vacancy, the oxygen interstitial and the oxygen antisite and are expected to have low formation energies under oxygen-rich growth conditions [21]. Of these acceptor defects, the zinc vacancy is the most common among the other intrinsic acceptor defects and has two deep levels at 1 449 cm^{-1} (0.18 eV) and 7 004 cm^{-1} (0.87 eV) [41] above the VBM. Oba et al. [43] and Srivastava [29] further proposed an additional V_{Zn} defect level at 19 322 cm^{-1} (2.4 eV) and a doubly ionized zinc vacancy defect level (V_{Zn}^{2-}) at 22 221 cm^{-1} (2.76 eV), respectively, above the VBM. Surrounding the V_{Zn} defect are partially filled states due to broken bonds of the four nearest neighbour oxygen [41]. These states can accommodate additional electrons thereby making the V_{Zn} level an acceptor [41]. The V_{Zn} also has the least defect formation energy of 29 789 cm^{-1} = 3.7 eV under n-type conditions and this becomes relatively high for p-type ZnO (58 772 cm^{-1} = 7.3 eV) [41]. V_{Zn} can occur in the neutral, 1- and 2- charge states with the 2- as the preferential charge state [41]. Another deep acceptor level is that due to the oxygen interstitial which can occupy the tetrahedral sites as an oxygen ion or as an isolated oxygen molecule [41,43]. The O_i formation energy (46 697 cm^{-1} = 5.8 eV) is greater than the formation energy for the V_{Zn} defect for n-type ZnO [41]. The O_i defect levels are 5 798 cm^{-1} (0.72 eV) and 12 801 cm^{-1} (1.59 eV) above the VBM [41]. As for the oxygen antisites, the oxygen atom occupies a lattice site normally occupied by a zinc atom. This defect has the highest formation energy with respect to the

other two acceptor defects (V_{Zn} and O_i) [41]. Similar to the V_{Zn} defect, the O_{Zn} defect has two deep acceptor levels at 12 238 cm^{-1} (1.52 eV) and 14 250 cm^{-1} (1.77 eV) above the VBM [41]. This defect is the least probable to occur due to its relatively high formation energy, however the formation energy is significantly reduced for oxygen-rich preparation conditions [21]. In addition to the isolated ZnO point defects, there are intrinsic defect complexes (figure 2.4) such as the oxygen vacancy-zinc interstitial (V_oZn_i) and the zinc vacancy-zinc interstitial ($V_{Zn}Zn_i$) defect complexes [44]. Of the two complexes, only the V_oZn_i defect complex has transition levels within the bandgap which are situated at 19 081 cm^{-1} (2.37 eV) and 17 471 cm^{-1} (2.17 eV) above the VBM [44]. These defect complexes act as non-radiative recombination centers through which non-radiative decay may occur [45,46] since isolated point defects cannot be non-radiative centers [12,46].

The aforementioned donor and acceptor defect levels are responsible for the visible luminescence observed in ZnO with ultra-violet excitation (28 482 cm^{-1} – 27 488 cm^{-1} (351.1 nm – 363.8 nm)) [23]. The radiative transitions associated with emission in semiconductors are summarised as follows [25]:

a) Inter-band CB to VB transitions; the emission wavelength in this transition corresponds to the semiconductor bandgap energy and it is observed at relatively high temperatures or electric fields.
b) Exciton to VB radiative decay occurs at relatively low temperatures as either free exciton or bound exciton to VB transitions.
c) Donors to VB transitions involve the radiative decay of an electron from a donor level to a hole in the VB. In some cases the electron-hole radiative recombination will be from deep donor levels.
d) CB to acceptor transitions, an electron decays radiatively from the CB to an acceptor defect level situated near the VBM.
e) Donor to acceptor radiative decay involves donor to acceptor defect level transitions. Normally the donor transition level lies near the CBM while the acceptor level is near the VBM.

These transition possibilities can be related to the visible emission observed in ZnO and are therefore useful for the energy transfer processes that result in the

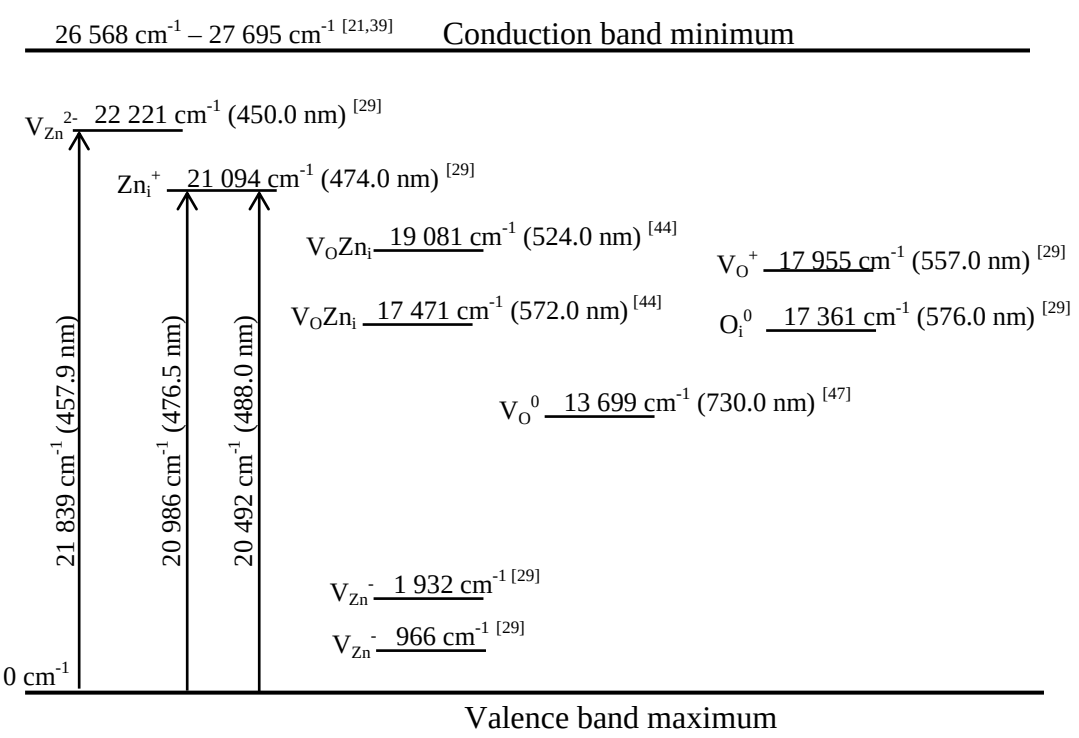

Figure 2.5 The transition energy levels associated with the ZnO intrinsic point defects that can be populated using the 457.9 nm, 476.5 nm and 488.0 nm excitation lines. The superscript 0 denotes a neutral charge state while -/+ denote a singly charged negative/positive state, respectively, and 2- is a doubly charged negative state. (8 051 cm^{-1} = 1 eV)

excitation of dopant impurities such as the rare-earth ions. The transition levels associated with the inherent ZnO defects determined from reported experimental [29,47] and theoretical [21,44] studies that are likely to be populated by the blue laser excitation lines used in this work are presented in figure 2.5.

2.4 Trivalent rare-earth ions

Rare-earth elements form part of the f-block in the periodic table consisting of 14 elements starting from lanthanum (Z = 57) to lutetium (Z = 71). The rare-earth electronic configuration can be described as having a xenon core, a successively occupied $4f^N$ shell from lanthanum to lutetium and the 5d6s shells accommodating the valence electrons, i.e. $[Xe]4f^N5d^16s^2$, where N = 0 – 14 [48]. The completely occupied $5s^2$ and $5p^6$ shells which are part of the Xe core shield the partially filled $4f^N$ shell [49] (figure 2.6). Rare-earth elements can exist as either divalent (RE^{2+}) or trivalent (RE^{3+}) ions with the latter being the most common ionic state because it is more stable. The shielding is responsible for the

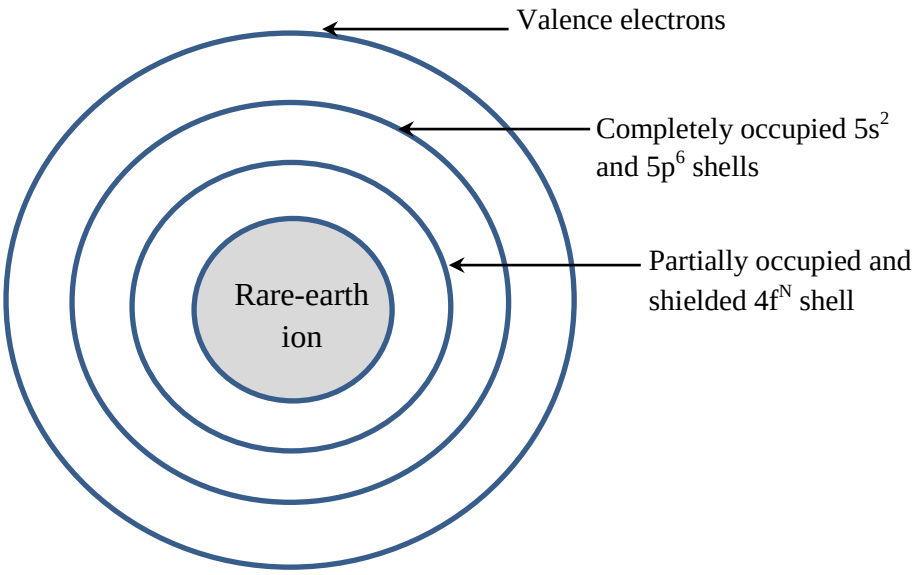

Figure 2.6 The radial distribution of the electron shells in trivalent rare-earth ions with the partially filled $4f^N$ shell shielded by the completely occupied $5s^2$ and $5p^6$ shells **[49]**.

rare-earth's unique and relatively intense atomic-like luminescence characteristics [49]. The above emission properties are mainly attributed to the intra-$4f^N$ electronic transitions within rare-earth ions [49] and are responsible for the RE^{3+} energy structure. These electronic transitions result in spectra that exhibit relatively narrow and intense peaks due to shielding of the partially filled $4f^N$ shell from the ligand environment which results in weak ligand-ion perturbations at the RE^{3+} ion site [49].

The rare-earth elements of interest in this study are europium (Eu) and terbium (Tb) which have the $[Xe]4f^76s^2$ and $[Xe]4f^96s^2$ respective electronic configurations. In their trivalent state, europium (Eu^{3+}) and terbium (Tb^{3+}) ions have $[Xe]4f^6$ and $[Xe]4f^8$ electronic configurations, respectively. The Eu^{3+} ion has a ground state multiplet of $^7F_0$ while that for the Tb^{3+} ion is $^7F_6$. The separate Eu^{3+} and Tb^{3+} free-ion energy level diagrams are shown in figure 2.7. The ground state multiplet is assigned the label Z according to the Dieke diagram [26] (figure 2.7). The first to the sixth excited multiplets are labelled Y, X, W, V, U and T, respectively, with the emitting multiplets assigned the letters A and B [26] (figure 2.7). The associated corresponding crystal-field energy levels are labelled

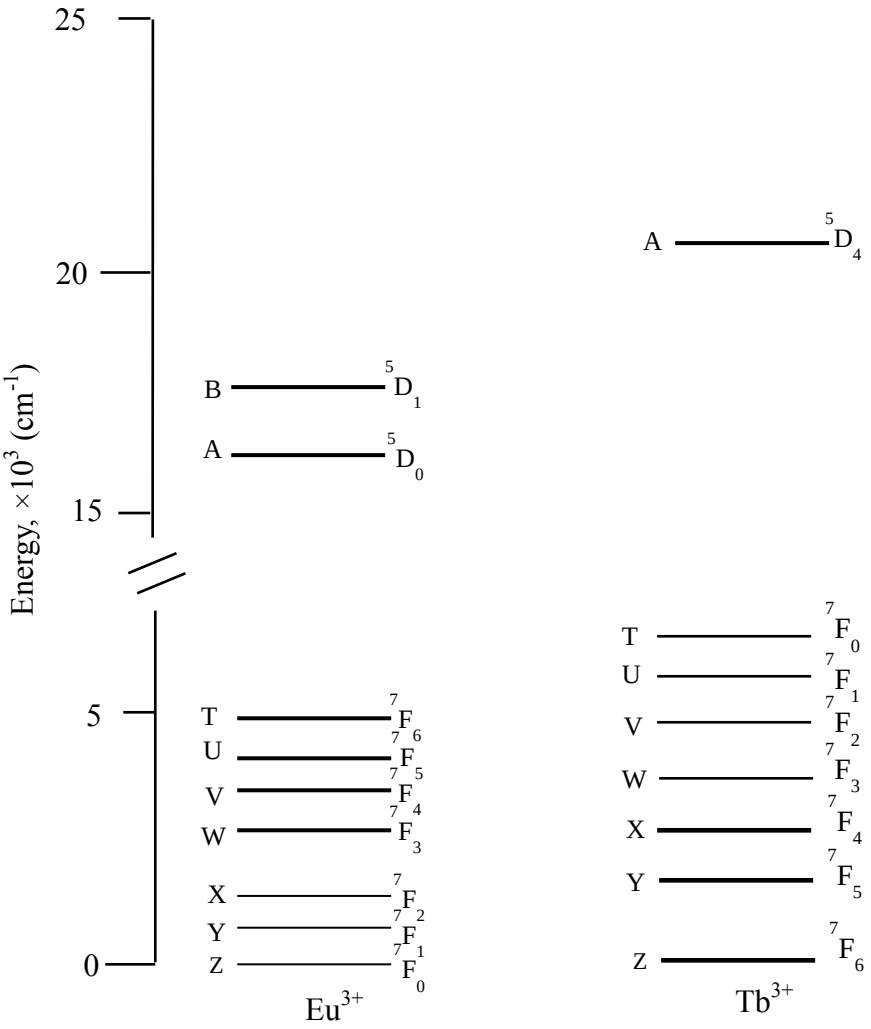

Figure 2.7 Trivalent europium and terbium free ion energy level diagrams with the multiplets labelled with upper case letters of the alphabet in accordance to the Dieke diagram [26].

with the addition of a subscript to denote each crystal-field energy level e.g. X_1, X_2, X_3,… etc. of the X multiplet, in order of increasing energy.

RE^{3+} ions have narrow absorption and emission bands [49]. Because of this, the RE^{3+} ions are often incorporated into host materials, usually semiconductors such as ZnO, which act as absorption antennas and then transfer the energy to the RE^{3+} ion [50]. On incorporation into the host, knowledge of the exact location of the RE^{3+} ion is important for deducing its energy level structure. The experimental techniques used in this study do not have the capability to give information on the location of the RE^{3+} ion within the ZnO lattice. However in the literature, the Tb^{3+} ion (0.92 Å) and the Eu^{3+} ion (0.95 Å) have been proposed to occupy the

Zn^{2+} (0.74 Å) lattice site in the ZnO structure [9,16]. The suggested RE^{3+} lattice location is supported by theoretical calculations [51] and experimental [51,52] results which have shown that the RE^{3+} ion takes up the C_{3v} symmetry site (i.e. Zn^{2+} lattice site). In addition, Badalawa et al. [52] showed that the occupation of a C_{3v} site symmetry by the RE^{3+} ion in the ZnO host may not be uniform. The RE^{3+} ions could also occupy sites of lower than C_{3v} symmetry so as to compensate for the Zn^{2+} and RE^{3+} charge difference as well as accommodate the relatively larger RE^{3+} ion [52]. Despite the narrow absorption of the RE^{3+} ions, they have relatively high luminescence [50] making them suitable dopants for the enhancement of the ZnO luminescent properties.

2.5 The Hamiltonian

Description of the crystal-field energy levels of the RE^{3+} ion requires determination of the effective terms of the Hamiltonian. The free ion behaviour of the RE^{3+} ion can only be related to the $4f^N$ electrons. The other electronic shells of the RE^{3+} ion are completely filled making them spherically symmetric. As such only the $4f^N$ electronic shell contributes towards the relative positions of the 4f energy levels [49]. The energy levels for an N-electron system can be theoretically determined by the Hamiltonian (equation (2.4))

$$H = H_{KP} + H_C + H_{SO} \tag{2.4}$$

The components are given by

$$H_{KP} = -\sum_{i=1}^{N}\left(\frac{\hbar^2}{2m}\nabla_i^2 + \frac{Ze^2}{r_i}\right) \tag{2.5}$$

$$H_C = \sum_{i<j}^{N}\frac{e^2}{r_{ij}} \tag{2.6}$$

$$H_{SO} = \sum_{i}^{N}\xi(r_i)\vec{l}\cdot\vec{s} \tag{2.7}$$

In equation (2.5), the first term gives the kinetic energy of the electrons while the second term is the potential energy of the electrons in the presence of the positively charged nucleus [53]. Both terms of H_{KP} are radially dependent and therefore do not contribute towards the lifting of the 4f configurational degeneracy [49,53]. H_C (equation (2.6)) is the Coulomb interaction between pairs of 4f electrons which are distance r_{ij} apart [53]. The term H_{SO} (equation (2.7)) represents the spin-orbit interaction [53]. This is a relativistic effect where the electron is considered to be stationary while the positively charged nucleus orbits around the electron [49]. The Coulomb and spin-orbit interactions are largely responsible for the free ion energies of the RE^{3+} ion [49].

Exact solutions of equation (2.4) cannot be determined for a many-electron system [53]. As such the central-field approximation is used to obtain approximate solutions. This approach assumes that in an N-electron system, each electron moves independently with respect to the field of the charged nucleus and as it moves it experiences a mean spherically-symmetric potential field $U(r_i)$ from the other (N-1) electrons [53,54]. Therefore the Hamiltonian according to the central-field approximation can be expressed in the form

$$H_D = \sum_{i=1}^{N}\left(-\frac{\hbar^2}{2m}\nabla_i^2 + U(r_i)\right) \tag{2.8}$$

where

$$\sum_{i=1}^{N} U(r_i) = -\sum_{i=1}^{N}\frac{Ze^2}{r_i} + \left\langle \sum_{i<j}^{N}\frac{e^2}{r_{ij}}\right\rangle. \tag{2.9}$$

The first term in equation (2.9), gives the potential energy as was stated above while the second term on the right is the averaged electron-electron repulsion experienced by the single electron in the presence of the other (N-1) electrons. The difference between (H_{KP} + H_C) and H_D given in equation (2.10) is small enough in magnitude and can thus be approximated as a perturbation to the central-field Hamiltonian [53,54].

$$(H_{KP} + H_C - H_D) = \sum_{i<j}^{N} \frac{e^2}{r_{ij}} - \left\langle \sum_{i<j}^{N} \frac{e^2}{r_{ij}} \right\rangle \qquad (2.10)$$

The second term on the right in equation (2.10) is spherically-symmetric therefore it has uniform effect on the electronic energy levels. However the first term (H_C) results in a perturbation responsible for the Coulomb splitting of the $4f^N$ configuration degeneracy to ^{2S+1}L terms [49] (figure 2.8). For rare-earth ions $H_{SO} < H_C$ with the spin-orbit term (H_{SO}) further splitting the ^{2S+1}L terms to $^{2S+1}L_J$ multiplets as shown in figure 2.8 [49]. The 2S+1 represents the multiplicity of the term while L and J are the total orbital angular momentum and the total angular momentum, respectively [55]. To build wavefunctions suitable for the central-field Hamiltonian for an N-electron system an appropriate coupling scheme needs to be chosen [53]. In the LS coupling scheme commonly used for rare-earth elements [49], the individual electron spins s_i interact with each other to give a total spin angular momentum S. This also applies to the individual orbital angular momenta l_i which result in a total angular momentum L. The total spin S and the total orbital angular momentum L are then added vectorially [53].

The free ion degeneracy is lifted when the RE^{3+} ion is surrounded by ligand

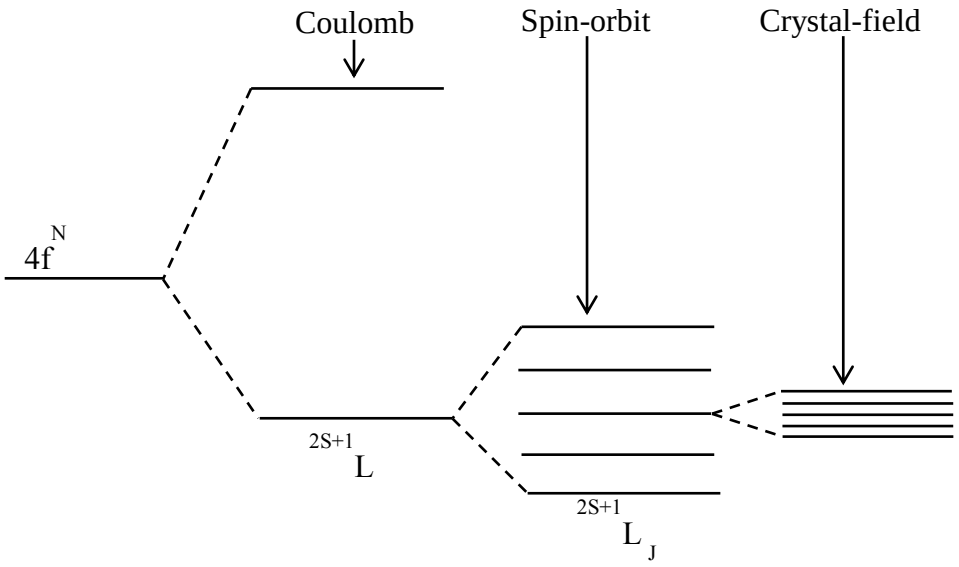

Figure 2.8 Schematic illustration of the Coulomb, spin-orbit and crystal-field interactions experienced by the RE^{3+} ion in a crystal lattice.

ions on incorporation into a crystal lattice because the symmetry of the RE^{3+} site becomes lower than spherical [49]. The lifting of the free ion degeneracy is due to the electric field from the electrons of the surrounding ligand ions [49]. The charges of the ligands produce an electric field which interacts with the 4f electrons. This field is referred to as the crystal field and causes the splitting of each free ion $^{2S+1}L_J$ multiplet into crystal-field energy levels (figure 2.8) [49]. The number of crystal-field energy levels for each J multiplet depends on the point symmetry of the RE^{3+} ion. The complete Hamiltonian including the crystal-field potential, V_{CF}, is given by the equation

$$H = H_{KP} + H_C + H_{SO} + V_{CF}. \tag{2.11}$$

$V_{CF} < H_{SO}$ and so the splittings due to crystal-field effects are of relatively small magnitude as shown in figure (2.8).

2.6 Selection rules

Electronic transitions from emitting (initial) states to terminal (final) states can be described in terms of the afore-stated term symbol ($^{2S+1}L_J$). However the transitions between any of these states have to obey a set of selection rules based on the change in S, L and J values. One example is the spin selection rule which requires that the multiplicity of the emitting state be the same as that of the terminal state for a transition to be allowed, thus a $^5D_1 \rightarrow {}^7F_6$ transition, is spin-forbidden [55]. The spin-orbit coupling associated with RE^{3+} ions results in the relaxation of this selection rule such that spin-forbidden transitions are experimentally observed [26].

Apart from the spin selection rule, it is also necessary that the electronic transitions satisfy the parity selection rule which depends on whether a transition is electric-dipole or magnetic-dipole in nature. The parity selection rule is governed by the orbital quantum number l such that if $\Delta l = 0$ (i.e. no change in parity from the initial state to the final state) the transition is forbidden for the electric-dipole case. Therefore s ↔ s and f ↔ f transitions are not allowed whereas s ↔ p and d ↔ f transitions satisfy the electric-dipole parity selection rule [48]. When a RE^{3+} ion is placed in a crystal lattice, the parity selection rule is

relaxed for the 4f ↔ 4f electronic transitions due to mixing of opposite parity states such as from the $4f^{N-1}5d$ configuration into the $4f^{N}$ configuration states [49,26]. For this selection rule, the electric-dipole transition probability which is given by $e\int \Psi_A \hat{r}\, \Psi_B dV$ must be nonzero for the transition A↔B to be allowed [26], where Ψ_A and Ψ_B are the wavefunctions of the initial and final states, respectively. The operator $\hat{r}$ is of odd parity and so if Ψ_A and Ψ_B are of the same parity then the electric-dipole transition is forbidden [26]. For a RE^{3+} ion incorporated into a crystal lattice, the electric-dipole transitions are crystal-field induced such that the free ion rules breakdown to give the following selection rules in the LS coupling scheme [49,56]:

1. $\Delta S = 0$
2. $\Delta L \leq \Delta 2l$
3. $\Delta J \leq 6$

On the other hand magnetic-dipole transitions are of even parity, i.e. the initial and final states have the same parity hence 4f ↔ 4f electronic transitions are allowed [49,26]. In the case of RE^{3+} ions, electronic transitions are mostly of the electric-dipole type with the magnetic-dipole related transitions being much weaker in comparison [49]. The probability of an electric-dipole transition occurring is of the order 10^5 greater than the probability of a magnetic-dipole transition provided both transitions are allowed [26]. Therefore magnetic-dipole transitions are generally less likely to occur.

Experimentally, crystal-field energy levels of RE^{3+} ions (Tb^{3+} and Eu^{3+} in this case) are deduced from the electronic transitions between emitting and terminating levels. Theoretically, crystal-field energy levels can be obtained as eigenvalues of the Hamiltonian (equation 2.11). Solving the Hamiltonian is a complicated task [26]. A simplified approach that makes use of group theory predictions based on the point symmetry of the RE^{3+} ion site is commonly used [26]. The symmetry properties of the RE^{3+} ion in a crystal lattice determine the symmetry of the Hamiltonian (equation 2.11) and the associated eigenfunctions hence the energy eigenvalues which are the crystal-field energy levels [26]. From point symmetry analysis the number and characteristics of the

crystal-field energy levels associated with a particular RE^{3+} ion site and the applicable selection rules can be determined [26].

To accomplish the aforementioned, representations of the symmetry operations on the RE^{3+} ion centre need to be considered. Each symmetry operation is associated with a transformation matrix such that a complete set of symmetry operations on a group can be related to a set of matrices and these matrices constitute a representation, Γ [26]. The representation can be either reducible or irreducible (Γ_i). If Γ is reducible, then $\Gamma = \sum a_i \Gamma_i$ where Γ_i appears a_i times in the reduction [26]. It is the irreducible representations (irreps), Γ_i, that are of interest as these are closely associated with the crystal-field energy levels [26]. For an electric-dipole transition to be allowed, the direct product of the initial-state irrep, Γ_i, and the electric-dipole operator, Γ_{ED}, should contain an irrep associated with the final state, Γ_f, i.e. $\Gamma_i \times \Gamma_{ED} \subset \Gamma_f$ [26].

In the present work the Tb^{3+} ion and the Eu^{3+} ion occupy a C_{3v} symmetry site in the ZnO host, as adopted from Pereira et al. [57]. Both RE^{3+} ions have an even number of electrons in their $4f^N$ orbitals. As such the same set of decomposition tables from Koster et al. [58] (pages 101 and 104) were used to determine the irreps as well as the number of levels associated with a given J value for a C_{3v} symmetry site (table 2.1).

Table 2.1 C_{3v}-symmetry irreps for crystal-field energy levels.

J	Γ_1	Γ_2	Γ_3	Total number of energy levels
0	1	0	0	1
1	0	1	1	2
2	1	0	2	3
3	1	2	2	5
4	2	1	3	6
5	1	2	4	7
6	3	2	4	9

The allowed and forbidden electric-dipole transitions for the C_{3v} point group symmetry (table 2.2) were deduced using group theory multiplication tables (Koster et al. [58], page 55) with the electric-dipole operator being of either Γ_1 or Γ_3 symmetry.

Table 2.2 Selection rules for electric-dipole transitions for C_{3v} symmetry.

C_{3v}	Γ_1	Γ_2	Γ_3
Γ_1	allowed	forbidden	allowed
Γ_2	forbidden	allowed	allowed
Γ_3	allowed	allowed	allowed

Tables 2.1 and 2.2 provide a guide for the deconvolution of the observed Eu^{3+} and Tb^{3+}emission bands presented later in sections 5.2.3.2 and 5.2.3.5, respectively.

Chapter 3

Experimental aspects

3.1 Introduction

The luminescence properties of two forms of ZnO samples were investigated in this study. These are undoped ZnO thin films and rare-earth doped ZnO powders synthesized using the radio-frequency magnetron sputtering and the chemical bath deposition methods, respectively. Each of these preparation methods uses relatively simple procedures that are cost effective and therefore preferred over other synthesis methods.

ZnO thin films can be synthesized using multiple deposition methods which include pulsed laser deposition [39], molecular beam epitaxy [6] and radio-frequency (RF) magnetron sputtering [8,59] techniques. The RF magnetron sputtering method was used in this work because of the following inherent advantages:

i. low deposition temperatures [8];
ii. high thin film - substrate adhesion [8];
iii. uniform thin - film deposition over large surface areas [8];
iv. simple equipment and relatively low operational costs [59];
v. allows control over thin film stoichiometry and microstructure [59], and
vi. ability to vary the deposition conditions [59].

Rare-earth doped and undoped ZnO powders can be prepared using the solution combustion [2], solid-state reaction [60] and chemical bath deposition [9] methods. In the solution combustion technique, the precursors go through a combustion process in a pre-heated furnace at 450 °C [2]. High decomposition temperatures render this technique unattractive due to the high energy costs [2]. The solid-state reaction method is based on a diffusion process where the precursor powders react at a constant temperature above 1000 °C [61]. This temperature facilitates the reaction and diffusion of the precursors however

without any melting of the reactants [61]. The major drawbacks of the solid-state reaction [61] method are:

i. inhomogeneity in the final product;
ii. high temperatures for efficient powder reactions (>1 000 °C);
iii. large particle sizes which promote luminescence quenching defects, and
iv. numerous thermal recycling and mechanical processing cycles.

The chemical bath deposition involves reacting precursor solutions in a water bath resulting in a precipitate [9,62]. The precipitate is then dried under ambient conditions forming the required powder. This technique was used as the preferred preparation method due to its simplicity and the relatively low synthesis temperature (80 °C) [9,62] over a reaction time of five minutes.

The structures of the ZnO thin films, the undoped and rare-earth doped ZnO powders were characterized using the grazing incidence X-ray diffraction geometry in a Bruker AXS D8 Discover diffractometer. The powders were further characterised for morphology and composition by scanning electron microscopy (SEM) and energy dispersive spectroscopy (EDS), respectively, using the FEI QUANTA 200 instrument. The luminescence properties of the two forms of ZnO samples were investigated using the three blue-laser excitation lines of the Spectra Physics 2080 argon ion laser. A detailed discussion of each of the above experimental techniques is presented in the subsequent sections. The results of the measurements conducted on the ZnO thin films and rare-earth doped ZnO powders are discussed and analysed in chapters four and five, respectively.

3.2. Thin film synthesis using radio-frequency magnetron sputtering

A typical radio-frequency (rf) magnetron sputter system constitutes two parallel electrodes a fixed distance apart. The target is mounted on one of the electrodes (cathode) while the substrate is attached onto the other electrode as shown in figure 3.1. The target consists of the material to be deposited and the substrate is the wafer on which film deposition occurs. The substrate (anode) is usually

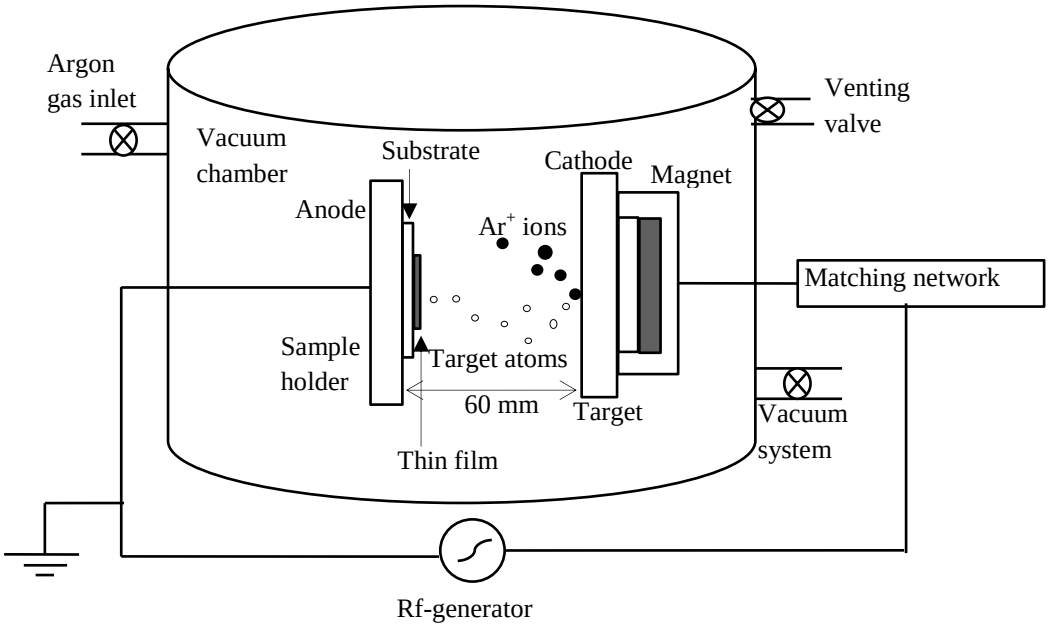

Figure 3.1 A schematic illustration of the configuration inside the deposition chamber of the radio-frequency magnetron sputtering system.

grounded (figure 3.1) however it can also be biased using a positive or negative floating potential. The bias voltage is useful for pre-etching of the substrate before deposition for improved substrate-film adhesion as well as implantation of Ar^+ or other plasma species. For thin-film growth, the deposition chamber is evacuated to the required base pressure (~1.0×10^{-5} mbar) and an inert gas (argon) is bled in as a medium through which a glow discharge is ignited [63]. The argon gas is then ionized using an rf signal superimposed on a negative DC self-biased target. This ignites a self-sustained visible glow discharge of Ar^+ ions as shown in figure 3.2 (b). The magnets behind the target (figure 3.1) provide a field that confines the electrons within the argon gas plasma increasing the ionization probability [8]. The negative potential on the target extracts the Ar^+ ions from the plasma, accelerating them towards the target material. When the Ar^+ ions collide with the target they eject atoms through a momentum transfer process [63] as shown in figure 3.1. The ejected target atoms then float across, through the plasma, to deposit on the substrate. If the ejected atoms have very high kinetic energy, re-sputtering may occur i.e. already deposited atoms are ejected by the incoming atoms [63].

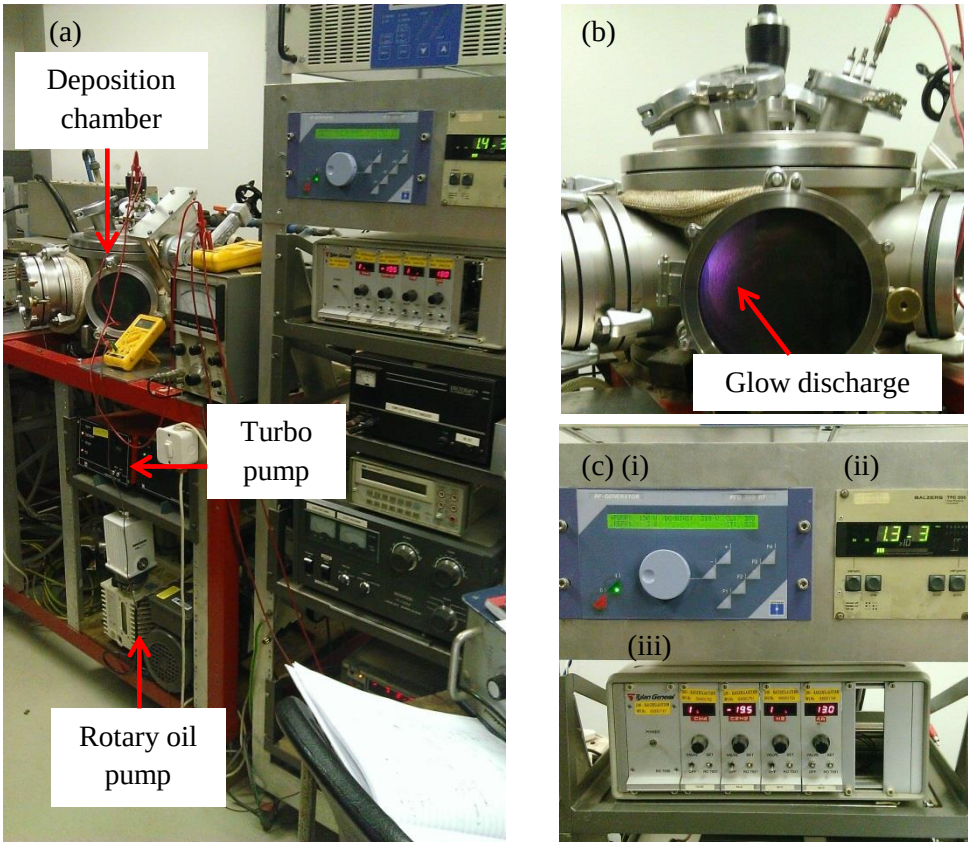

Figure 3.2 The radio-frequency magnetron sputtering system used for the deposition of the ZnO thin films: (a) The deposition system with the components as labelled. (b) The deposition chamber showing the visible glow discharge. (c) The supporting electronics: (i) radio-frequency generator, (ii) digital pressure gauge and (iii) argon/nitrogen gas flow controller.

This normally occurs at relatively high deposition powers of above 400 W and needs to be avoided as re-sputtering counters the thin film deposition process. ZnO thin films were deposited using the rf magnetron sputtering method in the thin films laboratory, in the School of Physics at the University of the Witwatersrand, Johannesburg. A 98.0 % zinc oxide target doped with 2.0 % aluminium of 99.9 % purity was used for the deposition process. The thin films were prepared on rectangular quartz substrates. Glass substrates were avoided as they were found to be luminescent in the same spectral region as the ZnO thin films. Before deposition, the quartz substrates were cleaned using detergent and water, rinsed with acetone in an ultrasonic bath for five minutes and then blow dried with ultra-pure nitrogen gas. The target and substrate are mounted in the

deposition chamber (figure 3.2 (a)) at a fixed separation of 60 mm as shown in figure 3.1. The chamber is initially evacuated using a rotary oil pump (figure 3.2 (a)) to a vacuum pressure of 5.0×10^{-2} mbar. An optimum vacuum pressure of 1.0×10^{-5} mbar is then attained using a turbo-molecular pump (figure 3.2 (a)). High purity argon gas is then bled into the chamber and the rf generator with an output frequency of 13.56 MHz is switched on to ignite the plasma. The target is pre-sputtered for five minutes to remove any adsorbates on its surface prior to deposition. A deposition pressure of 1.3×10^{-3} mbar was used to grow the ZnO thin films at a constant argon gas flow rate of 13.0 sccm (standard cubic centimetres per minute). All the ZnO films were deposited at room temperature (300 K) for two hours. A set of ZnO thin films was grown at 100 W, 150 W and 200 W RF powers with no substrate bias while another set was deposited at a constant RF power of 150 W and negatively DC biased substrates. DC substrate bias voltages of 0 V, -25 V, -50 V and -75 V were used. A ZnO film was also deposited in an argon/nitrogen gas environment with an Ar_2/N_2 gas flow rate ratio of 1:1 (i.e. 13 sccm: 13 sccm). After deposition, the films were left for an hour to allow them to gradually cool down before being removed from the deposition chamber. This minimized the thermal stress developed by rapid quenching to room temperature. The deposition rate of the sputter system was established to be 14.4 nm, 22.8 nm and 30.5 nm per minute for 100 W, 150 W and 200 W deposition powers, respectively. At 2 hour deposition times, the resulting films had thicknesses of about 1 700 nm, 2 700 nm and 3 700 nm for the respective deposition powers.

Post-deposition heat treatment was carried out using the isothermal annealing procedure. This involves gradual heating of the sample from a reference temperature (in this case room temperature) to a chosen set point temperature. The set point temperature is kept constant for the required dwell time and then the sample is left to gradually cool down. Gradual heating is normally applied to poor thermal conducting materials in order to prevent thermal shock or cracking of the sample. The thin films deposited in this study were annealed at 600 °C in air, for 2 hours [64] at a heating rate of 10 °C per minute. The annealing process

improves the crystallinity of the ZnO thin films [65]. A summary of the prepared ZnO thin films is given in table 3.1.

Table 3.1 Summary of the ZnO thin films prepared using various deposition parameters.

RF power (W)	DC substrate bias voltage (V)	Working gas flow rate (13 sccm)
100 W	-	Ar_2
150 W	-	Ar_2
150 W	-	Ar_2/N_2 (1:1)
150 W	-75	Ar_2
150 W	-50	Ar_2
150 W	-25	Ar_2
200 W	-	Ar_2

3.3 Powder synthesis (The chemical bath deposition method)

The chemical bath deposition method was utilized to synthesize Eu^{3+} and Tb^{3+} doped and pristine ZnO powders. The samples were prepared at the Department of Physics, University of the Free State (UFS), Qwaqwa campus. An additional separately-prepared 1.0 mol% Tb^{3+} doped ZnO sample was kindly provided by Professor Dejene of UFS. The concentrations and quantities of the precursor elements were based on optimization studies that had been carried out by Koao et al. [62]. The precursors were analytical grade zinc acetate (Zn $(CH_3COO)_2 \cdot 2H_2O$), thiourea ($(NH_2)_2CS$), ammonia (25% NH_3) and either terbium nitrate (Tb $(NO_3)_3 \cdot 6H_2O$) or europium acetate ($Eu(CH_3COO)_3 \cdot 2H_2O$); the starting quantities were measured so as to yield a 0.2, 0.5 and 1.0 mol% RE^{3+} dopant concentration.

For the pristine ZnO powder, 7.375 g of zinc acetate was dissolved in 60 ml of deionized water to obtain a 0.56 M concentration of zinc acetate solution. A separate solution of 0.18 M concentration was prepared by dissolving 6.851 g of

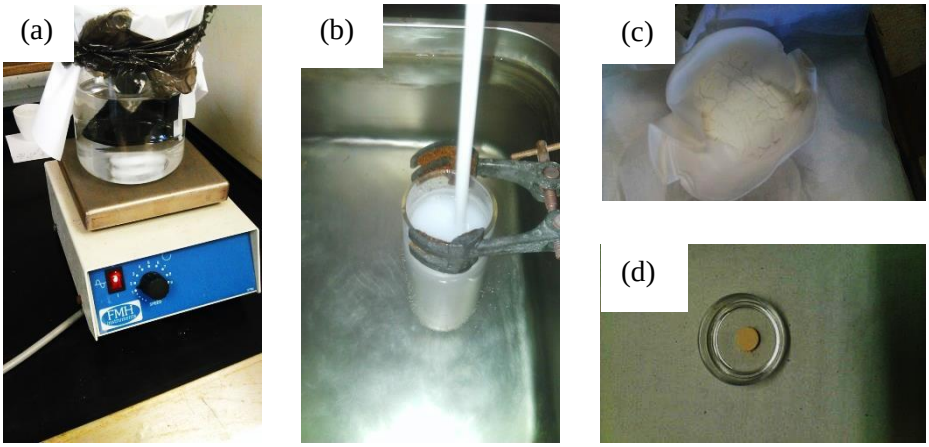

Figure 3.3 The setup and preparation process for pristine ZnO, Eu^{3+}-doped and Tb^{3+}- doped ZnO powders: (a) Magnetic stirrer used to mix the precursor solutions. (b) The water bath in which the solutions were reacted. (c) The white powder obtained after filtering and drying the precipitate. (d) The pelletized sample.

thiourea in 500 ml of deionised water. Using the same amount of deionised water a separate solution of ammonia was prepared by mixing 123.5 ml of 25 % aqueous ammonia. Of the two 500 ml solutions only 60 ml of each was used for preparing the sample. The solutions were each stirred for 30 minutes with a magnetic stirrer as shown in figure 3.3(a) and left standing for at least 8 hours to ensure homogeneity. The solutions were then reacted in an 80 °C water bath (figure 3.3 (b)) starting with zinc acetate then thiourea and finally ammonia solutions in volume ratios of 60 ml : 60 ml : 60 ml while continuously stirring for 5 minutes to obtain a precipitate of pristine ZnO. The resulting precipitate was removed from the water bath and left to settle for at least 8 hours before it was filtered, washed with ethanol and acetone and then left to dry under ambient conditions for a week. The final product was a white powder as shown in figure 3.3 (c).

For the RE^{3+} doped ZnO powders, preparation of the 1.0 mol% Eu^{3+} and the 1.0 mol% Tb^{3+} doped ZnO samples was carried out using the same procedure as above, with the addition of either 0.111 g of europium acetate or 0.153 g of terbium nitrate to the zinc acetate precursor before dissolving in 60 ml of deionised water. For the Eu^{3+} doped sample, the resulting powder had an orange like appearance (figure 3.3 (d)) which may be attributed to the addition of the

Eu^{3+} dopant ions. The 0.2 and 0.5 mol% concentrations were achieved by adding proportionate amounts of terbium nitrate or europium acetate.

The Tb^{3+} doped ZnO powders obtained from the above procedure did not give any terbium related results while the 1.0 mol% Tb^{3+} doped ZnO sample donated by Professor Dejene yielded positive results. The initial ZnO:Tb^{3+} powders, prepared at the same time as the undoped and Eu^{3+} doped ZnO powders as detailed above, will hereafter be referred to as the A sample (i.e. ZnO:Tb^{3+} (A)) while the donated sample will be identified as the B sample (i.e. ZnO:Tb^{3+} (B)). For this B sample, the same precursor quantities and concentrations as for the A sample were used. However, after the chemical bath reaction the resulting precipitate was immediately filtered and washed with ethanol and acetone instead of being left to settle for at least 8 hours. The filtrate was still left to dry for a week under ambient conditions. The only difference between the two methods is at the filtering stage; the precipitate for the A sample was left to settle for at least 8 hours before filtration whereas that for the B sample was filtered immediately after it was obtained. It has not yet been established why terbium could not be incorporated into the ZnO with the first procedure although europium was successfully incorporated. Due to time constraints, an undoped ZnO reference sample could not be prepared using the second procedure.

From the resulting powders, 300 mg of each were compacted using a hydraulic press at 80 kN to obtain a pellet of diameter 8 mm and thickness 2 mm, as shown in figure 3.3 (d).

Table 3. 2 Summary of the precursor quantities used to prepare the ZnO powders.

Sample	Dopant precursor mass (g) for 1 mol%	Zinc acetate mass (g)	Precipitate idle time before filtration (hours)
ZnO	-	7.375	8
ZnO:Tb^{3+} (A)	0.153	7.375	8
ZnO:Tb^{3+} (B)	0.153	7.375	-
ZnO:Eu^{3+}	0.111	7.375	8

This made handling of the samples easier. The pelletized samples were annealed in air at a temperature of 700 °C for 2 hours. Annealing at temperatures below 700 °C was found not to eradicate the precursor XRD peaks in the ZnO powders [66]. Table 3.2 summarises the quantities used to prepare the pristine ZnO, Tb^{3+} and Eu^{3+} doped ZnO powders together with the filtration procedure.

3.4 Sample characterisation

3.4.1 Scanning electron microscopy and energy dispersive spectroscopy

A typical scanning electron microscopy (SEM) unit consists of an electron-beam source coupled to a column of electron lenses, a specimen chamber with a stage for mounting the sample, a set of detectors (back scattering electron detector-BSED, secondary electron detector-SED and an X-ray spectrometer) and a user control interface [67]. From this system, SEM images that show the morphology of the samples can be obtained together with the qualitative elemental composition. This is obtained through the application of energy dispersive spectroscopy (EDS) incorporated in the SEM unit. The two characterisation techniques depend on the ability of the atoms and core electrons of the constituent atoms to interact with the bombarding electrons. In addition, the samples under investigation have to be electrically conductive [67]. For SEM imaging, the electron beam from the source (filament) is focused onto the sample. The electron beam interacts with the sample to generate back-scattered electrons, secondary electrons and X-rays [67]. The back-scattered electrons are a result of reflections of the incident electron beam while the secondary electrons are emitted from the atoms on the sample surface. It is the secondary electrons detected by the secondary electron detector that give high resolution SEM images [67]. The EDS relies on the X-rays emitted by the sample atoms as a result of atomic shell transitions when outer shell electrons radiatively decay to occupy holes created by the incident electron beam in inner shells [67]. This characterisation technique is based on the principle that each atom emits characteristic X-rays of energy equivalent to the shell transitions of that particular atom [67]. The X-rays emitted by the atoms are detected by a silicon lithium (Si(Li)) detector which then relates the emission to the corresponding element.

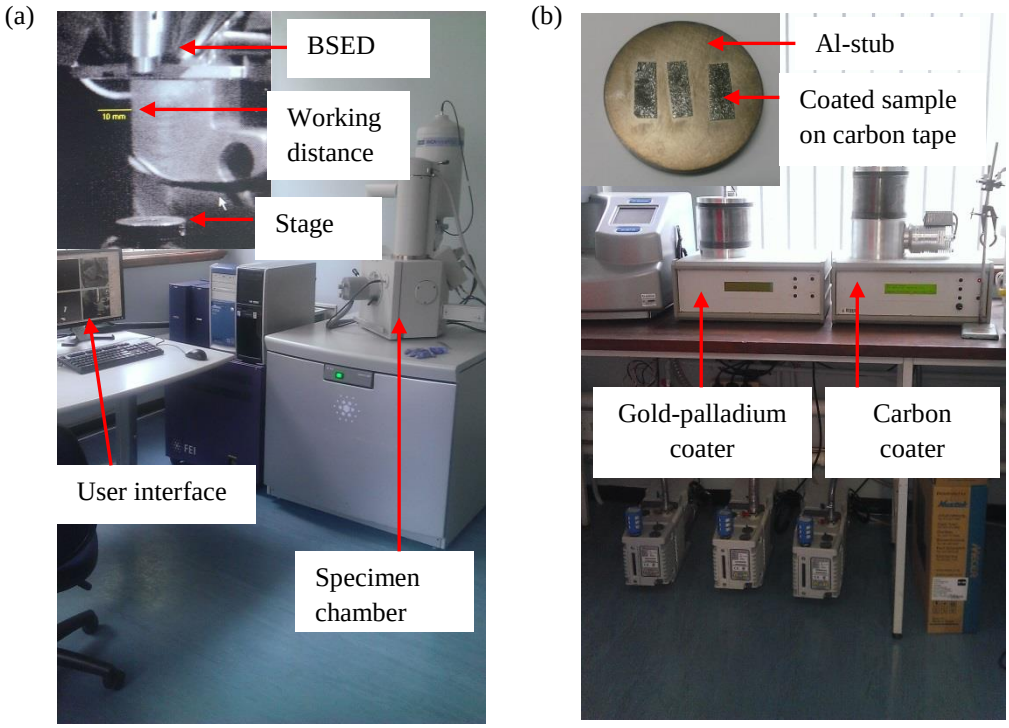

Figure 3.4 (a) The scanning electron microscopy system with the insert showing the interior of the specimen chamber and the back scattering electron detector (BSED). (b) The gold-palladium sputter coater and a typical gold-palladium coated sample on an aluminium (Al) stub (insert).

To determine the morphology and the elemental composition of the RE^{3+} doped ZnO powders obtained from the chemical bath deposition method (discussed above), SEM and EDS measurements were, respectively, carried out using the FEI QUANTA 200 instrument (figure 3.4 (a)). The characterisation measurements were conducted in the Microscopy and Microanalysis Unit in the School of Molecular and Cell Biology, at the University of the Witwatersrand, Johannesburg. For these measurements, the sample powder is firstly mounted onto an aluminium stub using carbon tape and then coated with a 5 nm thick layer of gold-palladium alloy (60 % -gold, 40 % -palladium) as shown in the insert of figure 3.4 (b), using a Quorum K550X EMITECH sputter coater system (figure 3.4 (b)). The gold-palladium coating is useful for increasing the conductivity of the samples. The coated sample is placed on the specimen stage (figure 3.4 (a) insert) in the specimen chamber which is then evacuated to 4.0×10^{-3} Pa. The mounted sample is raised to a working distance of 10.0 mm below the BSED (figure 3.4 (a) insert) for the measurements. SEM images and

EDS spectra of the as-prepared and the annealed powders presented in chapter five were obtained using an emission current of 20 μA and a bias voltage of 16 kV.

3.4.2 Grazing incidence X-ray diffraction characterisation

Diffraction in materials occurs if the atoms of the sample material are arranged in periodic arrays over long atomic distances (i.e. crystalline materials) [68]. The wavelength of the incident radiation should be similar to the separation between neighboring atoms hence the use of X-rays. When an incident X-ray beam is directed towards a sample material, the atoms of the sample will scatter the incident X-rays, generating a diffraction pattern. This diffraction pattern will form in positions where the scattered X-rays undergo constructive interference. It constitutes diffraction peaks whose pattern is a signature of the crystal structure unique to the material under investigation [68]. For constructive interference to occur, the scattered X-rays must satisfy Bragg's law [68] given in equation (3.1):

$$n\lambda = 2d_{hkl}\sin\theta \tag{3.1}$$

where λ is the wavelength of the monochromatic X-ray, θ is the Bragg angle, n is the order of diffraction and d_{hkl} is the inter-planar distance. The position of the diffraction peak relies on the inter-planar distance (d_{hkl}) between successive diffraction planes and the wavelength of the incident radiation (figure 3.5). In

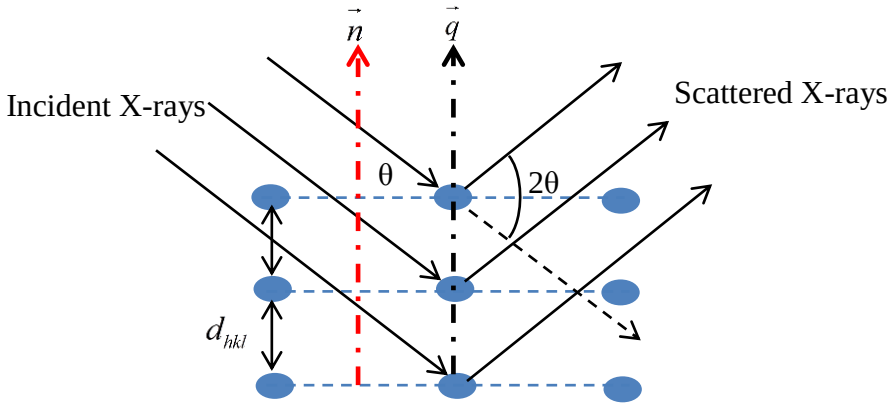

Figure 3.5 A schematic illustration of X-ray diffraction by a crystal of inter-planar distance d_{hkl}.

addition, for a diffraction peak to be observed the planes need to be aligned in such a way that the normal to the plane ($\vec{n}$) is parallel to the scattering vector ($\vec{q}$) (diffraction vector) bisecting the incident and the scattered X-rays as shown in figure 3.5 [68]. Different plane orientations result in different 2θ diffraction peaks. These planes are denoted by the *h k l* Miller indices.

In this study, the grazing incidence X-ray diffraction geometry was used to characterize pristine ZnO thin films, ZnO powder and rare-earth doped ZnO powders. For a thin film, the Seeman-Bohlin geometry [69] (figure 3.6) minimizes the substrate contribution to X-ray scattering through variation of the incidence angle, thus making the technique surface selective [70]. In grazing incidence

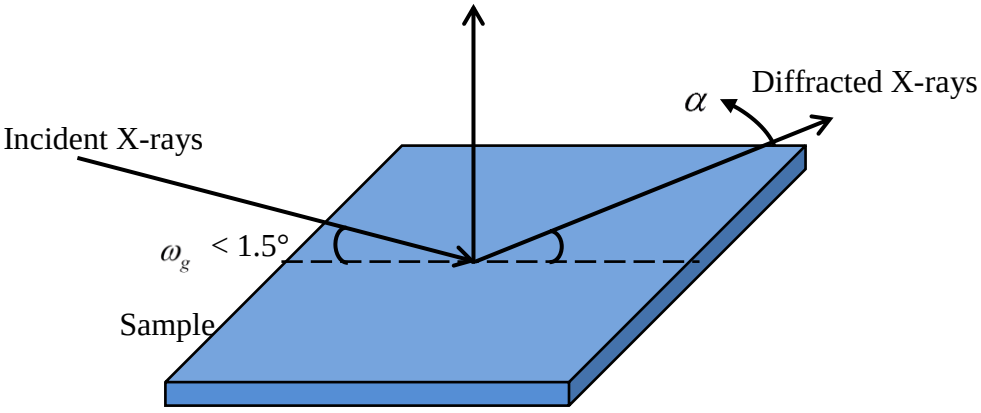

Figure 3.6 A schematic diagram of the grazing incidence X-ray diffraction geometry with the diffracted X-rays detected over angular scans (α).

X-ray diffraction, an incidence angle of $\omega_g < 1.5°$ (figure 3.6) is used to realize X-ray diffraction from the sample surface [70]. The exact value of the incidence angle from the afore-stated range depends on the electron density of the substrate, in the thin films case, and the X-ray energy [70]. This geometry is restricted to samples with very smooth surfaces [70]. Furthermore, the diffraction peaks are generally of low intensity due to the limited scatter volume as the incident X-rays interact with a limited sample volume [70]. The penetration is highly dependent on the incident angle [70]. The grazing incidence XRD measurements were conducted in the School of Chemistry at the University of the Witwatersrand, Johannesburg. For the XRD measurements, the 0.154 nm Cu K_α line of the

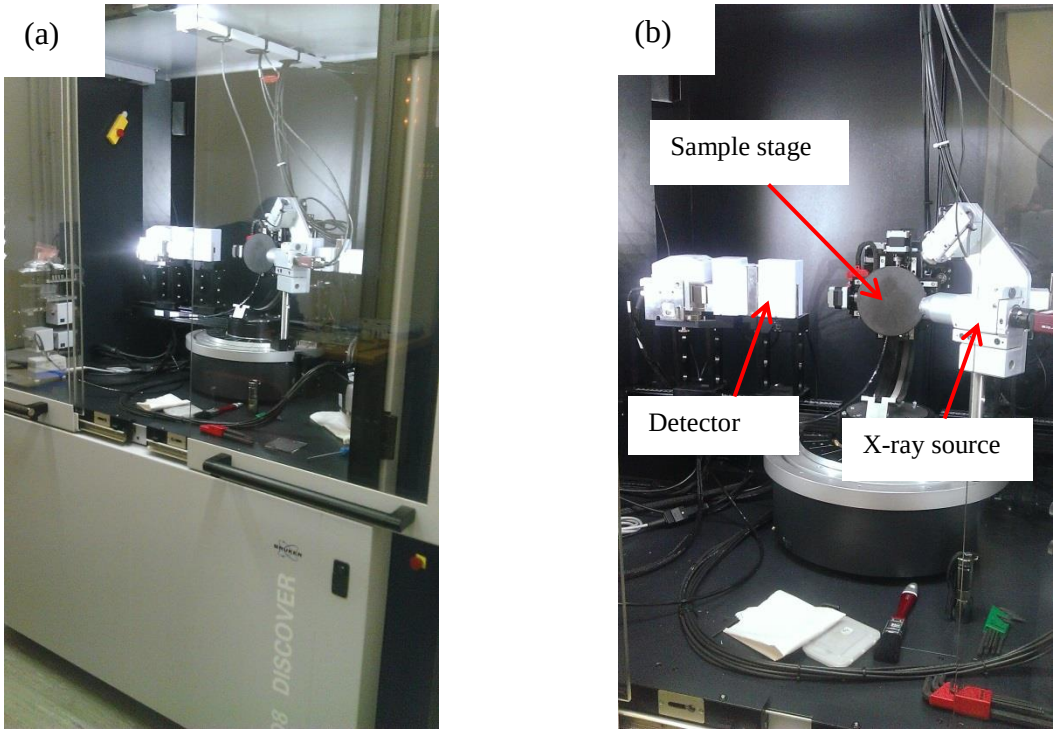

Figure 3.7 (a) The AXS Bruker D8 Discover X-ray diffraction instrument. (b) A close up showing the respective components as labelled.

Bruker AXS D8 Discover (figure 3.7) at $\omega_g = 1°$ was used. The measurements were carried out in the range $15° \leq 2\theta \leq 80°$. The XRD patterns obtained for the ZnO thin films and rare-earth doped ZnO powders are presented and discussed in chapters four and five, respectively.

3.5 Blue-laser excitation

The laser excited photoluminescence measurements for the ZnO thin films and the RE^{3+} doped ZnO powders were conducted in the fluorescence spectroscopy laboratory, in the School of Physics at the University of the Witwatersrand, Johannesburg (figure 3.8). The 457.9 nm, 476.5 nm and 488.0 nm excitation lines were available for the photoluminescence measurements. The experimental setup shown in figures 3.8 and 3.9 was used for both the ZnO thin films and ZnO powders. The emission was detected using a Burle C31034-A02 photomultiplier tube coupled to a high resolution McPherson 2062DP monochromator. The signal from the photomultiplier tube was amplified by an SRS preamplifier and

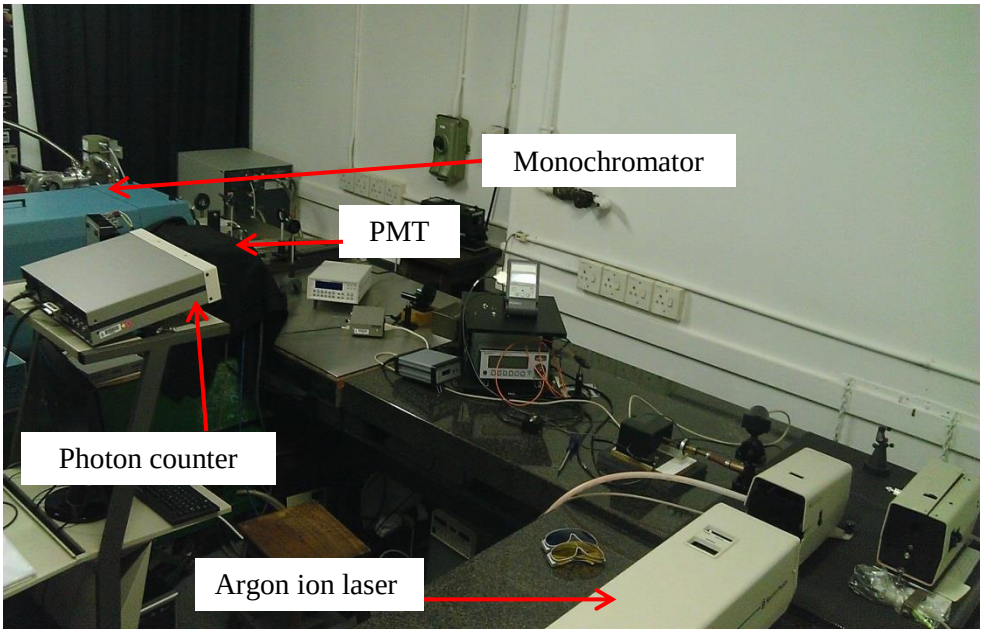

Figure 3.8 The fluorescence spectroscopy setup.

then transmitted to a photon counter. Typically, laser powers of 35 mW and monochromator slit-widths of 250 μm were used.

For the ZnO thin films, room temperature photoluminescence measurements were conducted on samples prepared under different deposition conditions (table 3.1) using the 488.0 nm excitation line. Spectra of the ZnO thin film deposited at 150 W RF power in an Ar_2 gas flow ambient at 0 V bias voltage were also obtained with the 476.5 nm and the 457.9 nm excitation lines so as to establish the effect of varying the excitation energy. The spectra were recorded in the range 500.0 – 900.0 nm using a 20 s integration time. The photoluminescence emission intensity was low hence a long integration time was required for the measurements. The reflection configuration (i) shown in figure 3.9 was used since the emission from the ZnO films could be easily focused on to the entrance slit of the monochromator. A discussion and analysis of the resulting photoluminescence spectra is presented in chapter four.

For the ZnO powders, room temperature (300 K) photoluminescence measurements were carried out on the pellet samples, using the 457.9 nm, 476.5 nm and 488.0 nm excitation lines of the Spectra Physics 2080 argon ion laser. In addition, some spectra were recorded with the 476.5 nm and 488.0 nm wavelengths after cooling the samples to 10 K. For the 10 K measurements, the

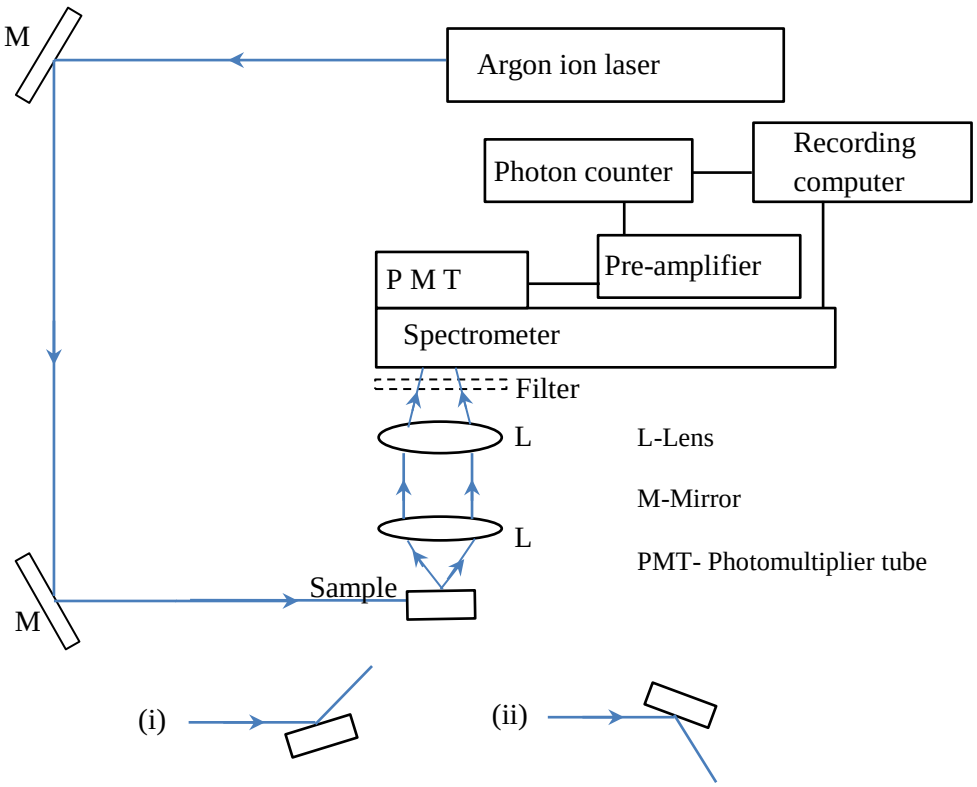

Figure 3.9 A schematic illustration of the photoluminescence experimental arrangement. Sample configuration (i) made use of a filter while (ii) did not require a filter.

pellets were mounted in a Janis CCS-150 cryostat that was evacuated to below 1.4×10^{-4} mbar. A LakeShore 331 controller was used to monitor the temperature at the sample. Spectra were recorded in the range 460.0 – 900.0 nm using 2 s integration times. The photoluminescence emission signal was relatively high hence short integration times were adequate for the measurements. The spectra were obtained with either the 515 nm long-pass filter using the configuration in figure 3.9 (i) or the geometry in figure 3.9 (ii) for which a filter was not required. The configuration in figure 3.9 (ii) was particularly useful for observing the $^5D_4 \rightarrow {}^7F_6$ emission band of the Tb^{3+} ion. The discussion and analysis of the laser excited photoluminescence spectra obtained for the ZnO powders is presented in chapter five.

Chapter 4

XRD and blue-laser excited photoluminescence studies of ZnO thin films

4.1 Introduction

The unique electrical and optical characteristics of ZnO thin films over other semiconductors have stimulated continued research interest in the material for optoelectronic applications [6]. ZnO has been identified as a potential candidate for the development of diode lasers [11], more efficient photovoltaic cells [71] and other optoelectronic devices as indicated in section 1. It has also been used as a host for RE^{3+} dopants as it provides a wide absorption band which is useful for energy transfer to the RE^{3+} ions for up-conversion and down-conversion in solar cells [71,72]. For the above applications to be realised, an in-depth understanding of the origins of the optoelectronic properties of ZnO is paramount. This requires an investigation of the intrinsic defects associated with ZnO as these are responsible for its optical and electrical characteristics. Furthermore, an understanding of the effects of the preparation conditions on the properties of ZnO thin films is useful as they influence the type of defects formed [73]. The ZnO thin films under study were deposited using radio-frequency (RF) magnetron sputtering. This technique was used as it presents several advantages as previously discussed in section 3.1.

In the literature, photoluminescence results of ZnO thin films obtained with ultra-violet excitation have shown emission in the ultra-violet and visible regions of the electromagnetic spectrum [59,40]. Ultra-violet excitation energy is sufficient for valence band (VB) to conduction band (CB) electron excitation. The excited electrons decay radiatively from the near CB edge to the VB resulting in the observed ultra-violet emission [39]. Some of the electrons undergo non-radiative transitions from the CB to defect levels within the ZnO band gap and then radiatively decay thereafter [39]. It is these defect level transitions that result in the observed visible emission [39,40]. Most photoluminescence studies of ZnO thin

films have been focused on ultra-violet excitation (30 769 cm^{-1} – 26 316 cm^{-1} (325.0 nm – 380.0 nm)) as this enables the population of the CB [39,59,40]. This has prompted the need to investigate direct excitation of the defect transition levels by using below bandgap excitation energies.

In this study, ZnO thin films were deposited under different RF magnetron sputter conditions. This was done so as to determine the effect of growth parameters on the structural and photoluminescence properties of the ZnO films. The structural properties of the ZnO thin films were characterized using grazing incidence X-ray diffraction while the photoluminescence properties were investigated using below bandgap excitation energies (blue-laser excitation). From the photoluminescence results, the relevant intrinsic defect levels and their associated defect level transitions responsible for the ZnO luminescence will be presented.

4.2 Results and discussion

4.2.1 XRD characterisation

The grazing incidence XRD patterns of annealed and as-prepared ZnO thin films deposited on quartz, in an Ar_2 (13 sccm) ambient, for two hours at 100 W RF power are as shown in figure 4.1. The ZnO thin film annealed at 600 °C for two hours in air yields relatively intense and slightly narrow diffraction peaks (figure 4.1 (i)). The XRD pattern for the annealed ZnO thin film shows diffraction peaks at 32.0°, 34.2°, 36.8°, 47.8°, 56.6°, 63.3°, 68.4° and 77.1° corresponding to the (1 0 0), (0 0 2), (1 0 1), (1 0 2), (1 1 0), (1 0 3), (1 1 2) and (2 0 2) diffraction planes, respectively (figure 4.1 (i)). An error estimate of ±0.1° was deduced from the measured XRD 2θ values. The as-prepared ZnO film yielded fewer XRD peaks at 31.5°, 56.0°, 62.5°, 67.4° and 76.2° which are relatively broad and have low intensity in comparison (figure 4.1 (ii)). This is an indication of nano-crystalline sized grains in an amorphous matrix [68]. The corresponding diffraction peaks of the annealed ZnO thin film show a general shift towards higher 2θ angles (32.0°, 56.6°, 63.3°, 68.4° and 77.1°) relative to the 2θ angles of the as-prepared ZnO thin film. The shifting of the diffraction peaks towards higher 2θ angles after annealing indicates the removal of inherent

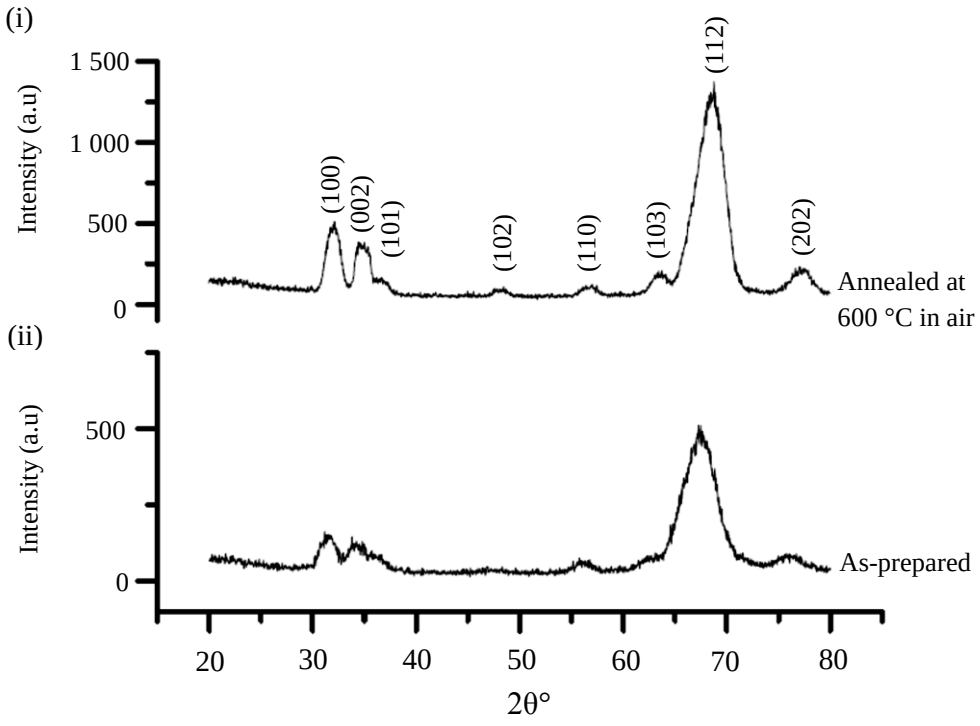

Figure 4.1 The XRD patterns for (i) annealed and (ii) as-prepared ZnO thin films deposited at 100 W RF power.

stresses associated with the as-grown ZnO film [30]. The XRD patterns for both the as-prepared and the annealed ZnO films show the peak at 67.4° and 68.4°, respectively, associated with the (1 1 2) diffraction plane as the dominant peak. Both XRD patterns present the (1 0 0), (0 0 2) and (1 1 2) planes as the preferred growth orientations with the (1 1 2) plane being dominant. The very weak XRD peaks for the as-prepared sample are attributed to misalignment of the diffraction planes during the growth process such that the Bragg condition for diffraction is not satisfied. The heat treatment may have caused re-alignment of the planes resulting in stronger peaks for the annealed ZnO thin film (figure 4.1 (i)). For the as-prepared ZnO film, the linewidths in milliradians (full width at half maximum-FWHM) for the (1 0 0), (0 0 2), (1 1 0), (1 1 2) and (2 0 2) peaks are 3.49, 3.0, 3.39, 6.25 and 5.48, respectively. The corresponding linewidths in milliradians (FWHM) for the annealed ZnO sample are 2.76, 2.76, 3.0, 5.58 and 3.91, respectively, which shows a decrease in the linewidth due to post-deposition annealing. In the literature, increases in diffraction intensity and narrowing of the linewidth have been shown to be a result of enhanced crystallinity in the annealed ZnO thin film [74]. Based on the improved XRD

pattern obtained from the annealed sample, all the ZnO thin films were annealed under the same conditions as above.

XRD patterns of annealed ZnO thin films deposited at 200 W and 150 W RF power in an Ar_2 gas flow (13 sccm) environment for two hours are presented in figure 4.2. The spectrum for the ZnO film obtained at 100 W (figure 4.1) is included for comparison. For the ZnO thin film obtained with 200 W deposition power, most of the diffraction peaks associated with the ZnO wurtzite structure are observed with relatively uniform intensity as shown in figure 4.2 (i). The ZnO thin film deposited at 150 W yields XRD peaks at 31.7°, 36.3°, 56.5°, 68.2° and 76.9° corresponding to the (1 0 0), (1 0 1), (1 1 0), (1 1 2) and (2 0 2) planes, respectively (figure 4.2 (ii)). These 2θ angles are consistent with those for the annealed ZnO thin film deposited at 100 W (figure 4.2 (iii)). However peaks at 34.6°, 47.8° and 62.5° associated with the (0 0 2), (1 0 2) and (1 0 3) planes are relatively weak for the 150 W sample. The ZnO thin film deposited at 100 W (figure 4.2 (iii)) gave similar XRD peaks as for the sample deposited at 150 W. As the RF deposition power is increased from 150 W to 200 W the intensity of

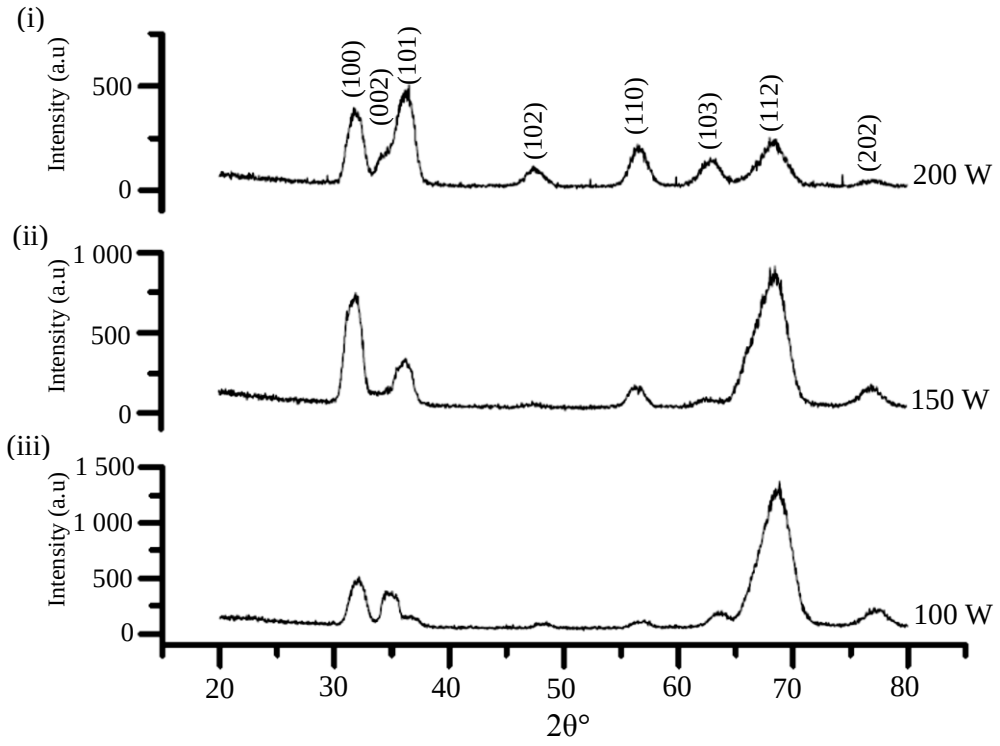

Figure 4.2 XRD patterns for ZnO thin films annealed at 600 °C in air and deposited at RF powers of (i) 200 W, (ii) 150 W and (iii) 100 W.

the diffraction peak at 68.4° corresponding to the (1 1 2) plane decreases while the peaks at 31.7° and 36.3° due to the (1 0 0) and (1 0 1) planes, respectively, gain in intensity. This shows that for the sputter system used in this work, growth in the (1 0 0) and (1 1 2) direction is favourable at low RF deposition powers while at high deposition powers a more random distribution in the plane growth of the films is obtained. In the literature, experimental work on ZnO thin films where RF power is varied has shown an increase in XRD peak intensity with increase in RF power [75,76,77]; the intensity however reaches an optimum at 200 W and then decreases with further increase in RF power [75,76]. This decrease in intensity with increase in RF power can be attributed to re-sputtering of the deposited film. The kinetic energy of the incoming atoms increases with increasing deposition power such that they can knock off already deposited atoms on collision [75]. This results in amorphous and randomly oriented thin film growth as indicated by the relatively low intensity peaks in the XRD pattern of the sample deposited at 200 W (figure 4.2 (i)).

Of the three ZnO thin films deposited at various RF powers, the film obtained at 200 W yielded an evenly distributed XRD peak intensity. However the sample had a poor film-substrate adhesion resulting in the ZnO film peeling off the substrate. The 150 W RF deposition power yielded a ZnO thin film with a good film-substrate adhesion. The ZnO film obtained at 100 W deposition power also had a good film-substrate adhesion and gave the most intense XRD peaks, it however had a poor response in preliminary photoluminescence investigations. Therefore a deposition power of 150 W was chosen as the most suitable over the 100 W and the 200 W.

Annealed ZnO thin films obtained with 150 W deposition power and 0 V, -25 V, -50 V and -75 V substrate bias voltages, in an Ar_2 ambient, were also characterised using grazing incidence XRD and the patterns are presented in figure 4.3. The XRD pattern obtained for the film deposited at -75 V bias voltage shows the (1 1 2) phase at 68.2° as the only dominant peak with the lower 2θ angle peaks having relatively low intensities (figure 4.3 (i)). As the negative bias voltage is decreased from -75 V to -50 V and then to -25 V, the (1 1 2) peak is supressed while the intensities of the (0 0 2) and (1 0 3) peaks at 34.6° and 62.5°,

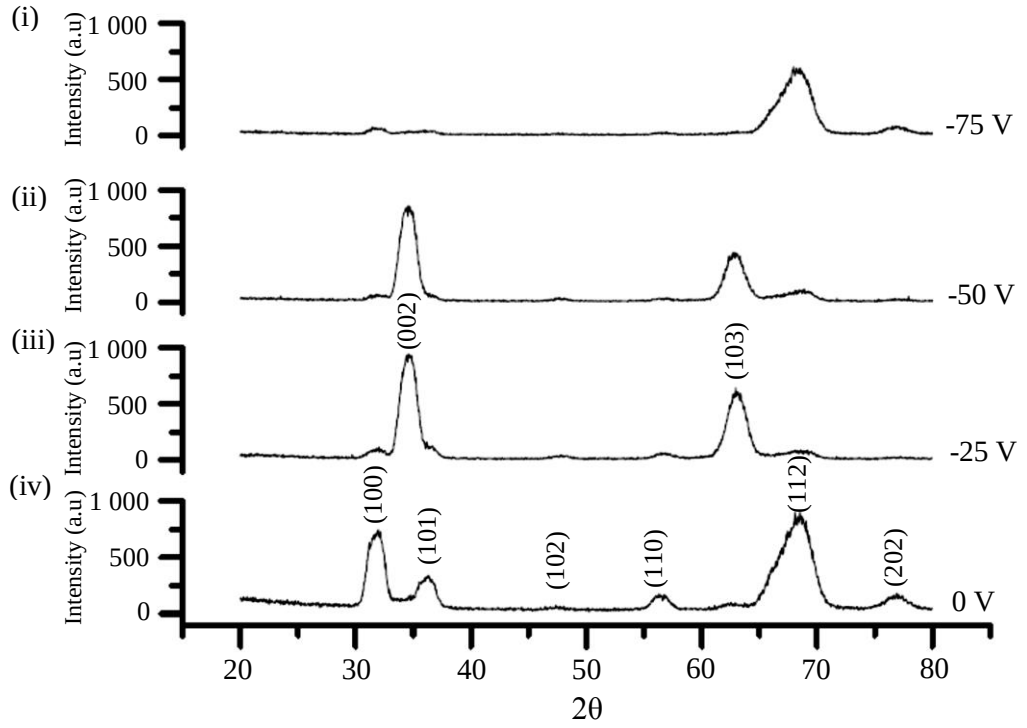

Figure 4.3 XRD patterns for annealed ZnO thin films deposited using an RF power of 150 W at substrate bias voltages of (i) -75 V, (ii) -50 V, (iii) -25 V and (iv) 0 V.

respectively, are increased as shown in figures 4.3 (ii) and (iii). At 0 V (no bias), the XRD pattern shows relatively intense peaks at 31.7°, 36.3° and 68.2° corresponding to the (1 0 0), (1 0 1) and (1 1 2) planes, respectively, (figure 4.3 (iv)). From the XRD patterns, the ZnO thin films obtained at -50 V and -25 V substrate bias voltages therefore have a (0 0 2) and a (1 0 3) preferred growth orientation while the film obtained at 0 V shows (1 0 0), (1 0 1) and (1 1 2) preferred growth directions and the sample obtained at -75 V results in a film with only a (1 1 2) plane growth orientation. Variations in substrate bias voltages affect the deposition rate resulting in changes in the XRD peak intensities with the preferred growth orientation having the most intense peak [78,79]. In addition, the negative substrate bias could also determine the selection of sputter species (e.g. Zn^{2+}, Zn^{+}, Ar^{+} and O^{+}) [80]. In the literature, at bias voltages less than -60 V, the Ar^{+} ions are attracted to the substrate together with the atoms of the material to be deposited thereby increasing the deposition rate [79]. However at high negative bias voltages (-75 V), the film thickness is

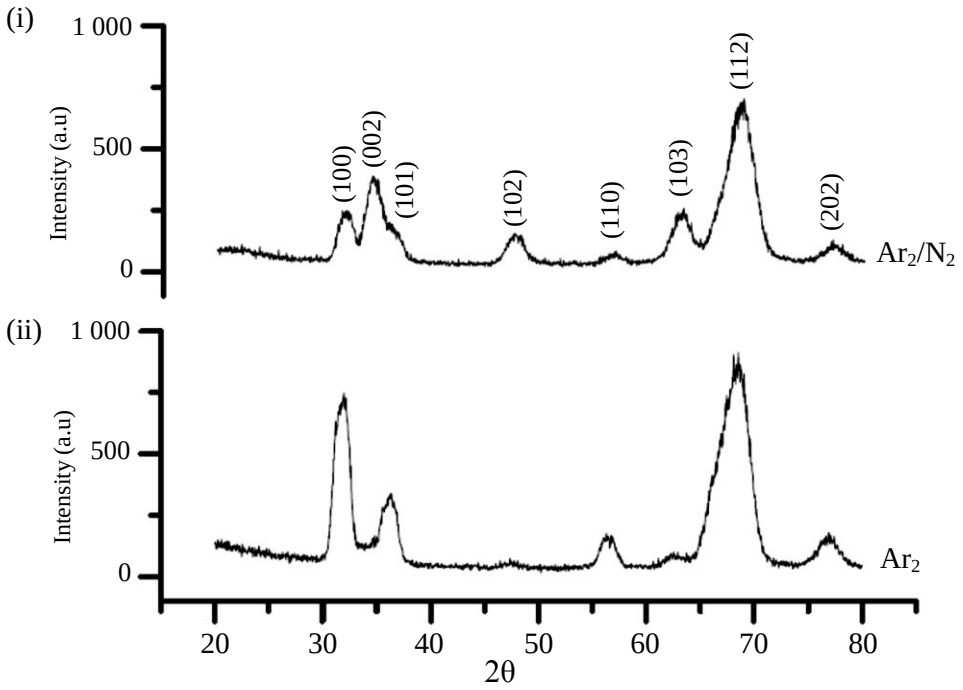

Figure 4.4 XRD patterns for annealed ZnO thin films deposited at an RF power of 150 W in (i) an Ar_2/N_2 (1:1) and (ii) an Ar_2 gas flow environment.

low due to film re-sputtering. This is because the incoming Ar^+ ions possess sufficient kinetic energy to re-sputter already deposited ad-atoms instead of being implanted into the ZnO film [79].

The XRD patterns of the ZnO thin films obtained with 150 W deposition power in an Ar_2/N_2 (13 sccm:13 sccm) and Ar_2 (13 sccm) gas flow environment at 0 V are presented in figure 4.4. The Ar_2/N_2 growth environment resulted in typical ZnO diffraction peaks as shown in figure 4.4 (i) except for a relative increase in intensity of the (1 0 2) and (1 0 3) peaks. For the ZnO film deposited in an Ar_2 gas flow environment, two dominant peaks at 31.7° and 68.2° corresponding to the (1 0 0) and (1 1 2) planes, respectively, were observed (figure 4.4 (ii)).

Generally, all the ZnO thin films yielded XRD patterns that show a wurtzite structure for the various preparation conditions. The grain sizes (*D*) for each sample were calculated using the Scherrer formula [68] (equation 4.1) where *k* is the Scherrer constant, β is the linewidth in radians (full width at half maximum-FWHM), λ is the X-ray wavelength and θ is the diffraction angle.

$$D = \frac{k\lambda}{\beta \cos\theta} \tag{4.1}$$

Only the most intense diffraction peak for each sample was considered in the calculations as the ZnO films did not yield a common diffraction peak for comparison. From the calculations, the different preparation conditions resulted in ZnO thin films with average grain sizes (D) of 5 ±1 nm.

Table 4.1 A summary of the calculated lattice constants, *c/a* ratio and the corresponding *u*-parameter for each of the ZnO thin films.

ZnO thin films	Lattice constants (±0.006 nm)		$\frac{c}{a}$	*u*-parameter
	a (nm)	*c* (nm)	(±0.04)	(±0.02)
100 W (as)	0.328	0.524	1.60	0.38
100 W (an)	0.321	0.518	1.61	0.38
150 W (an)	0.323	0.516	1.60	0.38
150 W (Ar_2/N_2, an)	0.323	0.520	1.61	0.38
150 W (-75 V, an)	0.323	0.518	1.60	0.38
150 W (-50 V, an)	0.329	0.519	1.58	0.38
150 W (-25 V, an)	0.327	0.518	1.58	0.38
200 W (an)	0.323	0.520	1.61	0.38

as – as-prepared

an – annealed at 600 °C in air

The corresponding lattice constants *a* and *c* (table 4.1) were obtained from equation 4.2 [81] while the *u*-parameter for a hexagonal structure was determined using equation 4.3 [82].

$$\left(d_{hkl}\right)^2 = \left(\frac{\lambda}{\sin\theta}\right)^2 = \frac{3a^2c^2}{4c^2\left(h^2+k^2+hk\right)+3a^2l^2} \tag{4.2}$$

$$u = \frac{1}{3}\left(\frac{a^2}{c^2}\right) + \frac{1}{4} \tag{4.3}$$

The values of the lattice constants *a* and *c* and the *u*-parameter determined in this study are comparable with the values reported in literature (*a* = 0.325 nm, *c* = 0.521 nm and *u* = 0.38) [12,83]. The values of the *c/a* ratio and *u*-parameter indicate minimum distortion of the ZnO lattice structure with change in deposition conditions. The lattice constants *a* and *c*, the *c/a* ratio and the *u*-parameter are summarised in table 4.1.

4.2.2 Laser excited photoluminescence

The photoluminescence spectra of the as-prepared and annealed ZnO thin films deposited at 100 W as well as a blank quartz substrate, obtained with the 488.0 nm excitation line are presented in figure 4.5. The spectrum for the blank

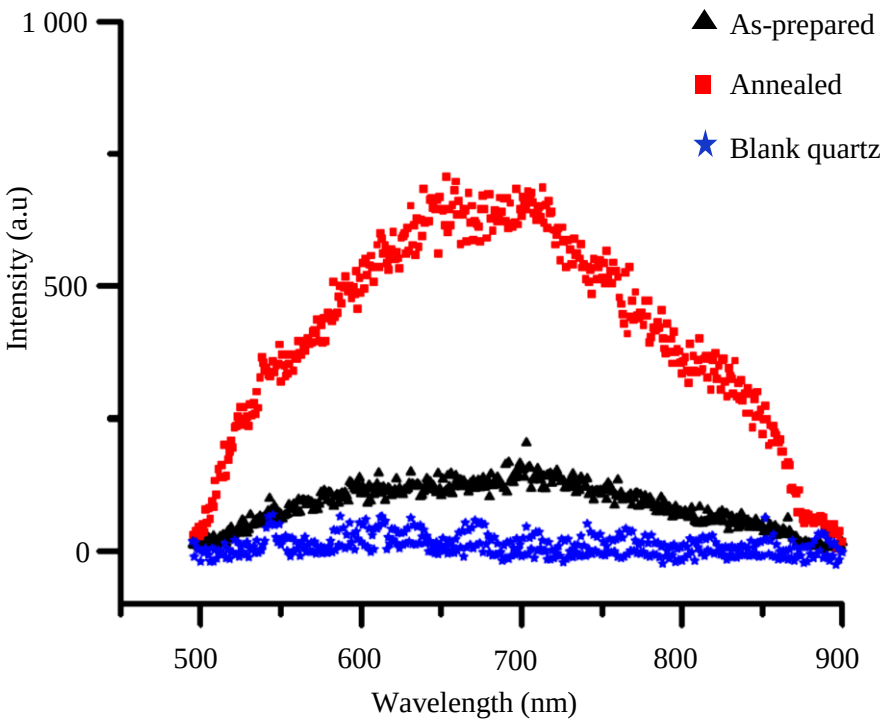

Figure 4.5 Room temperature (300 K) photoluminescence spectra for the as-prepared and the annealed ZnO thin films deposited at 100 W RF power and the blank quartz substrate, as obtained with the 488.0 nm excitation line.

substrate shows a flat background while for the as-prepared and annealed ZnO thin films, the spectra exhibit a broad emission spanning the visible and near infrared regions (500.0 nm – 900.0 nm) of the electromagnetic spectrum. The annealed ZnO film gives an intense broad emission centred at 656.0 nm (15 244 cm^{-1}) as shown in figure 4.5. The spectrum also shows some

near-infrared emission at 12 0482 cm^{-1} (830.0 nm). A similar broad emission band centred at 640.0 nm (15 625 cm^{-1}) and 690.0 nm (14 492 cm^{-1}) has been reported by Wu et al. [84] and Tam et al. [85], respectively, using the 325.0 nm excitation line and ZnO nano-rods annealed in air at 600 °C. From section 4.2.1, the XRD results of the annealed ZnO thin films show a relative improvement in crystallinity and a decrease in amorphous content (structural defects) of the samples as compared to the as-prepared films. The photoluminescence spectrum of the annealed ZnO film presented in figure 4.5 shows an increase in intensity of the emission band as compared to the as-prepared film which could be due to the improvement in the quality of the film on annealing. The observed increase in luminescence intensity on annealing (figure 4.5) can also be attributed to defects on the ZnO surface [84]. The annealing treatment may cause over compensation of oxygen on the ZnO surface due to the unfulfilled coordination (surface reconstruction). This results in an increase in defect concentration (i.e. on the surface) corresponding to the observed increase in the photoluminescence intensity [86]. This has been reported in experimental studies of sintered ZnO powders [86] where the surface luminescence intensity of the sintered powders was greater than the bulk emission intensity. The surface defects responsible for the broad emission include the zinc (Zn_i) and oxygen (O_i) interstitial defects which have been related to the green and yellow emission, respectively [84,86]. Liu et al. [86] suggested that the excess zinc responsible for the Zn_i defects on the surface reacts with ambient water vapour to form ZnO. This causes a reduction in the Zn_i defect concentration relative to the V_{Zn} and O_i defect concentrations resulting in a relative increase in the intensity of the yellow emission band [86]. On the other hand Wu et al. [84] proposed that the amount of oxygen in air is sufficient to cause O_i defects on the surface on annealing thereby enhancing the emission at 656.0 nm. The emission at 830.0 nm can then be related to a donor-acceptor transition involving the O_i (donor) and the V_{Zn} (acceptor). Variations in defect concentration may occur on the ZnO surface as a result of post-deposition annealing. Since the annealed ZnO thin film yielded a relatively high intensity spectrum, all the ZnO films were therefore annealed under the same conditions before photoluminescence measurements.

Photoluminescence measurements using the 488.0 nm excitation wavelength were then conducted on ZnO thin films deposited at 100 W, 150 W and 200 W RF powers. The resulting photoluminescence spectra are presented in figure 4.6.

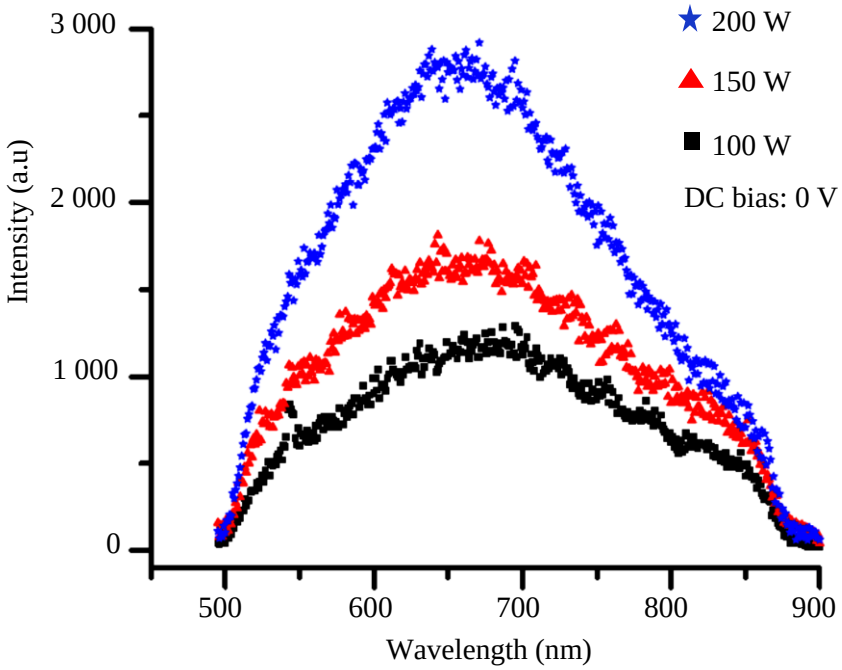

Figure 4.6 Room temperature (300 K) photoluminescence spectra of annealed ZnO thin films deposited at 100 W, 150 W and 200 W RF powers obtained with the 488.0 nm excitation wavelength.

The samples gave the same emission profile with the peak of the broad emission at 656.0 nm. However an increase in the photoluminescence intensity is observed with increasing deposition power (figure 4.6). The intensity increase can be attributed to a bulk effect as more film is deposited at high RF powers (section 3.2) resulting in a general increase in the photo-excited sample volume. The observed increase in the photoluminescence intensity with increase in deposition power is consistent with the work of Lu et al. [80]. Although the ZnO thin film deposited at 200 W yields the most intense emission, the high residual stress in the film leads to the delamination of the film from the substrate as previously stated in section 4.2.1, therefore subsequent depositions were at 150 W RF power.

Photoluminescence spectra of ZnO thin films deposited at 150 W RF power with 0 V, -25 V, -50 V and -75 V substrate bias voltages appear in figure 4.7.

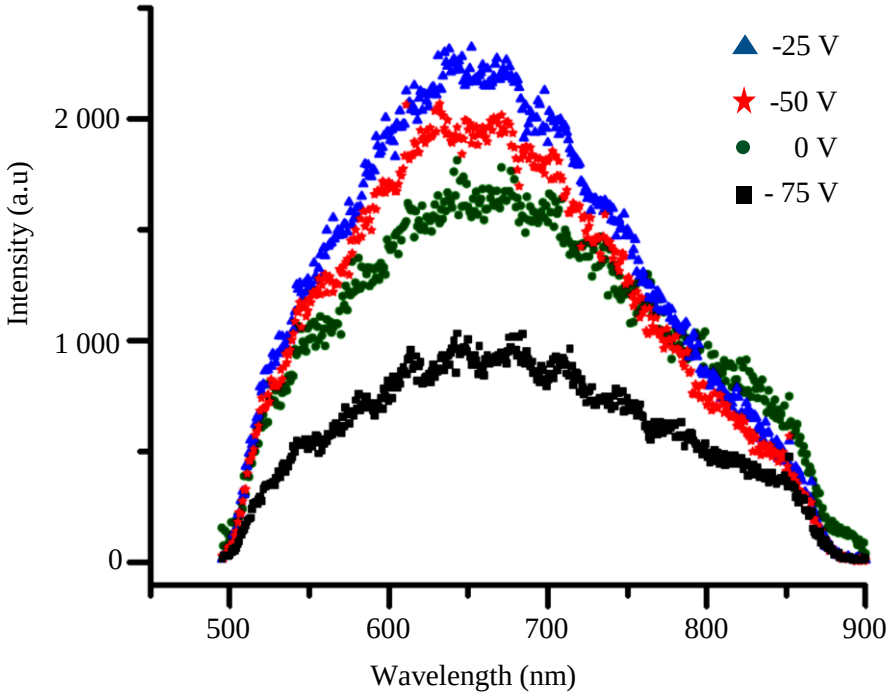

Figure 4.7 Room temperature (300 K) photoluminescence spectra for annealed ZnO thin films deposited using 150 W RF power and bias voltages of 0 V, -25 V, -50 V and -75 V, obtained with the 488.0 nm excitation wavelength.

The spectra show a broad emission in the same range as for the ZnO films deposited at 100 W, 150 W and 200 W centered at 656.0 nm. The negative bias voltage of -25 V resulted in the most intense photoluminescence emission, followed successively by that for -50 V, 0 V and -75 V. The negative bias voltage results in either the Ar^+, Zn^+ or O^+ ions being introduced into the film [87]. Among the three ions, O^+ has the least ionic mass hence more of the O^+ ions are expected to be attracted to the substrate. This will result in a relatively high concentration of the O_i defects which is consistent with the increase in emission intensity for the ZnO thin film obtained at -25 V bias (figure 4.7). However at higher negative bias voltages, the attractive force acting on the Ar^+, Zn^+ and O^+ ions is relatively high such that the ions can knock out already deposited atoms. This is shown by the reduction in photoluminescence intensity as the bias voltage is increased from -75 V to -50 V and then to -25 V.

The photoluminescence spectra of ZnO thin films deposited in an Ar_2 (13 sccm) and Ar_2/N_2 (13 sccm: 13 sccm) gas flow environment are presented in figure 4.8. The spectrum obtained from the ZnO film deposited under Ar_2 gas flow conditions shows an increase in the photoluminescence intensity by a factor

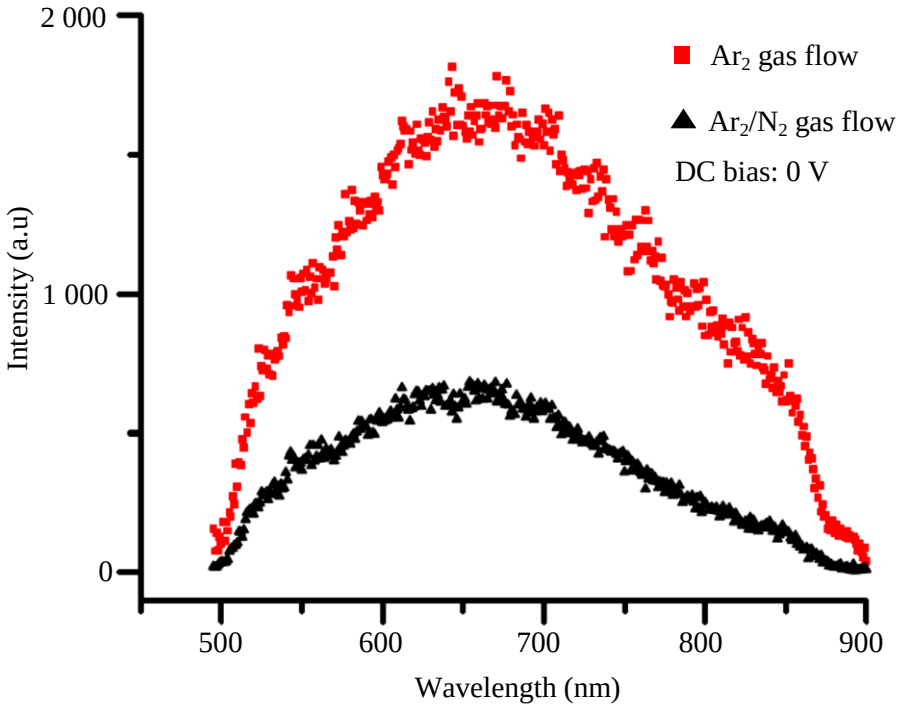

Figure 4.8 Room temperature (300 K) photoluminescence spectra for annealed ZnO thin films deposited at 150 W RF power under Ar_2 (13 sccm) and Ar_2/N_2 (13 sccm: 13 sccm) gas flow, obtained with the 488.0 nm excitation wavelength.

of three compared to the film prepared in an Ar_2/N_2 gas flow ambient (figure 4.8). The reduction in photoluminescence intensity for the ZnO film obtained under Ar_2/N_2 gas flow can be attributed to a reduction in the O_i^0 defect concentration due to the presence of N_2 gas in the growth ambient. Similar reduced photoluminescence intensity for ZnO thin films deposited under N_2 gas flow has been reported by Tu et al. [88] who attributed the decreasing photoluminescence intensity with increasing N_2 gas flow to nitrogen dopants in the ZnO film [88].

Photoluminescence spectra of the ZnO thin film deposited at 150 W under Ar_2 gas flow obtained using the 457.9 nm, 476.5 nm and 488.0 nm excitation lines at constant laser power (35 mW) are presented in figure 4.9. From the spectra, the 457.9 nm excitation line yields slightly more intense photoluminescence emission than the 488.0 nm line while the 476.5 nm yields the lowest luminescence intensity. The same luminescence band profile and peak position (15 244 cm^{-1} (656.0 nm)) is observed for all three excitation lines. This indicates

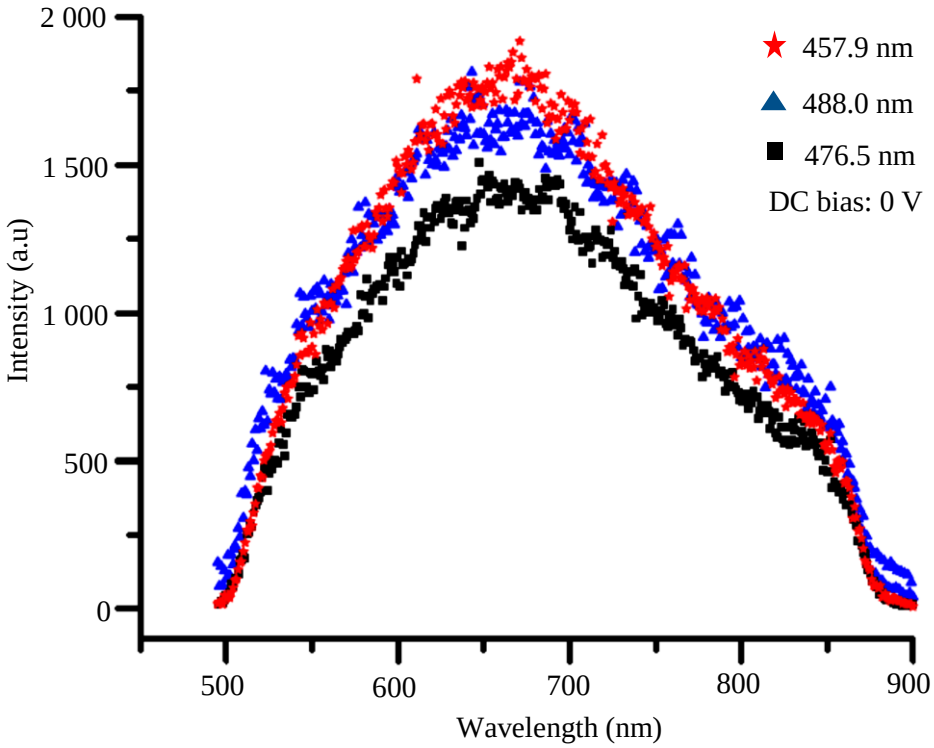

Figure 4.9 Room temperature (300 K) photoluminescence spectra for the annealed ZnO thin film deposited at 150 W RF power under Ar_2 (13 sccm) gas flow, obtained with the 457.9 nm, 476.5 nm and 488.0 nm excitation lines.

that the 457.9 nm and 476.5 nm excitation lines did not result in the population of different defect transition levels.

To determine the defect states and transitions contributing to the broad emission in the ZnO thin films and thereby identify the corresponding radiative defect level transitions, a deconvolution of the photoluminescence spectrum for the film deposited at 150 W with -25 V bias voltage was carried out as shown in figure 4.10. Gaussian curves where fitted such that each peak corresponds to a transition between a donor defect level and the VB or an acceptor defect level with guidance from the theoretical defect levels discussed in section 2.3. There is no particular relation between the individual defect level transitions. As such, each fitted curve corresponding to a transition between two defect levels has an independent linewidth determined such that the resulting overall fitted curve is superimposed on or is as close as possible to the experimental data as shown in figure 4.10. The energy separations between transitions for the different defect levels are therefore independent of each other. From the deconvolution, five

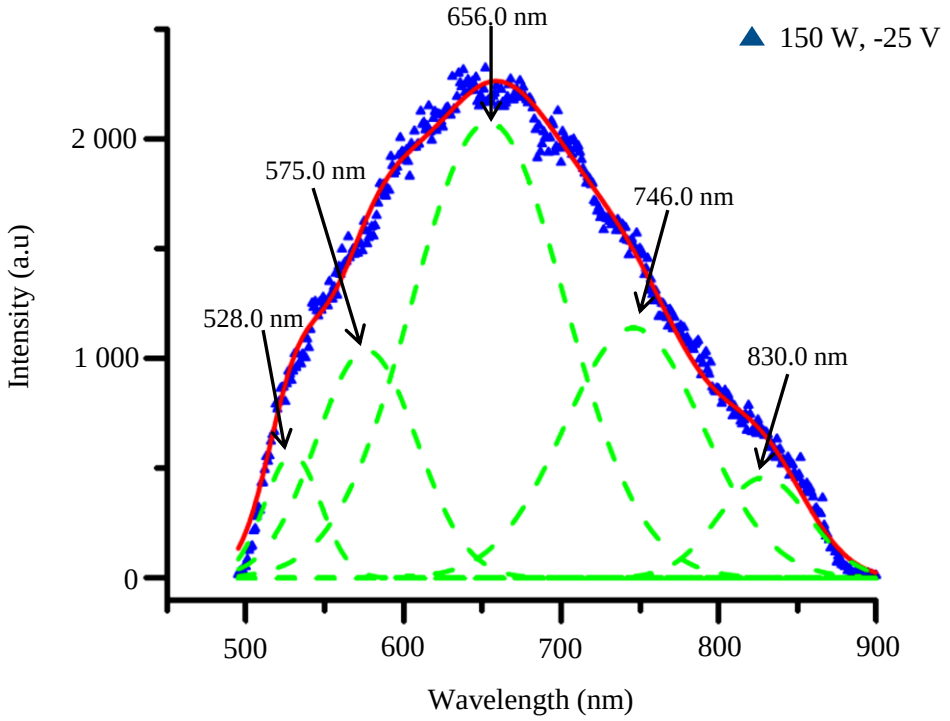

Figure 4.10 Gaussian curve fittings on the room temperature (300 K) photoluminescence spectrum of the annealed ZnO thin film deposited at 150 W RF power with -25 V bias voltage obtained using the 488.0 nm excitation wavelength.

Gaussian curves were fitted to the spectrum with peak centres at 528.0 nm (18 940 cm^{-1}), 575.0 nm (17 401 cm^{-1}), 656.0 nm (15 244 cm^{-1}), 746.0 nm (13 405 cm^{-1}) and 830.0 nm (12 048 cm^{-1}). The curve fittings yield green, orange, red and near infrared emission peaks and can be related to transitions from the defect levels previously discussed in section 2.3 (figure 2.5).

Using the Gaussian curve fittings with reference to the defect levels discussed in section 2.3 (figure 2.5), a schematic illustration of the radiative transitions was deduced as shown in figure 4.11. The V_{Zn}^{2-} defect level at 22 221 cm^{-1} [29] can be populated with the 457.9 nm (21 839 cm^{-1}) excitation line with absorption of one or two phonons as shown in figure 4.11. Population of the Zn_i^{+} defect level at 21 094 cm^{-1} [29] could be realised with either 476.5 nm (20 986 cm^{-1}) or 488.0 nm (20 492 cm^{-1}) excitation (figure 4.11). Some of the excited electrons then undergo non-radiative relaxation from the V_{Zn}^{2-} and Zn_i^{+} defect levels to the V_OZn_i defect complexes at 19 081 cm^{-1} and 17 471 cm^{-1} before populating the O_i^{0} and V_O defect levels at 17 401 cm^{-1} and 13 405 cm^{-1}, respectively, as shown in

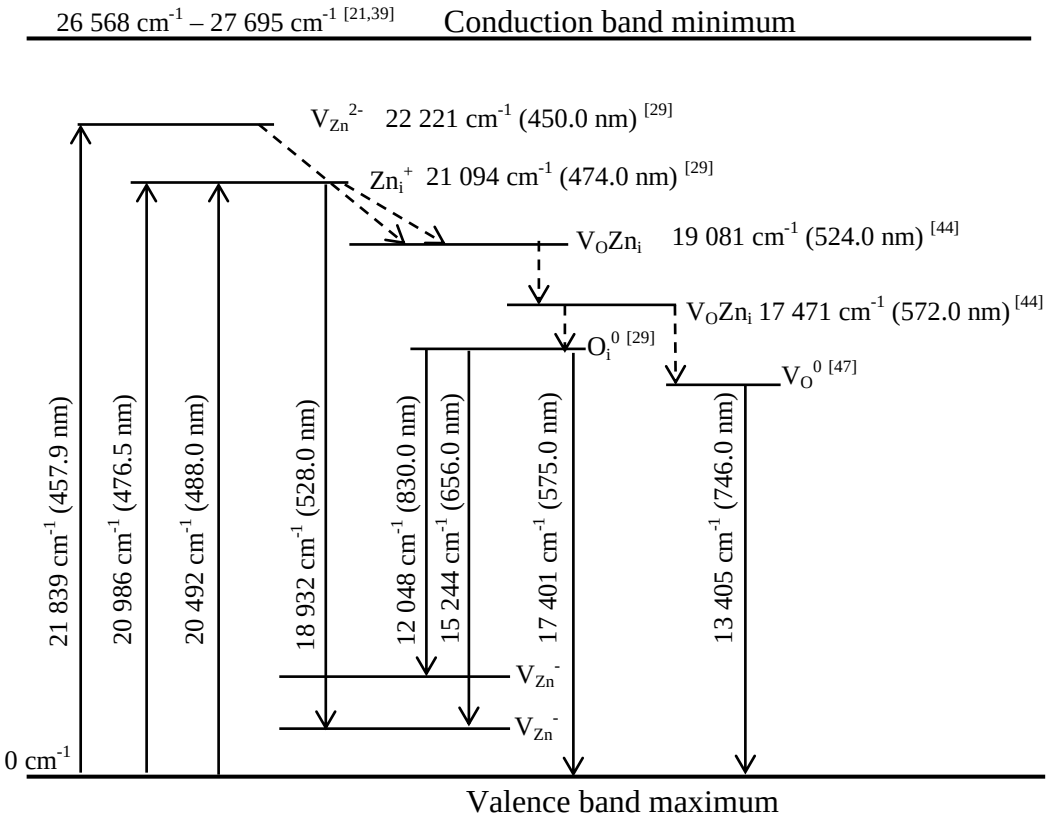

Figure 4.11 The transition energy levels associated with the ZnO intrinsic point defects in wavenumbers (cm^{-1}). The solid lines show radiative transitions while the dashed lines indicate non-radiative transitions. Superscript 0 denotes a neutral charge state while -/+ denote a singly charged negative/positive state, respectively, and 2- is a doubly charged negative state. (8 051 cm^{-1} = 1 eV)

figure 4.11. The V_OZn_i complexes provide an important intermediate step because direct non-radiative decay between single point defects is not permitted [46] as was discussed in section 2.3. On populating the different donor defect levels, the electrons then undergo radiative transitions to either the VB or the acceptor V_{Zn}^- defect level (figure 4.11). With the defect levels populated this way, the green emission at 528.0 nm (figure 4.10) can be attributed to the $Zn_i^+ \rightarrow V_{Zn}^-$ radiative transition at 18 932 cm^{-1} (528.0 nm) (figure 4.11). The $Zn_i^+ \rightarrow V_{Zn}^-$ transition is in agreement with the theoretical calculations reported by Janotti et al. [41] where the V_{Zn}^- is an acceptor defect level. This is further supported by the experimental results presented by Stavale et al. [47]. Although transitions involving the V_O^+ defect at 17 654 cm^{-1} above the VB have been reported in experimental studies to contribute towards the green emission [29], the V_O^+ defect occurs in low concentrations and is therefore unlikely to have a

significant contribution [41] . It is therefore expected that the $Zn_i^+ \rightarrow V_{Zn}^-$ transition is predominantly responsible for the green emission at 528.0 nm (figure 4.10).

The yellow emission centred at 575.0 nm (17 401 cm^{-1}) (figure 4.10) can be related to a transition from an O_i^0 defect level at 17 401 cm^{-1} to the VB as shown in figure 4.11. Emission due to the O_i^0 defect level could also arise from the $O_i^0 \rightarrow V_{Zn}^-$ transitions which correspond to the 656.0 nm (15 244 cm^{-1}) and 830.0 nm (12 048 cm^{-1}) curve fittings. A transition from the O_i^0 level to the lower V_{Zn}^- level yields the broad emission centred at 656.0 nm while the near infrared emission at 830.0 nm is attributable to an electronic transition from the O_i^0 to the higher V_{Zn}^- level (figure 4.11). Radiative emission is also observed at 746.0 nm (13 405 cm^{-1}) (figure 4.10) which corresponds to the $V_O^0 \rightarrow$ VB transition as illustrated in figure 4.11. This emission band has been reported in the experimental work conducted by Stavale et al. [47] where the luminescence intensity at 730.0 nm increased under high zinc growth conditions due to an increase in the V_O^0 defect concentration. Having identified the defect level transitions responsible for the broad emission, a summary of the XRD characterisation and photoluminescence studies of the ZnO thin films is presented in the following section.

4.3 Conclusion

The XRD characterisation results generally show a hexagonal wurtzite structure in the ZnO thin films deposited under various growth conditions. The annealing treatment resulted in improved XRD peak intensities indicating enhanced crystallinity. Variations in the substrate bias voltage resulted in a change in the growth orientation of the film. This was observed for the ZnO films obtained at -25 V and -50 V bias voltages which yielded XRD patterns showing a (0 0 2) and (1 0 3) preferential growth. The XRD patterns for the -75 V sample showed a (1 1 2) preferred growth orientation while the ZnO film deposited at 0 V bias voltage yielded XRD patterns with a (1 0 0), (1 0 1) and (1 1 2) preferential growth. As the deposition power increased from 100 W to 150 W a slight change in the XRD peak intensities was observed. With further increase from 150 W to 200 W, the resulting sample yielded more XRD peaks of relatively low intensity

in comparison to the 100 W and 150 W samples. The ZnO film obtained in an Ar_2/N_2 ambient resulted in a slight increase in intensity for the diffraction peaks associated with the (1 0 2) and (1 0 3) planes compared to the sample prepared in an Ar_2 ambient.

For the photoluminescence results, there was no significant change in the broad emission peak centre (656.0 nm) as the ZnO thin film growth conditions were varied. The only changes observed were in the photoluminescence intensity where annealing in air yielded higher luminescence intensity. From the Gaussian fittings, the emission at 528.0 nm (18 932 cm^{-1}), 575.0 nm (17 401 cm^{-1}), 656.0 nm (15 244 cm^{-1}), and at 746.0 nm (13 405 cm^{-1}) correspond to the $Zn_i^+ \rightarrow V_{Zn}^-$, $O_i^0 \rightarrow$ VB, $O_i^0 \rightarrow V_{Zn}^-$ and $V_O^0 \rightarrow$ VB transitions, respectively. The emission at 830.0 nm (12 048 cm^{-1}) is attributable to a transition for the O_i^0 defect level to the second V_{Zn}^- defect level. There was no significant change in the emission profile with change in excitation wavelength indicating that the same defect levels were being populated with each of the three excitation lines. In general the observed emission can be attributed to electronic transitions involving zinc and oxygen interstitial defects.

Chapter 5

Laser excitation studies and crystal-field analysis of ZnO:Eu^{3+} and ZnO:Tb^{3+} powders

5.1 Introduction

Optical studies in chapter 4 and in the literature [2,16,17], have shown ZnO to yield a broad emission in the visible region of the electromagnetic spectrum. The broad emission has been attributed to deep level transitions within the bandgap due to intrinsic ZnO defects. These defects predominantly consist of zinc interstitials [29], oxygen interstitials, zinc vacancies and oxygen vacancies [16,29]. To enhance the visible emission, studies on rare earth (RE^{3+}) doped ZnO continue to be pursued with successful incorporation of RE^{3+} ions such as trivalent terbium (Tb^{3+}-0.92 Å) [2,89] and europium (Eu^{3+}-0.95 Å) ions [9]. It is suggested that the RE^{3+} ion resides at either a Zn^{2+} (0.74 Å) lattice site or an interstitial position [9,57,89] with a neighboring zinc vacancy for charge compensation [89] as discussed in section 2.4. Intense green and red emission bands have been observed for ZnO:Tb^{3+} [2,89] and ZnO:Eu^{3+} [9], respectively, with ultra-violet excitation. RE^{3+} doping therefore significantly enhances visible luminescence in ZnO and could be useful for solid-state laser development and for optoelectronic device applications. The relatively intense peaks are attributed to the RE^{3+} intra-4f radiative transitions [90]. The narrow linewidths are a result of the free ion like behaviour of the RE^{3+} ion due to 5s and 5p shielding of the 4f orbital from the ligand environment (section 2.4; figure 2.6) [2,49].

Among the many different techniques of preparing RE^{3+} doped semiconductors [81,17], semiconductor powder synthesis continues to be pursued [2,9]. Powder synthesis provides a simple and low-cost procedure for the incorporation of RE^{3+} dopants into semiconductors [15]. In particular, the chemical bath deposition method used for this study is a relatively low temperature (80 °C) technique.

In the literature, studies of ZnO:Tb^{3+} and ZnO:Eu^{3+} have focused on ultra-violet excitation and visible emission for white light production [2,9]. In this work, visible-region excitation and visible-region emission studies of ZnO:Tb^{3+} and ZnO:Eu^{3+} are presented. Preliminary photoluminescence measurements were conducted on undoped as well as 0.2, 0.5 and 1.0 mol% Eu^{3+} doped ZnO at room temperature (300 K) using the 488.0 nm excitation line. From the spectra, it was observed that the intensity of the Eu^{3+} ion emission bands increases with increase in dopant concentration. Based on these initial results, blue-laser excitation studies of ZnO powders separately doped with 1.0 mol % Eu^{3+} and 1.0 mol % Tb^{3+} were carried out in detail. Therefore only results of 1.0 mol% RE^{3+} doped ZnO are presented in this work. Although there is no clear energy exchange process from the ZnO host to the RE^{3+} ions some energy transfer mechanism will be suggested in this study.

The undoped and RE-doped ZnO powders used for photoluminescence studies were characterized using X-ray diffraction (XRD) and scanning electron microscopy (SEM). Energy dispersion spectroscopy (EDS) was used to determine the qualitative elemental composition of the samples.

5.2 Results and discussion

5.2.1 XRD studies

The grazing incidence XRD patterns of both as-prepared and annealed samples of pristine ZnO and 1.0 mol% Eu^{3+}, 1.0 mol% Tb^{3+} (A sample) and 1.0 mol% Tb^{3+} (B sample) doped ZnO powders are presented in figure 5.1. The XRD patterns of the as-prepared undoped ZnO, the ZnO:Tb^{3+} (A) and the ZnO:Tb^{3+} (B) (figure 5.1 (a) ii, (b) ii and (c) ii) show zinc acetate related peaks (marked with an asterisk (*)) in addition to the ZnO peaks. The zinc acetate peaks correspond to 2θ values of 20.2°, 25.0°, 27.5°, 39.5°, 51.9° and 59.8° which are consistent with the 2θ angles reported in the literature [91]. These peaks may be due to unreacted zinc acetate [62] as it is a precursor in the synthesis of the ZnO powders as previously discussed in section 3.3. On the other hand, the as-prepared ZnO:Eu^{3+} XRD pattern as shown in figure 5.1 (d) ii did not exhibit any peaks attributed to the precursor. It could not be established why the as-prepared ZnO:Eu^{3+} sample

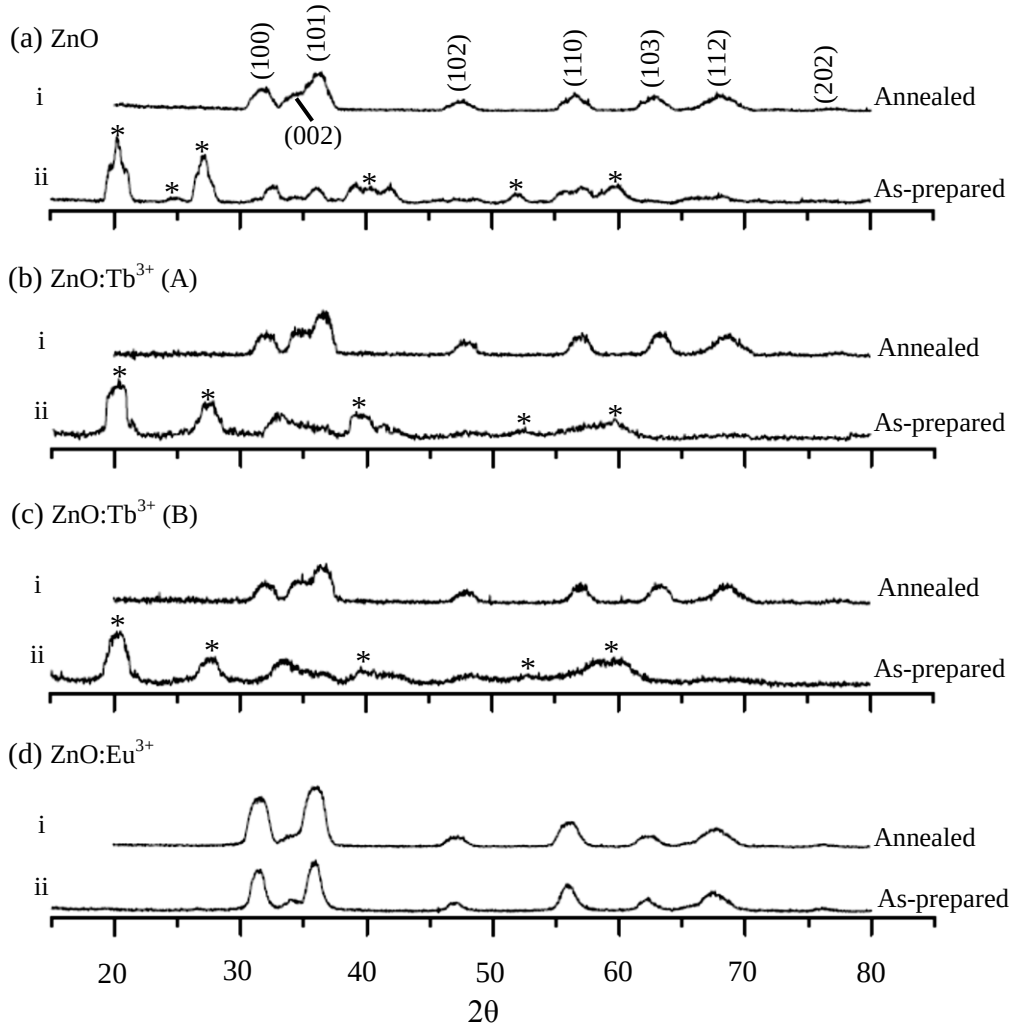

Figure 5.1 Grazing incidence XRD patterns for annealed and as-prepared (a) pristine ZnO powder, (b) 1.0 mol% Tb^{3+} (A sample), (c) 1.0 mol% Tb^{3+} (B sample) and (d) 1.0 mol% Eu^{3+} doped ZnO powders. The asterisk (*) identifies the zinc acetate peaks while the ZnO diffraction planes are as labelled in (a).

did not give any zinc acetate XRD peaks. The annealing treatment (700 °C in air for 2 hours) was carried out so as to remove the precursor (zinc acetate) impurity resulting in only the ZnO XRD peaks as shown in figure 5.1 (a) i, (b) i, (c) i, and (d) i. For all the annealed samples, the XRD patterns show peaks at 31.9°, 34.3°, 36.3°, 47.4°, 56.5°, 62.8°, 68.0° and 76.8° associated with the (1 0 0), (0 0 2), (1 0 1), (1 0 2), (1 1 0), (1 0 3), (1 1 2) and (2 0 2) planes of the wurtzite ZnO phase [62,91].

The broadened linewidth (β) of the XRD peaks is a result of two factors which are microstrain (ε) and small crystallite size of the powders [92,93]. XRD

peak-broadening studies based on the Williamsom-Hall (WH) plot were conducted to determine the average crystallite size (D) and the nature of the microstrain (ε) (compressive or tensile) associated with the samples. The microstrain component of the WH equation is obtained from the differential of the Bragg equation [93]. The effect of microstrain on the broadening of the XRD peaks is contained in the linewidth component β_ε (full width at half maximum-FWHM) and can be expressed in the form of equation (5.1) [93]

$$\beta_\varepsilon = 4\varepsilon \tan\theta . \tag{5.1}$$

The linewidth component β_D (FWHM) due to the crystallite size (D) can be determined from the Scherrer formula by arranging the terms as shown in equation in equation (5.2) where k is the Scherrer constant [68].

$$\beta_D = \frac{k\lambda}{D\cos\theta} \tag{5.2}$$

The overall linewidth, β (FWHM) is as shown in equation (5.3).

$$\beta = \beta_D + \beta_\varepsilon = \frac{k\lambda}{D\cos\theta} + \frac{4\varepsilon\sin\theta}{\cos\theta} \tag{5.3}$$

The Scherrer constant k varies with crystallite shape. However the values are always such that $0.97 < k \leq 1$ hence k is usually taken to be equal to one [68], leading to the equation (5.4).

$$\frac{\beta\cos\theta}{\lambda} = \frac{1}{D} + \frac{4\varepsilon\sin\theta}{\lambda} \tag{5.4}$$

An estimate of the crystallite size is calculated using equation 5.2. The WH analysis is based on the plot of equation 5.4 where $\beta\cos\theta/\lambda$ is plotted on the y-axis and $\sin\theta/\lambda$ is plotted on the x-axis. If the crystallite size and the microstrain of the samples under study are homogeneously distributed, the resulting plot is a straight line [93]. From the linear fit of the plot, a positive slope shows tensile microstrain while a negative slope illustrates compressive microstrain within the sample [93]. A linear fit with gradient equal to zero indicates that the sample is free of microstrain. The average crystallite size can be determined from the reciprocal of the y-intercept [93].

The WH plots for the annealed samples of pristine ZnO, Eu^{3+} and Tb^{3+} doped ZnO powders are presented in figure 5.2. The plots exhibit fairly linear

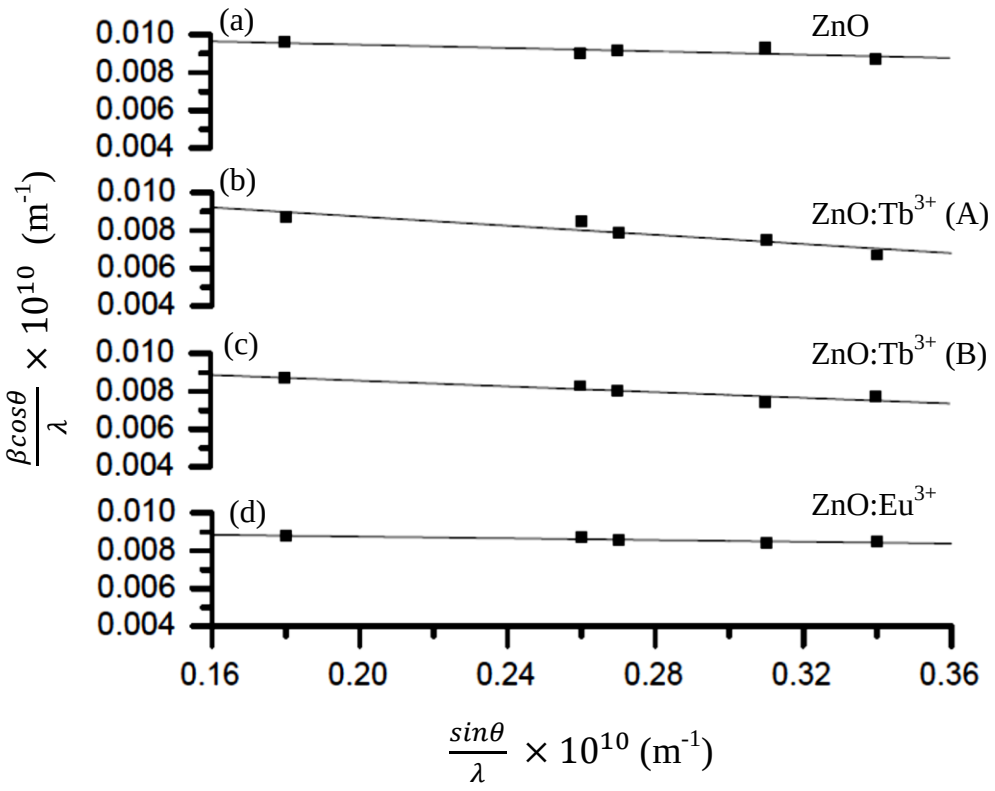

Figure 5.2 The Williamson-Hall plots for (a) ZnO, (b) 1.0 mol% ZnO:Tb^{3+} (A), (c) 1.0 mol% ZnO:Tb^{3+} (B) and (d) 1.0 mol% ZnO:Eu^{3+} powders obtained from XRD patterns of the annealed samples.

distribution of the data points indicating a homogeneous distribution of the crystallite size and microstrain within the sample powders. The negative gradient shows the existence of slight compressive microstrain for all the samples with the ZnO:Tb^{3+} (A) powders having the greatest micro-compression. The average crystallite size is 10 ± 1 nm for all the samples (table 5.1). The crystallite sizes determined in this work are smaller compared to those of Koao et al. [62] where crystallite sizes in the 45.0 nm region were obtained for ZnO powders prepared using chemical bath deposition [62]. Large crystallite sizes indicate improved crystallinity within the sample powders and these are usually associated with narrow linewidths and relatively intense XRD peaks [68]. The sample powders in this work yield relatively broad linewidths which are consistent with the small crystallite sizes and low intensity XRD peaks identified with nano-crystalline grains in an amorphous matrix [68]. The lattice parameters *a* and *c* presented in

table 5.1 were calculated by applying equation (5.5) [81] to peaks of the (1 0 0) and the (1 0 2) planes in the annealed XRD patterns.

$$\left(d_{hkl}\right)^2 = \left(\frac{\lambda}{\sin\theta}\right)^2 = \frac{3a^2c^2}{4c^2\left(h^2+k^2+hk\right)+3a^2l^2} \qquad (5.5)$$

In the literature [12], the experimentally and theoretically determined lattice constants range from 0.319 nm to 0.325 nm and from 0.515 nm to 0.521 nm for the *a* and the *c* lattice parameters, respectively. The lattice constants determined in this study for the ZnO powders are therefore comparably the same to those reported in the literature [12] (table 5.1). The microstrain (ε) within the ZnO powders is of relatively small magnitude (table 5.1) and hence did not have any significant effect on the ZnO lattice constants. The *c/a* ratio does not change significantly with 1 mol% RE^{3+}, hence depending on the the RE^{3+} ionic radius, the RE^{3+} could be on the grain boundaries or surface of the ZnO host.

Table 5.1 Lattice constants, *c/a*, crystallite sizes and microstrain for undoped, Tb^{3+} and Eu^{3+} doped ZnO powders.

Sample	Lattice constants (±0.006 nm)		$\frac{c}{a}$	Crystallite size (±1 nm) D (nm)		Microstrain (±0.0002)
	a (nm)	*c* (nm)	(±0.04)	(S)	(WH)	(ε)
ZnO	0.326	0.519	1.59	9	10	-0.0011
ZnO:Tb^{3+} (A)	0.322	0.519	1.61	10	9	-0.0022
ZnO:Tb^{3+} (B)	0.322	0.517	1.61	10	10	-0.0019
ZnO:Eu^{3+}	0.327	0.523	1.60	9	11	-0.0008

(S) – Scherrer

(WH) – Williamson-Hall

Generally, XRD patterns of the annealed samples show a hexagonal wurtzite ZnO structure for the undoped and RE^{3+} doped powders. The WH plots show compressive microstrain for all the annealed samples. The crystallite sizes determined from the WH plots were consistent with those calculated using the Scherrer formula.

5.2.2 EDS and SEM characterisation

To confirm the composition of the ZnO powder samples, EDS measurements were carried out on the as-prepared and the annealed samples. Firstly an EDS spectrum of an empty sample holder (gold-palladium coated stub with carbon tape) was recorded as a reference (figure 5.3). The reference spectrum shows peaks for carbon from the carbon tape, aluminium from the mounting stub and a relatively low concentration of oxygen (figure 5.3). The peak observed at 0 keV is the reference from the detector. As expected, the EDS spectrum for the undoped ZnO (figure 5.4 (a)) exhibits zinc and oxygen peaks only. On the other hand, the EDS spectrum for the ZnO:Tb^{3+} (A) sample (figure 5.4 (b)) did not show any terbium peaks although zinc and oxygen peaks were observed. This indicates that the incorporation of the terbium into or on the surface of the ZnO

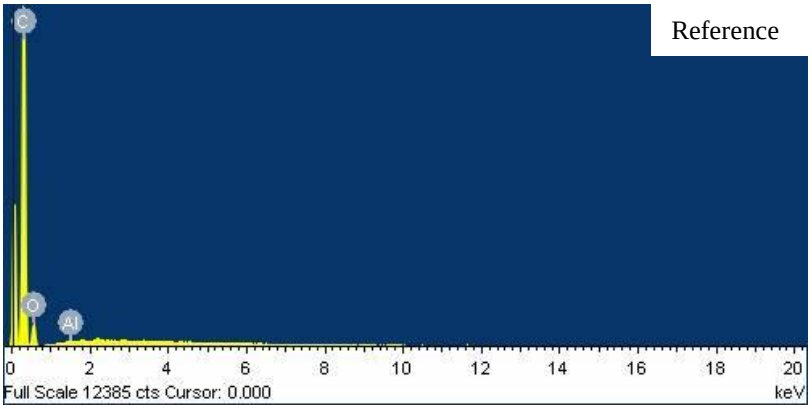

Figure 5.3 Reference EDS spectrum for the sample holder with carbon tape.

host was not successful. The EDS spectra for the ZnO:Tb^{3+} (B) and ZnO:Eu^{3+} samples confirmed the presence of terbium and europium, respectively as shown in figure 5.4 (c) and (d). The reference EDS spectrum exhibited high concentrations of carbon as compared to the ZnO, ZnO:Tb^{3+} (A), ZnO:Tb^{3+} (B) and ZnO:Eu^{3+} EDS spectra. This is because the sample powders cover the carbon tape thereby significantly reducing the area of the carbon tape exposed to the electron beam. A general increase in oxygen intensity is observed in the EDS spectra for all the samples and can be related to the oxygen in the ZnO host. There was no significant change in the elemental composition after annealing the powders as shown by the EDS spectra presented in figure 5.5 (a), (b), (c) and (d). The XRD patterns in figure 5.1 for the ZnO, ZnO:Tb^{3+} (A) and ZnO:Tb^{3+} (B)

samples show the presence of zinc acetate (Zn $(CH_3COO)_2 \cdot 2H_2O$) which mainly constitutes of zinc, oxygen and carbon. These are elements found in the ZnO sample powders and the carbon tape. Therefore a distinction between the zinc acetate and ZnO could not be made using EDS characterisation.

The SEM images of the as-prepared and annealed ZnO powders are presented in figure 5.6. Generally, the annealing process did not change the morphology of the powders. The SEM image of the undoped ZnO shows a rhombohedral shape (figures 5.6 (a) i and ii) with an average size of 12 μm as measured diagonally across the particles. The SEM image of the ZnO:Tb^{3+} (A) sample also exhibits a rhombohedral shape as for the undoped ZnO with a mean size of 12 μm and in addition traces of star-like rods are also present (figure 5.6 (b) i and ii). SEM images of the ZnO:Tb^{3+} (B) sample present a flower like morphology (figure 5.6 (c) i and ii) with dimensions of 1.9 μm as measured across the particle. The difference in the morphology between the ZnO:Tb^{3+} (A) and ZnO:Tb^{3+} (B) samples is attributed to the change in the precipitate idle time before filtration (section 3.3; table 3.2); the ZnO:Tb^{3+} (A) sample was left as a precipitate for 8 hours before filtering while the ZnO:Tb^{3+} (B) sample was filtered immediately after the precipitate was formed. SEM images of the ZnO:Eu^{3+} sample (figure 5.6 (d) i and ii) show star-like rods with an average length and width of 7.1 μm and 1.8 μm, respectively. Similar star-like rods are present however in small quantities in the ZnO:Tb^{3+} (A) sample (figure 5.6 (b)). It appears that introduction of the rare-earth has the effect of changing the shape of the particles [91] in addition to the reduction in the average size.

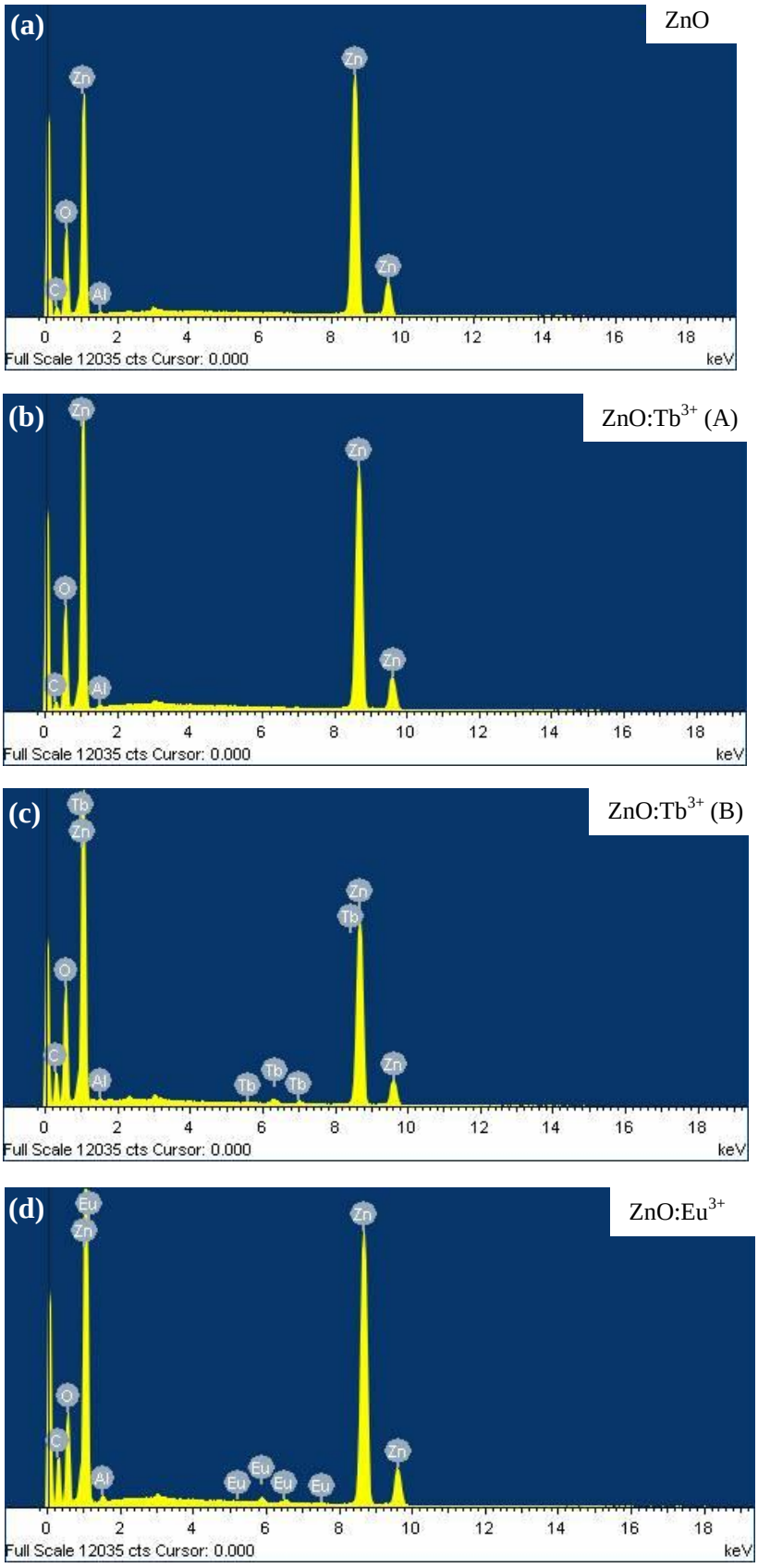

Figure 5.4 EDS spectra showing the elemental composition of as-prepared (a) ZnO, (b) 1.0 mol% ZnO:Tb^{3+} (A), (c) 1.0 mol% ZnO:Tb^{3+} (B) and (d) 1.0 mol% ZnO:Eu^{3+} powders.

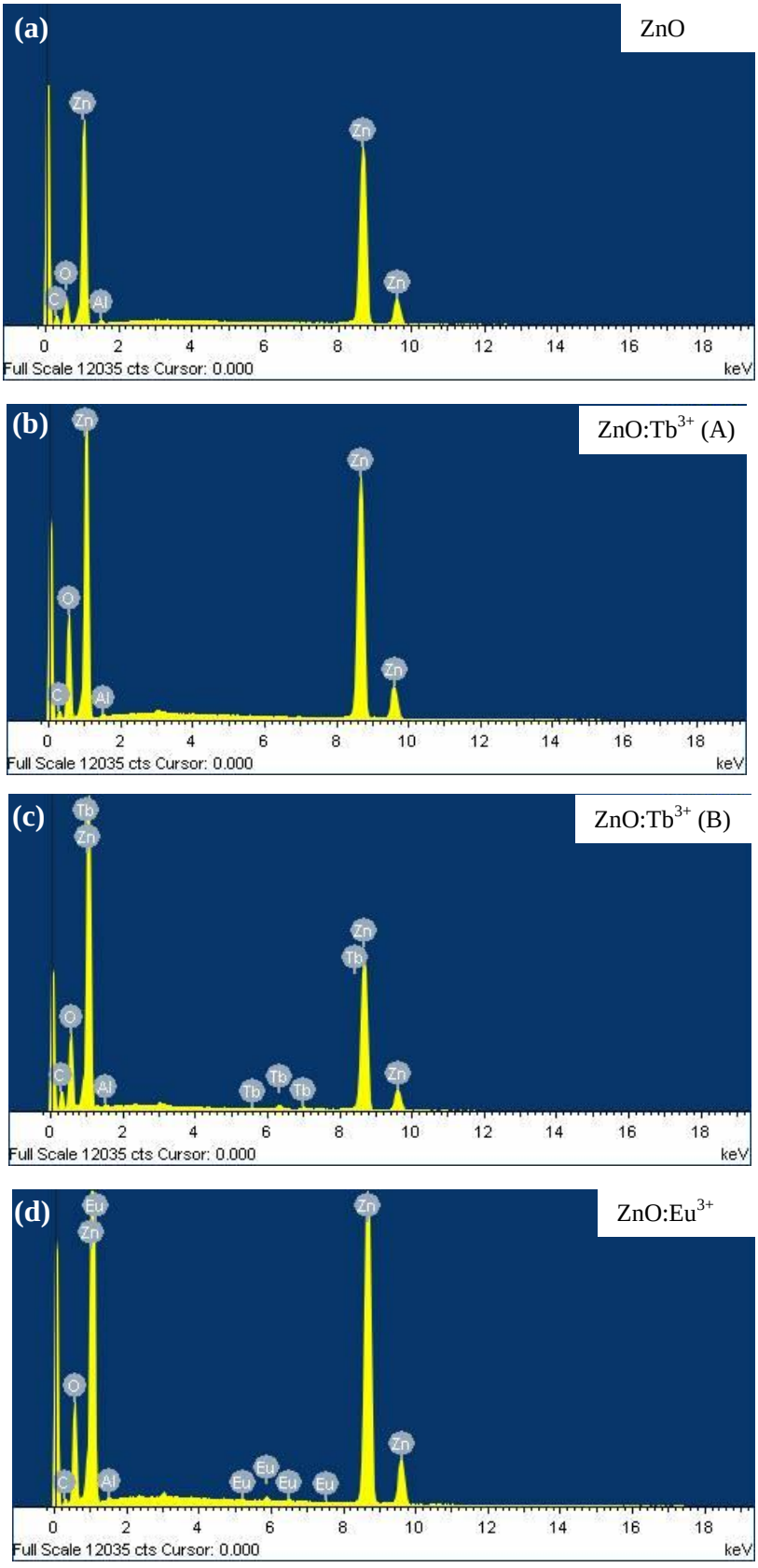

Figure 5.5 EDS spectra showing the elemental composition of annealed (a) ZnO, (b) 1.0 mol% ZnO:Tb^{3+} (A), (c) 1.0 mol% ZnO:Tb^{3+} (B) and (d) 1.0 mol% ZnO:Eu^{3+} powders.

(a) i ZnO: as-prepared

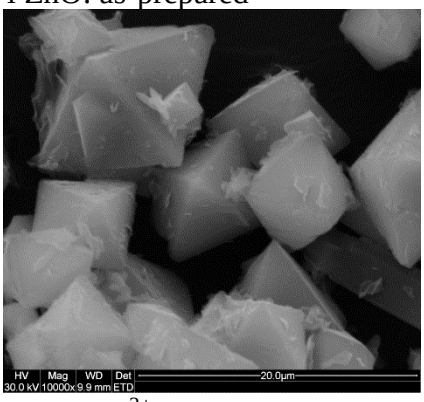

ii ZnO: annealed

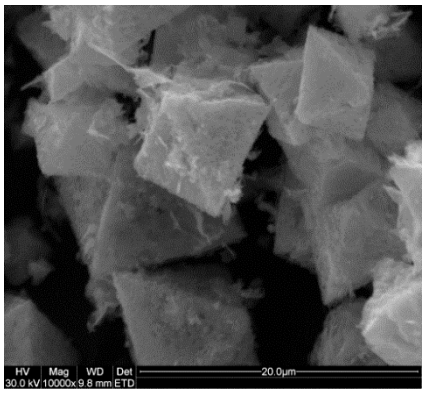

(b) i ZnO:Tb^{3+}(A): as-prepared

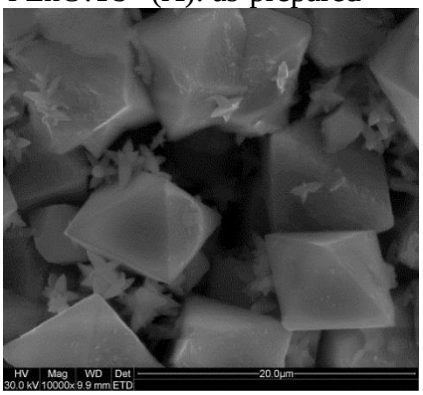

ii ZnO:Tb^{3+}(A): annealed

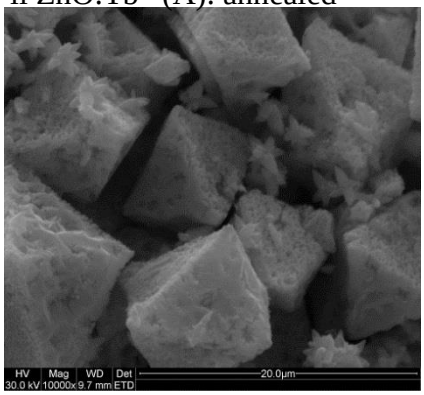

(c) i ZnO:Tb^{3+}(B): as-prepared

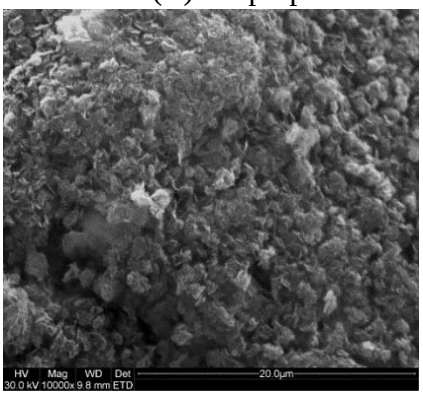

ii ZnO:Tb^{3+}(B): annealed

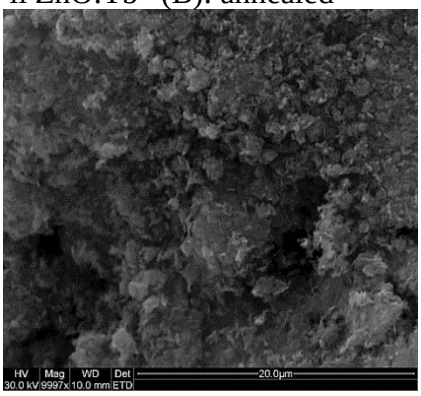

(d) i ZnO:Eu^{3+}: as-prepared

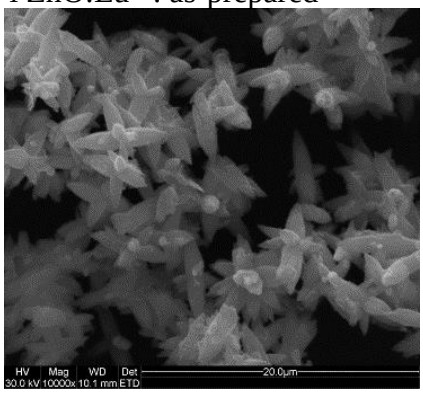

ii ZnO:Eu^{3+}: annealed

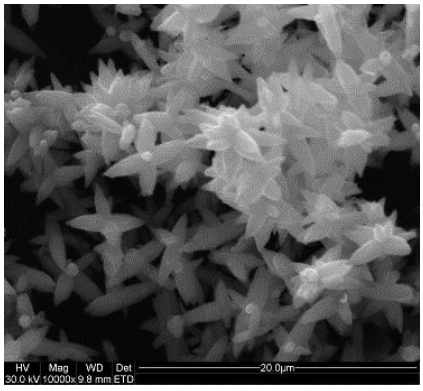

Figure 5.6 SEM images of (a) ZnO, (b) 1.0 mol% ZnO:Tb^{3+} (A), (c) 1.0 mol% ZnO:Tb^{3+} (B) and (d) 1.0 mol% ZnO:Eu^{3+} powders. (i) as-prepared and (ii) annealed samples.

From the characterisation results, all the annealed sample powders yield ZnO XRD peaks related to the wurtzite structure without any additional phases. For the EDS and SEM characterisation, no significant change in the elemental composition and morphology, respectively, was observed after annealing the samples.

5.2.3 Laser-excited photoluminescence

5.2.3.1 ZnO:Eu^{3+} photoluminescence

The spectra for the 1.0 mol% Eu^{3+} doped ZnO and the undoped ZnO powders obtained with the 476.5 nm and the 488.0 nm excitation lines at 300 K are shown in figure 5.7. The spectrum obtained with 457.9 nm excitation had a very poor signal-to-noise ratio and is omitted from this analysis. Photoluminescence measurements were also carried out on the ZnO:Eu^{3+} pellet at 10 K using the

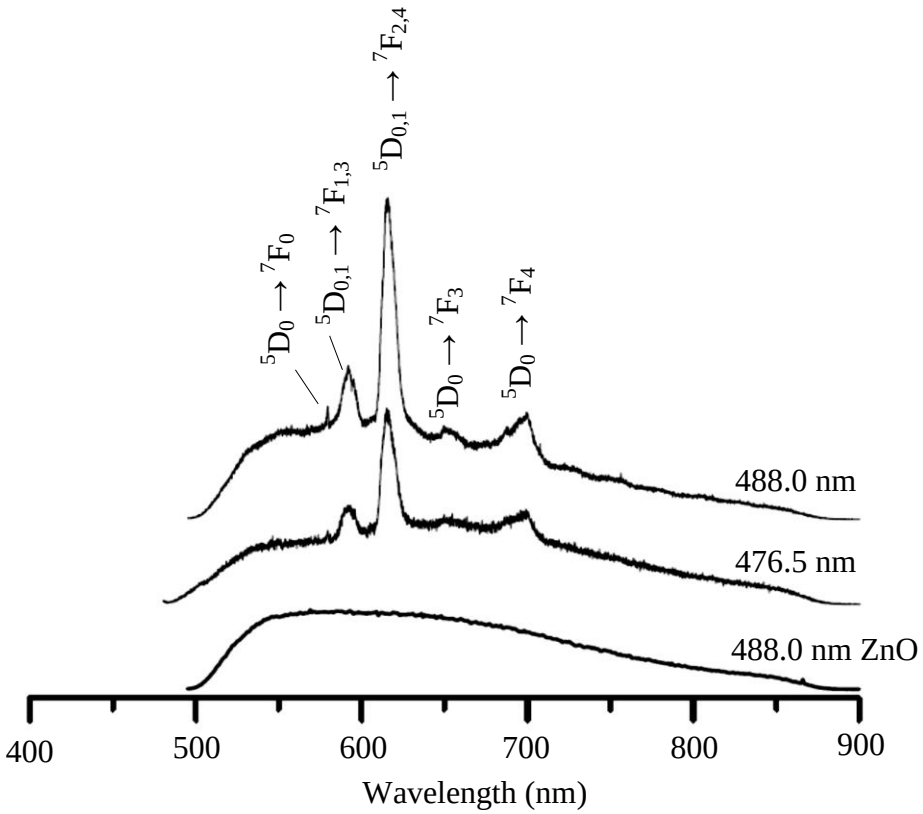

Figure 5.7 Room temperature (300 K) photoluminescence spectra of 1 mol% Eu^{3+} doped ZnO and undoped ZnO samples obtained using the 476.5 nm and 488.0 nm excitation lines.

488.0 nm excitation line since it yields the most intense Eu^{3+} emission bands at 300 K. However, the sample did not give any significant Eu^{3+} emission and no further low temperature measurements were attempted. As such only the room temperature photoluminescence spectra are presented in this section. For the annealed ZnO:Eu^{3+} sample, no significant change in the Eu^{3+} ion emission was observed as compared to the pristine (as-prepared) sample. This is consistent with the SEM and EDS characterisation results which show no changes in morphology and elemental composition, respectively, after the annealing treatment (figures 5.4, 5.5, and 5.6). The undoped ZnO spectrum shows a broad emission band with almost uniform intensity from 550 nm to about 700 nm, followed by a gradual decrease in intensity thereafter. The spectrum of the undoped ZnO obtained with 488.0 nm excitation follows the profile of the broad background emission of the ZnO:Eu^{3+} sample obtained with both the 488.0 nm and 476.5 nm excitation lines (figure 5.7). This broad background emission is therefore attributed to the intrinsic defects in the ZnO host lattice [9] which have been discussed in sections 2.3 and 4.2.2. The green emission (510.0 nm-570.0 nm) is associated with the $Zn^{+}_{i} \rightarrow V^{-}_{Zn}$ and the $V_O^{+} \rightarrow VB$ transitions [29] while the yellow-orange emission in the 570.0 nm-610.0 nm region is related to the $O_i \rightarrow VB$ and $V_O^{+} \rightarrow V^{-}_{Zn}$ transitions [29]. The red emission observed in the 610.0 nm-680.0 nm regime is attributed to $V_O^{+} \rightarrow V_{Zn}$ and $O_i \rightarrow V_{Zn}$ transitions [29] while the $V_O \rightarrow VB$ [47] transition is related to the near infrared emission (680.0 nm-750.0 nm). It is these defect related transitions (section 4.2.2; figure 4.11) that lead to indirect excitation of the Eu^{3+} ion in the ZnO host by means of energy transfer mechanisms [18,90] which will be discussed in section 5.2.3.3.

With either 488.0 nm or 476.5 nm excitation, the ZnO:Eu^{3+} sample yields Eu^{3+} emission bands superimposed on the broad background emission. The intensity of the Eu^{3+} emission bands is observed to be higher with the 488.0 nm excitation line. The spectra show the same relatively intense Eu^{3+} emission bands centred at 579.0 nm, 592.0 nm, 615.0 nm, 650.0 nm and 699.0 nm which are due to electronic transitions from the $^5D_0$ multiplet to the ^7F_J (J = 0, 1, 2, 3, 4) multiplets (figure 5.7). In addition, transitions from the $^5D_1$ multiplet to the $^7F_3$ and $^7F_4$

multiplets overlap with the $^5D_0 \rightarrow {}^7F_1$ and $^5D_0 \rightarrow {}^7F_2$ transitions, respectively. The most intense emission band centred at 615.0 nm corresponds to the overlapping $^5D_0 \rightarrow {}^7F_2$ and $^5D_1 \rightarrow {}^7F_4$ transitions. These emission bands have been reported in the literature from ultra-violet excitation studies but with no further analysis [9,94]. Analysis of the Eu^{3+} emission bands obtained at room temperature (300 K) with the 488.0 nm excitation line and the resulting crystal-field energy levels are presented in the next section.

5.2.3.2 Eu^{3+} crystal-field energy levels

Knowledge of the RE^{3+} ion site symmetry in the host matrix is important for determining the RE^{3+} ion energy levels resulting from crystal-field effects [49]. It is from the site symmetry and the selection rules that RE^{3+} ion transitions can be assigned to specific originating and terminating crystal-field energy levels, thereby determining the energy level scheme of the RE^{3+} ion in a particular host lattice [49]. The C_{3v} configuration is most commonly associated with RE^{3+} ions in the ZnO lattice [51,52,57] and is adopted for the analysis presented here. The number of crystal-field energy levels expected for the C_{3v}-symmetry site and the applicable selection rules are presented in tables 2.1 and 2.2 (section 2.6), respectively.

To deduce the crystal-field energy levels from the observed photoluminescence spectra, Gaussian peak profiles were fitted to each of the Eu^{3+} emission bands in figure 5.7. The Gaussian curve fittings were carried out using the Origin version 6.1 program with a good fit corresponding to a reduced chi-square value close to 1. The curve fittings were carried out starting with the $^5D_0$ (A) $\rightarrow {}^7F_0$ (Z) transition band at 579.0 nm (figure 5.7); the fitted peak is as shown in figure 5.8 (a). The $^5D_0$ (emitting) and $^7F_0$ (terminating) multiplets both have J = 0 which corresponds to one crystal-field energy level each hence a single transition could be expected. This single transition is represented by the fitted Gaussian peak in the $^5D_0$ (A) $\rightarrow {}^7F_0$ (Z) transition band as shown in figure 5.8 (a). From the results, the crystal-field energy level of the $^5D_0$ multiplet was deduced to be at 17 259 cm^{-1} (figure 5.8 (c)) since the $^7F_0$ multiplet is the ground state (0 cm^{-1}) of Eu^{3+}.

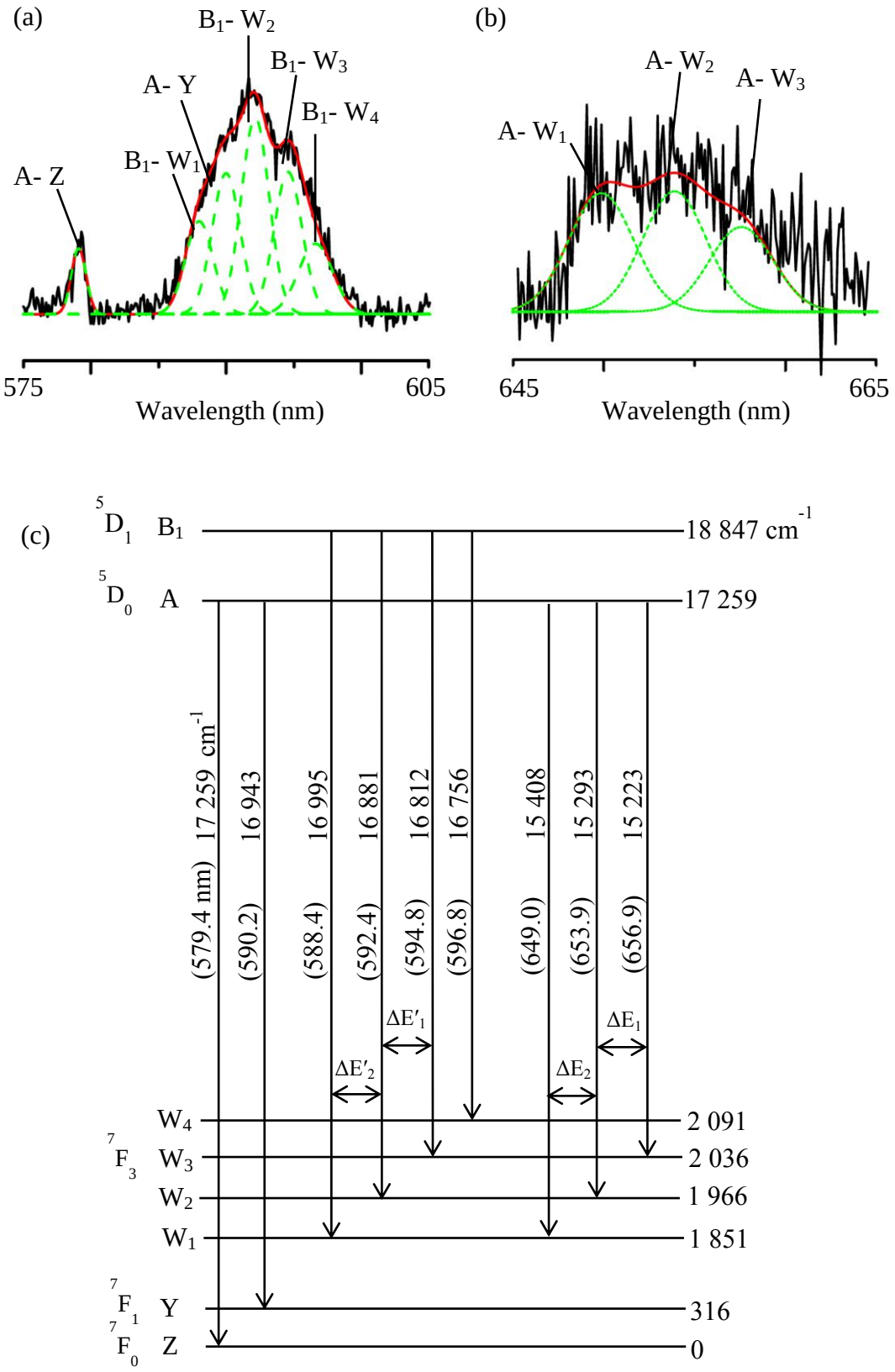

Figure 5.8 Room temperature (300 K) Gaussian curve fittings for (a) the $^5D_0$ (A) → $^7F_0$ (Z), $^5D_0$ (A) → $^7F_1$ (Y) and $^5D_1$ (B) → $^7F_3$ (W) and (b) the $^5D_0$ (A) → $^7F_3$ (W) emission bands for 1 mol% Eu^{3+} doped ZnO. The corresponding transitions between crystal-field energy levels are as shown in (c).

Although the $^5D_0$ (A) $\rightarrow ^7F_0$ (Z) transition is allowed with respect to the crystal-field selection rules, ($\Gamma_1 \rightarrow \Gamma_1$, section 2.6; table 2.2), the transition violates the spin and parity selection rules under which the J = 0 → J = 0 transition is forbidden for the electric-dipole case [56]. However due to the spin-orbit coupling interaction the spin selection rule is relaxed [95]. The electric potential from the surrounding ligands causes J-mixing of the levels in the $^7F_0$ and $^7F_2$ multiplets [95]. This J-mixing partially lifts the parity selection rule which forbids a J = 0 → J = 0 transition [95] rendering the $^5D_0$ (A) $\rightarrow ^7F_0$ (Z) transition weakly observable as shown in figure 5.8 (a). In addition, the $^5D_0 \rightarrow ^7F_3$ transitions are only weakly observed because they are a result of J mixing of the $^7F_2$, $^7F_3$ and $^7F_4$ multiplets by the crystal-field potential. This mixing occurs via lattice vibrations and the associated electron-phonon interaction results in the broader linewidths for the $^5D_0 \rightarrow ^7F_3$ transitions.

Using the selection rules (section 2.6; table 2.2), only a single transition is allowed and therefore expected for the $^5D_0 \rightarrow ^7F_1$ emission band centred at 579.0 nm (figure 5.7). However, it is clear from figure 5.8 (a) that there are more than three peaks in the experimental data. In fact, five Gaussian peaks were required to satisfactorily fit the data. A single Gaussian curve, corresponding to the single A→Y transition (figure 5.8 (a)), could not satisfactorily fit the observed $^5D_0 \rightarrow ^7F_1$ emission band. To address this apparent contradiction, the $^5D_0 \rightarrow ^7F_3$ emission band centred at 650.0 nm (figure 5.7) was analysed instead. A total of three peaks were satisfactorily fitted as shown in figure 5.8 (b) resulting in the identification of three crystal-field energy levels of the $^7F_2$ (W) multiplet at 1 851 cm^{-1} (W_1), 1 966 cm^{-1} (W_2) and 2 036 cm^{-1} (W_3) as shown in figure 5.8 (c). Three of the five fitted peaks had energy separations of ΔE_1 = 70 cm^{-1} and ΔE_2 = 115 cm^{-1}. These energy separations matched the separations $\Delta E'_1$ and $\Delta E'_2$ between the three peaks fitted to the band centred at 592.0 nm. The three transitions at 16 995 cm^{-1} (588.4 nm), 16 881 cm^{-1} (592.4 nm) and 16 812 cm^{-1} (594.8 nm) were therefore assigned to originate from a $^5D_1$ multiplet level (B_1) at 18 847 cm^{-1} to the common W_1, W_2 and W_3 levels of the $^7F_3$ multiplet (figure 5.8 (c)). The low-lying level of the $^5D_1$ multiplet (18 847 cm^{-1}) deduced in this work is relatively higher compared to the

18 690 cm^{-1} energy deduced by Gruber et al. [96] for AlN:Eu^{3+}crystals. The remaining two transitions at 16 943 cm^{-1} (590.2 nm) and 16 756 cm^{-1} (596.8 nm) were then assigned as $^5D_0$ (A) → $^7F_1$ (Y) and $^5D_1$ (B_1) → $^7F_3$ (W_4) transitions, respectively. The chosen A → Y transition places the Y level at 316 cm^{-1} above the ground state which is consistent with the energy diagram (figure 2.7) of Eu^{3+}. This way, the anomaly of five Gaussian peaks for the emission band at 592.0 nm is resolved convincingly.

From the selection rules in table 2.2, three $^5D_0$ (A) → $^7F_3$ (W) crystal-field transitions are expected since the A level is necessarily of the Γ_1 irrep. The W_1, W_2 and W_3 levels should then comprise of the $\Gamma_1+2\Gamma_3$ irreps (table 2.1) for all three transitions to be observed. The fact that transitions from B_1 to all three (W_1, W_2 and W_3) crystal-field energy levels and the W_4 level are observed implies that B_1 is of the Γ_3 irrep since a Γ_2 → Γ_1 type transition is forbidden (table 2.2).

A total of four crystal-field energy levels were deduced for the $^7F_3$ multiplet (figure 5.8 (c)) instead of the five expected from the group theory predictions for a Γ_3 excited level. The missing transition could be quite weak as an additional Gaussian curve could not be accommodated. Similarly, for the $^5D_0$ (A) →$^7F_2$ (X) and $^5D_1$ (B) →$^7F_4$ (V) transition band centred at 615.0 nm, five Gaussian curves were fitted (figure 5.9 (a)) and they correspond to overlapping $^5D_0$ (A) →$^7F_2$ (X) and $^5D_1$ (B) →$^7F_4$ (V) transitions (figure 5.9 (c)). A total of five peaks were fitted to the $^5D_0$ (A) →$^7F_4$ (V) transition band centred at 699.0 nm as shown in figure 5.9 (b). From the Gaussian fittings, three and six crystal-field energy levels were deduced for the $^7F_2$ and $^7F_4$ multiplets (figure 5.9 (c)), respectively, and this is consistent with the theoretical predictions. Based on the calibration measurements that were carried out using a source of known wavelength (He-Ne laser 632.8 nm), an experimental error of ±2 cm^{-1} was determined for all the deduced energy values. The crystal-field energy levels deduced for the $^5D_{0,1}$ and the ^7F_J (J = 0 to 4) multiplets of Eu^{3+} in ZnO are summarised in table 5.2 .

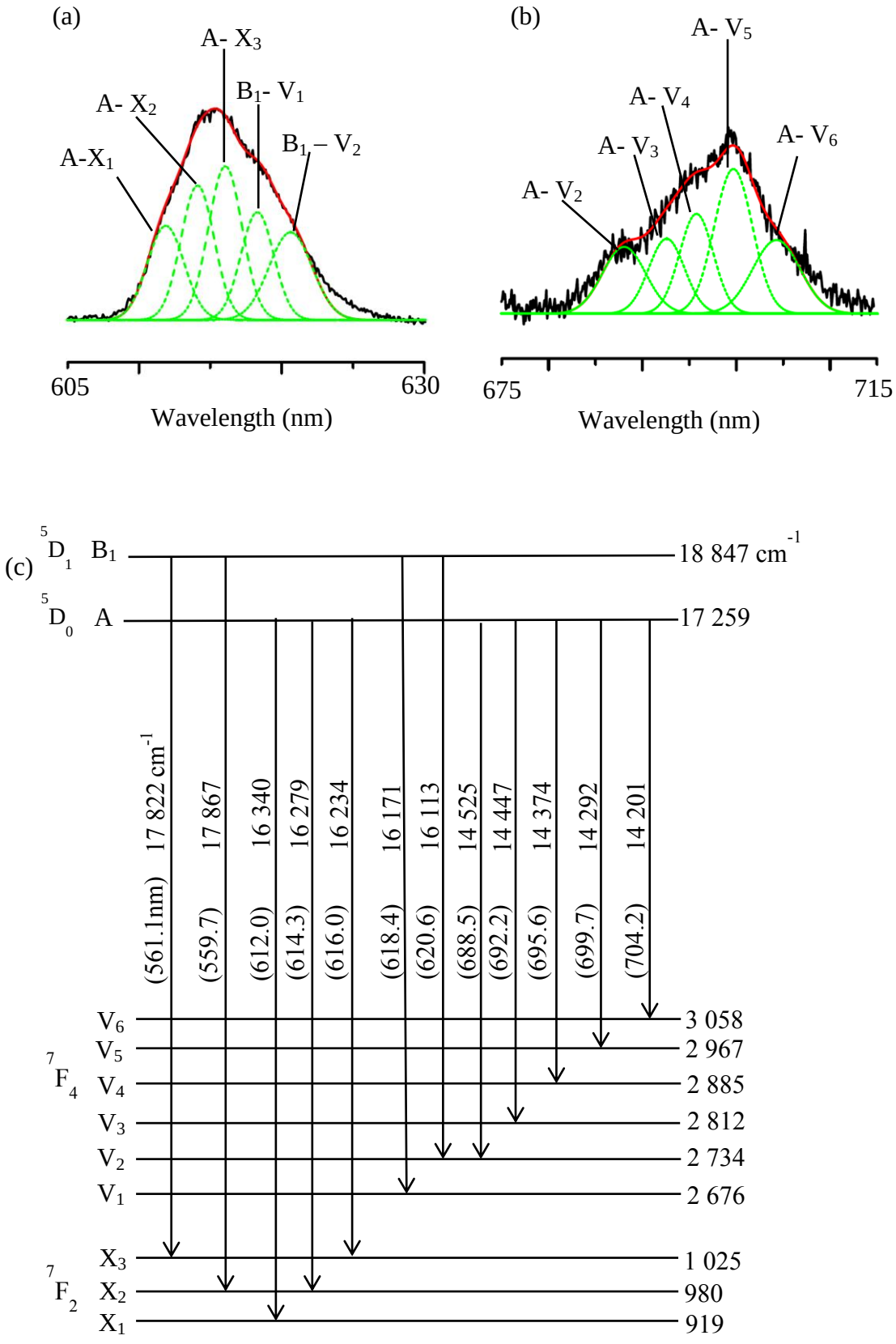

Figure 5.9 Room temperature (300 K) Gaussian curve fittings for (a) the overlapping $^5D_0$ (A) $\rightarrow{}^7F_2$ (X) and $^5D_1$ (B) $\rightarrow{}^7F_4$ (V) and (b) the $^5D_0 \rightarrow {}^7F_4$ emission bands for 1 mol% Eu^{3+} doped ZnO. The corresponding transitions between crystal-field energy levels are as shown in (c).

Table 5.2 Crystal-field energy levels of the Eu^{3+} ion in ZnO in cm^{-1} (± 2 cm^{-1}).

Multiplet	$^7F_0$	$^7F_1$	$^7F_2$	$^7F_3$	$^7F_4$	$^5D_0$	$^5D_1$
Levels	0	316	919	1 851	2 676	17 259	18 847
			980	1 966	2 734		
			1 025	2 036	2 812		
				2 091	2 885		
					2 967		
					3 058		

5.2.3.3 Energy transfer in ZnO:Eu^{3+}

The only possible energy transfer mechanism for the excitation of the Eu^{3+} ion involves donor defect levels below the CB [24]. This is because the blue-laser excitation energies are lower than the required 27 132cm^{-1} (369 nm) for ZnO VB-to-CB excitation. Therefore electrons from the VB can only be excited to some defect level below the conduction band. It is these defect levels rather than the RE^{3+} levels that have to be in resonance with or within a few phonons of the pump laser lines for excitation to occur.

In the literature, Srivastava et al. [29] identified several defect levels which are accessible with the excitation wavelengths used in the present work, as shown in figure 2.5. The V_{Zn}^{2-} (22 221 cm^{-1}) defect level can be populated by the 457.9 nm (21 839 cm^{-1}) excitation line while population of the Zn_i^+ (21 094 cm^{-1}) transition level is most likely with the 476.5 nm (20 986 cm^{-1}) and 488.0 nm (20 492 cm^{-1}) excitation wavelengths (figure 5.10). The maximum longitudinal optical (LO) phonon energy associated with ZnO has been reported to be in the 580 cm^{-1} region [97]. Therefore, absorption of one or two phonons together with the laser excitation energies is sufficient to excite electrons from the VB to either the V_{Zn}^{2-} or the Zn_i^+ defect levels. To populate the V_{Zn}^{2-} defect level using the 457.9 nm excitation line (figure 5.10), 382 cm^{-1} of phonon energy is required while the 476.5 nm and the 488.0 nm excitation lines require 108 cm^{-1} and 650 cm^{-1} of phonon energy, respectively, to populate the Zn_i^+ defect level. The excited electrons then undergo non-radiative transitions from the V_{Zn}^{2-} and Zn_i^+ defect levels to the V_O^+ and O_i transition levels via a non-radiative center

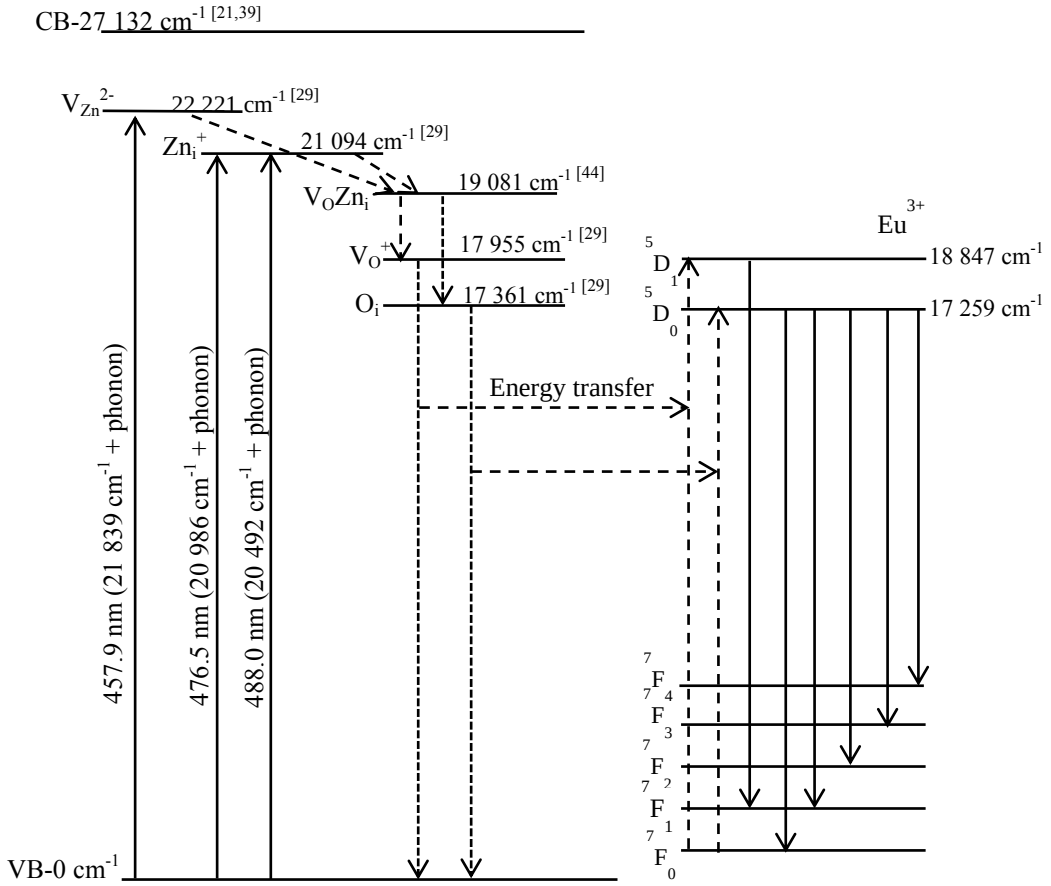

Figure 5.10 Schematic illustrating the possible energy transfer processes from the ZnO host to the Eu^{3+} ions. The dashed lines represent the ZnO to Eu^{3+} ion energy transfer due to defect related transitions. (1eV = 8 051 cm^{-1}).

(V_OZn_i defect complex) as shown in figure 5.10. As discussed in sections 2.3 and 4.2.2, the V_OZn_i defect complex facilitates non-radiative relaxation between single defects. The electrons then decay to the VB in the process transferring energy to the Eu^{3+} ion resulting in the population of the $^5D_1$ (18 847 cm^{-1}) and $^5D_0$ (17 259 cm^{-1}) multiplets as shown in figure 5.10. The $V_O^+ \rightarrow$VB and $O_i \rightarrow$VB transitions match the $^7F_0 \rightarrow {}^5D_1$ and $^7F_0 \rightarrow {}^5D_0$ transition energies, respectively, to within one or two phonons and are hence the most probable intermediaries for efficient energy transfer. The excited electrons in the $^5D_1$ and $^5D_0$ multiplets then radiatively decay to the terminal ^7F_J multiplets leading to the observed Eu^{3+} emission bands in figure 5.7. The V_{Zn}^{2-} defect level is 3 140 cm^{-1} higher than the V_OZn_i defect complex level while the Zn_i^+ defect level is only 2 013 cm^{-1}. As such with the 457.9 nm excitation route, there is a larger energy

difference (3 140 cm^{-1}) as compared to the 476.5 nm or 488.0 nm excitation route (2 013 cm^{-1}). It is therefore expected that the 476.5 nm or 488.0 nm excitation route will be more favourable for efficient energy transfer in comparison. This is consistent with the photoluminescence results where spectra obtained with either 476.5 nm or 488.0 nm excitation lines have relatively intense Eu^{3+} emission (figure 5.7) as compared to the spectrum obtained with 457.9 nm excitation.

5.2.3.4 ZnO:Tb^{3+} photoluminescence

Photoluminescence spectra of 1.0 mol% Tb^{3+} doped ZnO (B sample) obtained with the 457.9 nm, 476.5 nm and 488.0 nm excitation wavelengths are presented in figure 5.11. The spectrum for the ZnO:Tb^{3+} (A) sample (not presented) did not exhibit any Tb^{3+} related emission bands and this is consistent with the absence of Tb^{3+} peaks in the corresponding EDS spectrum (figure 5.4 (b); section 5.2.2). The photoluminescence spectrum for undoped ZnO is not included because the sample was not available. However for the ZnO:Eu^{3+} photoluminescence spectra obtained with 476.5 nm and 488.0 nm excitation, the broad background emission on which the Eu^{3+} emission bands are superimposed follows the same profile as that of the undoped ZnO spectrum (figure 5.7). It is therefore expected that an undoped ZnO sample prepared under the same conditions as the ZnO:Tb^{3+} (B) sample would yield a spectrum similar to the broad background emission in the ZnO:Tb^{3+} (B) spectra obtained with 457.9 nm and 476.5 nm excitation (figure 5.11) [2]. The observed broad background emission spans the visible region of the electromagnetic spectrum (480.0 nm – 650.0 nm). As the excitation wavelength is increased from 457.9 nm to 476.5 nm the Tb^{3+} emission bands increase in intensity. The 488.0 nm excitation wavelength happens to be in resonance with the $^5D_4$ multiplet of Tb^{3+} and as a result, the Tb^{3+} emission is significantly stronger relative to the emission obtained with the 457.9 nm and 476.5 nm excitation lines and the background emission is supressed.

The Tb^{3+} emission band at 542.0 nm (figure 5.11) was observed with all three excitation lines, with the 457.9 nm excitation wavelength giving the least intensity. The spectrum obtained with the 476.5 nm excitation line shows four broad peaks centred at 488.0 nm, 542.0 nm, 585.0 nm and 622.0 nm. With the 488.0 nm excitation line, the ZnO:Tb^{3+} (B) sample yields a spectrum with a total

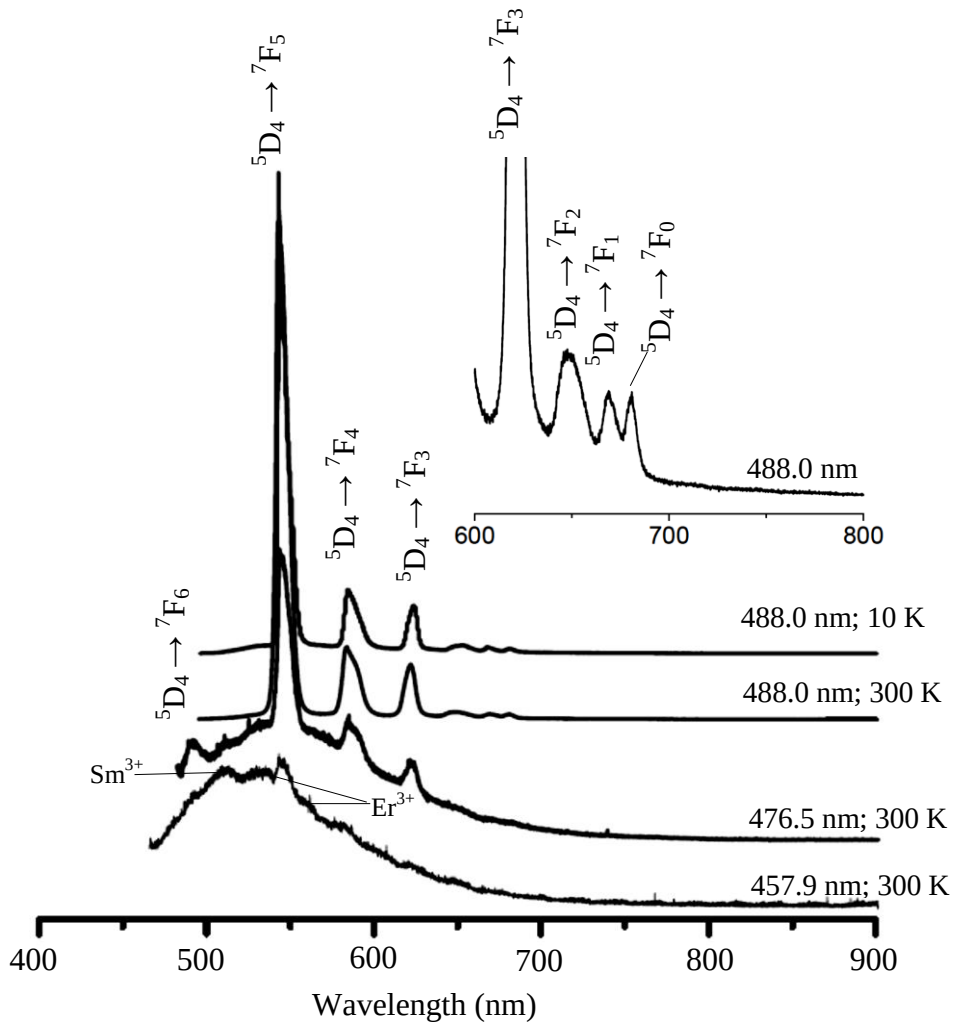

Figure 5.11 Room temperature (300 K) and 10 K photoluminescence spectra of 1 mol% Tb^{3+} doped ZnO (B sample) obtained with the 457.9 nm, 476.5 nm and 488.0 nm excitation lines.

of six peaks. The three broad peaks at 542.0 nm, 585.0 nm and 622.0 nm are as obtained with the 476.5 nm excitation line while the additional three weaker peaks centred at 650.0 nm, 668.0 nm and 680 nm (figure 5.11 insert) were not observed with the lower wavelength excitation line. Figure 5.11 also shows the ZnO:Tb^{3+} (B) photoluminescence spectrum obtained at 10 K using the 488.0 nm excitation line. There was no change in the peak positions of the Tb^{3+} emission bands at the lower temperature however the linewidths were slightly narrower compared to the 300 K spectrum. For example, the 542.0 nm and 622.0 nm peaks have linewidths (full-widths at half maximum-FWHM) of 8.4 nm and

12.7 nm, respectively, at room temperature and at 10 K the corresponding linewidths are 7.0 nm and 11.2 nm, respectively.

The broad background emission centred at 530.0 nm obtained with the 457.9 nm and 476.5 nm excitation lines is attributed to intrinsic defect level transitions from the ZnO host [29,98]. The green, yellow-orange and red emission can be attributed to the defect level transitions discussed in section 5.2.3.1 while the blue emission (470.0 nm-500.0 nm) observed with 457.9 nm excitation is attributed to the $Zn^{+}_{i} \rightarrow VB$ [29] transition. Similar to Eu^{3+}, the intrinsic defect level transitions are essential for the indirect excitation of the Tb^{3+} ion through energy transfer processes [2] which will be discussed in section 5.2.3.6.

The Tb^{3+} emission bands presented in figure 5.11 are due to electronic transitions from the $^5D_4$ multiplet at 488.2 nm (20 483 cm^{-1}) to all the ^7F_J (J = 0, 1, 2, 3, 4, 5, 6) multiplets. The $^5D_4 \rightarrow {}^7F_6$ transition (488.2 nm emission) was only clearly observed with the 476.5 nm excitation line as it is inevitably filtered out with the 488.0 nm excitation line and is far too weak to observe with the 457.9 nm excitation line. Transitions to the $^7F_2$, $^7F_1$ and $^7F_0$ multiplets were quite weak by comparison as shown in the insert of figure 5.11. The $^5D_4 \rightarrow {}^7F_{6,5,4,3}$ emission bands are as reported in the literature, from ultra-violet excitation studies [2,16], while the $^5D_4 \rightarrow {}^7F_{2,1,0}$ emission bands centred at 650.0 nm, 668.0 nm and 680.0 nm, respectively, have not been reported before. Crystal-field energy levels associated with the observed Tb^{3+} ion emission bands are discussed in the next section.

The additional relatively weak emission bands observed at 510.0 nm, 531.0 nm and 558.0 nm (figure 5.11) with the 457.9 nm excitation line could be due to traces of samarium and erbium impurities present in the starting materials. The 457.9 nm excitation energy matches $^4F_{5/2}$ and $^4F_{15/2}$ multiplets of the Sm^{3+} and Er^{3+} ions, respectively. The emission band at 510.0 nm could therefore be attributed to the $^4F_{3/2} \rightarrow {}^6H_{5/2}$ transition of the Sm^{3+} ion (figure 5.11). The 531.0 nm and 558.0 nm emission could be due to the $^2H_{11/2} \rightarrow {}^4I_{15/2}$ and $^4S_{3/2} \rightarrow {}^4I_{15/2}$ transitions, respectively, of the Er^{3+} ion (figure 5.11).

5.2.3.5 Tb^{3+} crystal-field energy levels

The Tb^{3+} crystal-field energy levels were deduced using the same deconvolution procedure as applied to the Eu^{3+} emission bands in section 5.2.3.2. The 10 K spectrum was considered first as all the excited electrons are most likely to occupy the lowest emitting level (denoted by A_1 in figure 5.12(b)) of the excited $^5D_4$ multiplet at this temperature, resulting in fewer emission transitions. Governed by the selection rules, the $^5D_4$ (A) $\rightarrow ^7F_0$ (T) transition band was fitted first as the $^7F_0$ (T) multiplet has only one energy level and therefore a single transition could be expected. From table 2.1 in section 2.6, the level for J = 0 corresponds to the Γ_1 irrep. The emitting level (A_1) of the $^5D_4$ multiplet can be assigned to only one of the three possible irreps (Γ_1, Γ_2 and Γ_3; table 2.1 in section 2.6). Considering the $^5D_4$ (A) $\rightarrow ^7F_0$ (T) and $^5D_4$ (A) $\rightarrow ^7F_1$ (U) transition bands obtained at 10 K (figure 5.12 (a)) for example, a single Gaussian peak fits the $A_1 \rightarrow$T emission band while two Gaussian peaks are required for the $A_1 \rightarrow$U band. In order to determine the most suitable irrep for the emitting level, a schematic illustration of the crystal-field energy level transitions for the $^5D_4$ (A) $\rightarrow ^7F_0$ (T) and $^5D_4$ (A) $\rightarrow ^7F_1$ (U) bands as shown in figure 5.13 was used. The transitions marked (**×**) in figure 5.13 are electric-dipole forbidden. If the Γ_1 irrep is assigned to the emitting level (A_1) of the $^5D_4$ multiplet (figure 5.13 (a)), the $\Gamma_1 \rightarrow \Gamma_2$ transition is forbidden (section 2.6; table 2.2) and so a single Gaussian curve would be expected to satisfactorily fit the $A_1 \rightarrow$U band at 668.0 nm (figure 5.12 (a)). However this was not achievable as two Gaussian peaks were required. Furthermore if the Γ_2 irrep is assigned to the emitting level (A_1) as shown in figure 5.13 (b), the $\Gamma_2 \rightarrow \Gamma_1$ transition is also forbidden which means that the $A_1 \rightarrow$T emission band at 680.0 nm (figure 5.12 (a)) should be absent from the spectrum, in contradiction to the results presented here. Consequently the Γ_1 and Γ_2 irreps are inappropriate assignments for the A_1 crystal-field energy level. Assigning the Γ_3 irrep to the emitting level (A_1) (figure 5.13 (c)) results in three $A_1 \rightarrow$U,T allowed electric-dipole transitions which are consistent with the three fitted curves in the $^5D_4$ (A) $\rightarrow ^7F_0$ (T) and $^5D_4$ (A) $\rightarrow ^7F_1$ (U) transition bands. As such the Γ_3 irrep is the most suitable assignment for the A_1 crystal-field level of the $^5D_4$ multiplet.

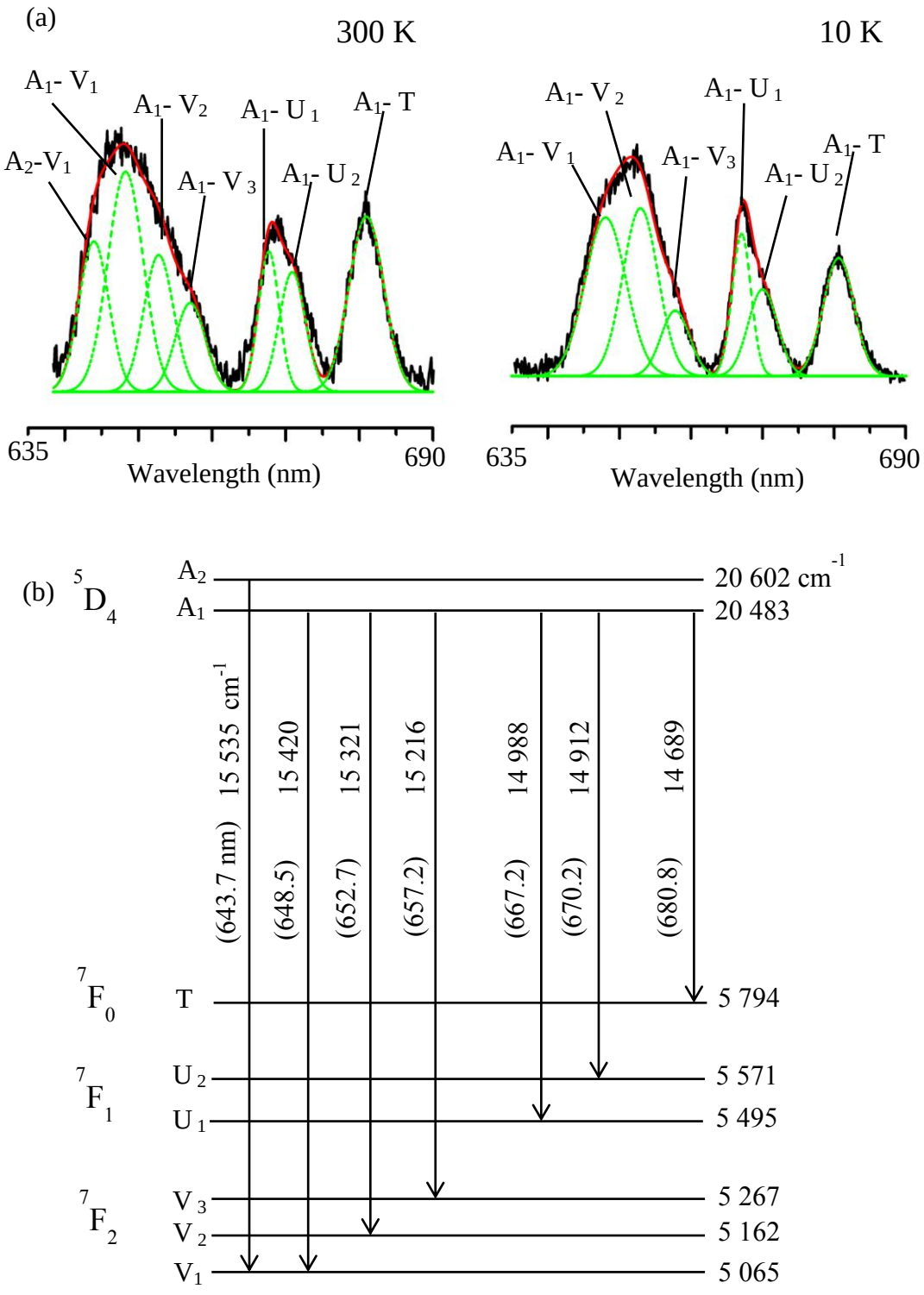

Figure 5.12 (a) Room temperature (300 K) and 10 K Gaussian curve fittings for the $^5D_4 \rightarrow {}^7F_{0,1,2}$ emission bands in the 1.0 mol% Tb^{3+} doped ZnO (B) and (b) the corresponding transitions between crystal-field energy levels.

Maintaining the Γ_3 irrep for the emitting level (A_1), Gaussian curves were fitted to all the emission bands in the10 K spectrum (figures 5.12 and 5.14 to 5.17) in accordance with the selection rules. Guided by the 10 K fittings and using the same fitted curve peak positions, Gaussian curves were then fitted to the room temperature (300 K) $^5D_4 \rightarrow {}^7F_{0,1,2}$ transition bands and additional Gaussian curves included as necessary. The curve fittings for the $^5D_4$ (A) $\rightarrow {}^7F_0$ (T) and $^5D_4$ (A) $\rightarrow {}^7F_1$ (U) transition bands obtained at 300 K resulted in one and two fitted Gaussian curves, respectively, as for the 10 K fittings (figure 5.12 (a)). However the $^5D_4$ (A) $\rightarrow {}^7F_2$ (V) transition band obtained at 300 K resulted in four

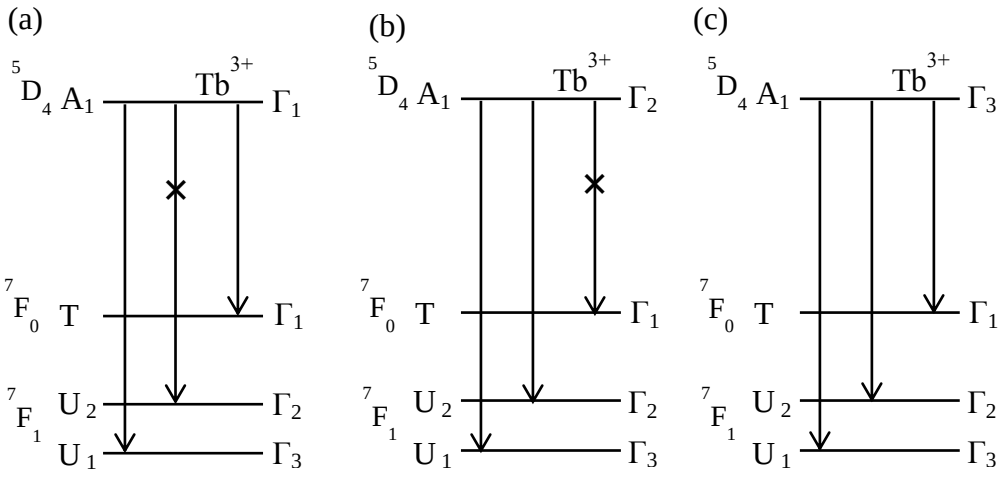

Figure 5.13 A schematic illustration of the crystal-field level transitions for the Tb^{3+} ion with (a) the Γ_1, (b) the Γ_2 and (c) the Γ_3 irreps assigned to the emitting level (A_1) of the $^5D_4$ multiplet. The terminal $^7F_0$ (T) and $^7F_1$ (U) multiplets have the Γ_1, the Γ_2 and Γ_3 irreps, respectively, assigned to the terminating levels. The (×) shows a forbidden electric-dipole transition.

fitted curves as compared to the three curves obtained for the same emission band at 10 K (figure 5.12 (a)). The additional Gaussian curve fitted on the $^5D_4$ (A) $\rightarrow {}^7F_2$ (V) transition band obtained at 300 K corresponds to a transition from the second excited level (A_2) of the $^5D_4$ (A) multiplet to the lowest level (V_1) of the $^7F_2$ (V) multiplet (figure 5.12 (b)). Transitions from the second excited level (A_2) are expected at room temperature (300 K) as electrons have sufficient thermal energy to occupy this level. As such additional transitions from the higher A_2 level at 20 602 cm^{-1} are present as well and mixed in with those from the lower A_1 level at 20 483 cm^{-1} (figure 5.12 (b)). The additional

fitted curve is consistent with the observed broadening of the Tb^{3+} emission bands obtained at 300 K. From the Gaussian curve fittings, one crystal-field energy level was deduced for the $^7F_0$ (T) multiplet while two and three crystal-field levels where deduced for the $^7F_1$ (U) and $^7F_2$ (V) multiplets, respectively. This is consistent with group theory predictions previously discussed in section 2.6 (table 2.1). Gaussian curves were then fitted to all the Tb^{3+} emission bands obtained at 300 K in the same manner. A total of six curves were fitted to the $^5D_4$ (A) $\rightarrow ^7F_3$ (W) transition band obtained at 300 K as compared to the five curves that were fitted to the same emission band obtained at 10 K (figure 5.14 (a)). The extra fitted curve on the 300 K emission band corresponds to a transition from the higher A_2 level of the $^5D_4$ (A) multiplet to the third level (W_3) of the $^7F_3$ (W) multiplet (figure 5.14 (b)). Seven and six Gaussian curves were fitted to the $^5D_4$ (A) $\rightarrow ^7F_4$ (X) transition band obtained at 300 K and at 10 K, respectively, (figure 5.15 (a)). The additional curve for the room temperature (300 K) emission band corresponds to the $A_2 \rightarrow X_1$ transition as shown in figure 5.15 (b). From the $^5D_4$ (A) $\rightarrow ^7F_3$ (W) and $^5D_4$ (A) $\rightarrow ^7F_4$ (X) transition bands, five and six crystal-field energy levels were deduced for the $^7F_3$ (W) and $^7F_4$ (X) multiplets, respectively, which is in agreement with the theory in section 2.6 (table 2.1). Similar fittings resulted in a total of seven fitted curves for the $^5D_4$ (A) $\rightarrow ^7F_5$ (Y) transition band obtained 300 K while for the same emission band at 10 K a total of six curves were fitted (figure 5.16 (a)). The additional curve from the emission band obtained at 300 K corresponds to the $A_2 \rightarrow Y_2$ transition as shown in figure 5.16 (b). Six crystal-field energy levels of the $^7F_5$ (Y) multiplet were deduced from the curves fitted to the $^5D_4$ (A) $\rightarrow ^7F_5$ (Y) transition band instead of the seven theoretically expected crystal-field levels (section 2.6; table 2.1); the missing transition could be either too weak or overlapping with one of the observed transitions. Gaussian curves were then fitted to the $^5D_4$ (A) $\rightarrow ^7F_6$ (Z) transition band obtained with 476.5 nm excitation (figure 5.17 (a)) as this emission could only be observed with this excitation line (figure 5.11) as earlier explained in section 5.2.3.4. The $^5D_4$ (A) $\rightarrow ^7F_6$ (Z) transition band obtained at 300 K resulted in a total of five fitted curves while a total of three curves were fitted to the corresponding transition band obtained at

10 K (figure 5.17 (a)). The two additional curves on the $^5D_4$ (A) $\rightarrow$$^7F_6$ (Z) transition band obtained at 300 K correspond to the $A_2 \rightarrow Z_1$ and $A_2 \rightarrow Z_4$ transitions as shown in figure 5.17 (b). With the $^5D_4$ (A) $\rightarrow$$^7F_6$ (Z) transition band, only two and four crystal-field levels were deduced for the $^5D_4$ (A) and the $^7F_6$ (Y) multiplets, respectively, instead of six for the $^5D_4$ (A) multiplet and nine for the $^7F_6$ (Y) multiplet as expected from the group theory predictions (section 2.6; table 2.1). The electronic transitions between some of the crystal-field energy levels are forbidden (section 2.6; table 2.2) resulting in fewer than expected experimentally-determined levels for some of the multiplets.

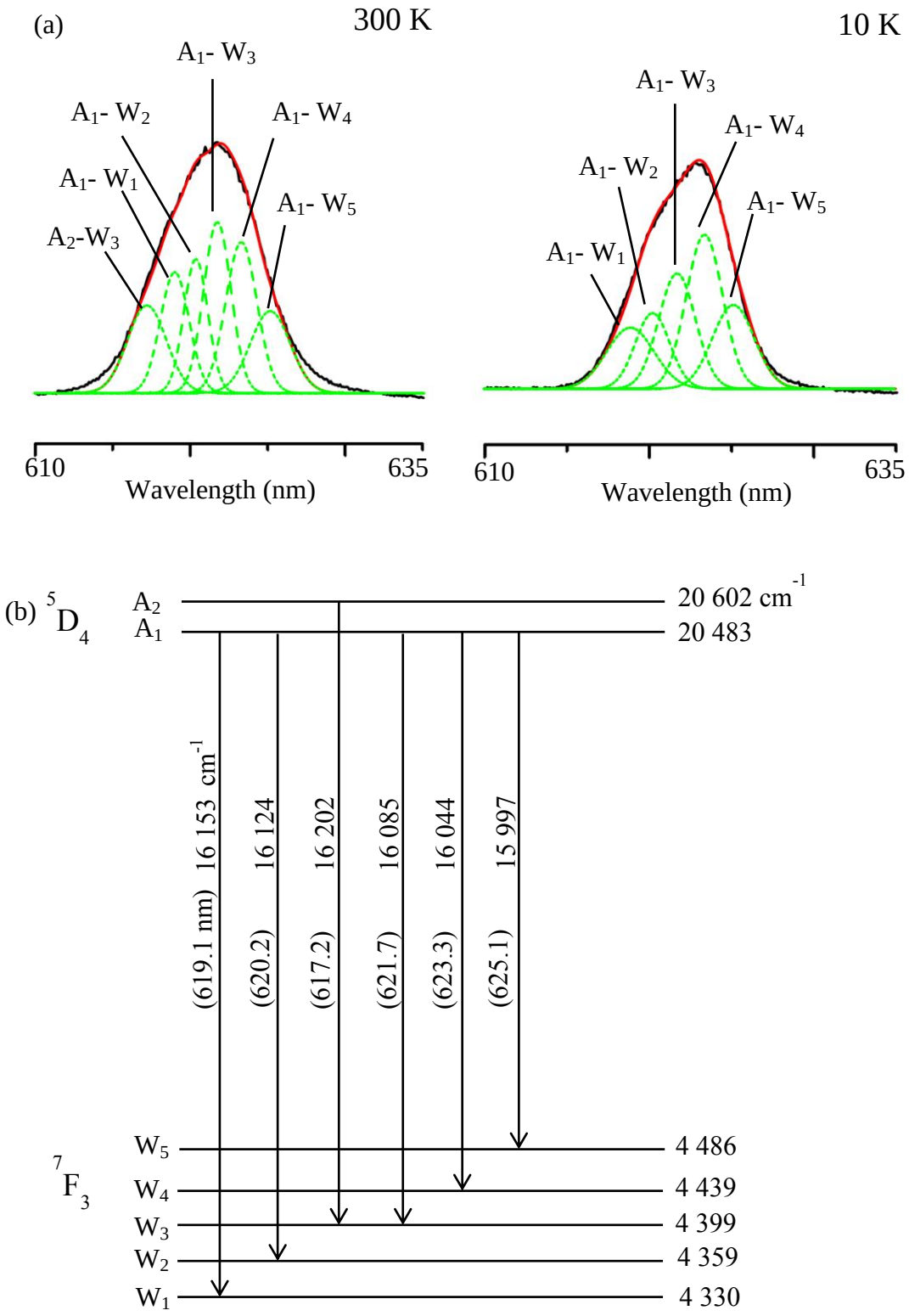

Figure 5.14 (a) Room temperature (300 K) and 10 K Gaussian curve fittings for the $^5D_4 \rightarrow {}^7F_3$ emission band in the 1.0 mol% Tb^{3+} doped ZnO (B) and (b) the corresponding transitions between crystal-field energy levels.

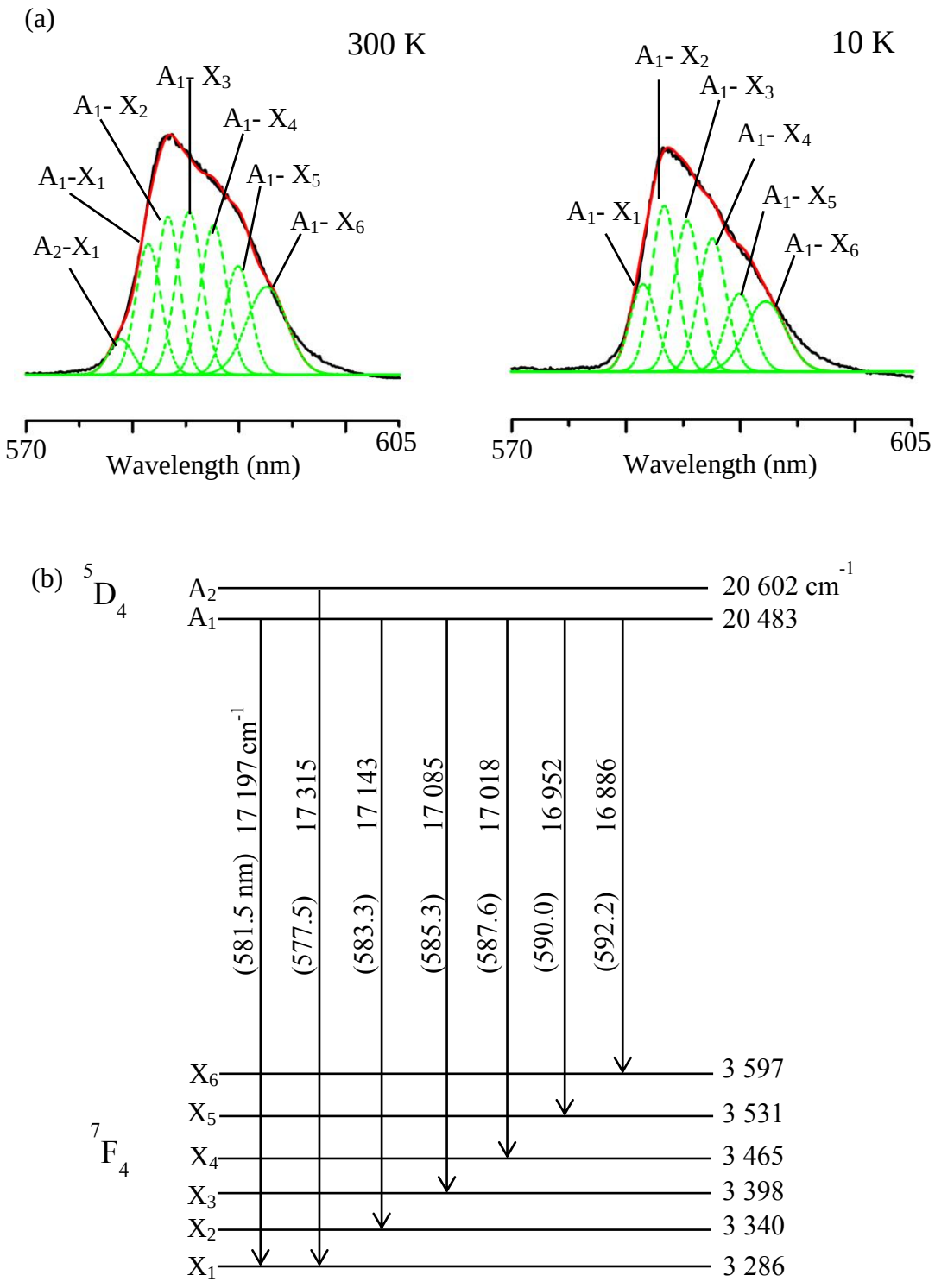

Figure 5.15 (a) Room temperature (300 K) and 10 K Gaussian curve fittings for the $^5D_4 \rightarrow {}^7F_4$ emission band in the 1.0 mol% Tb^{3+} doped ZnO (B) and (b) the corresponding transitions between crystal-field energy levels.

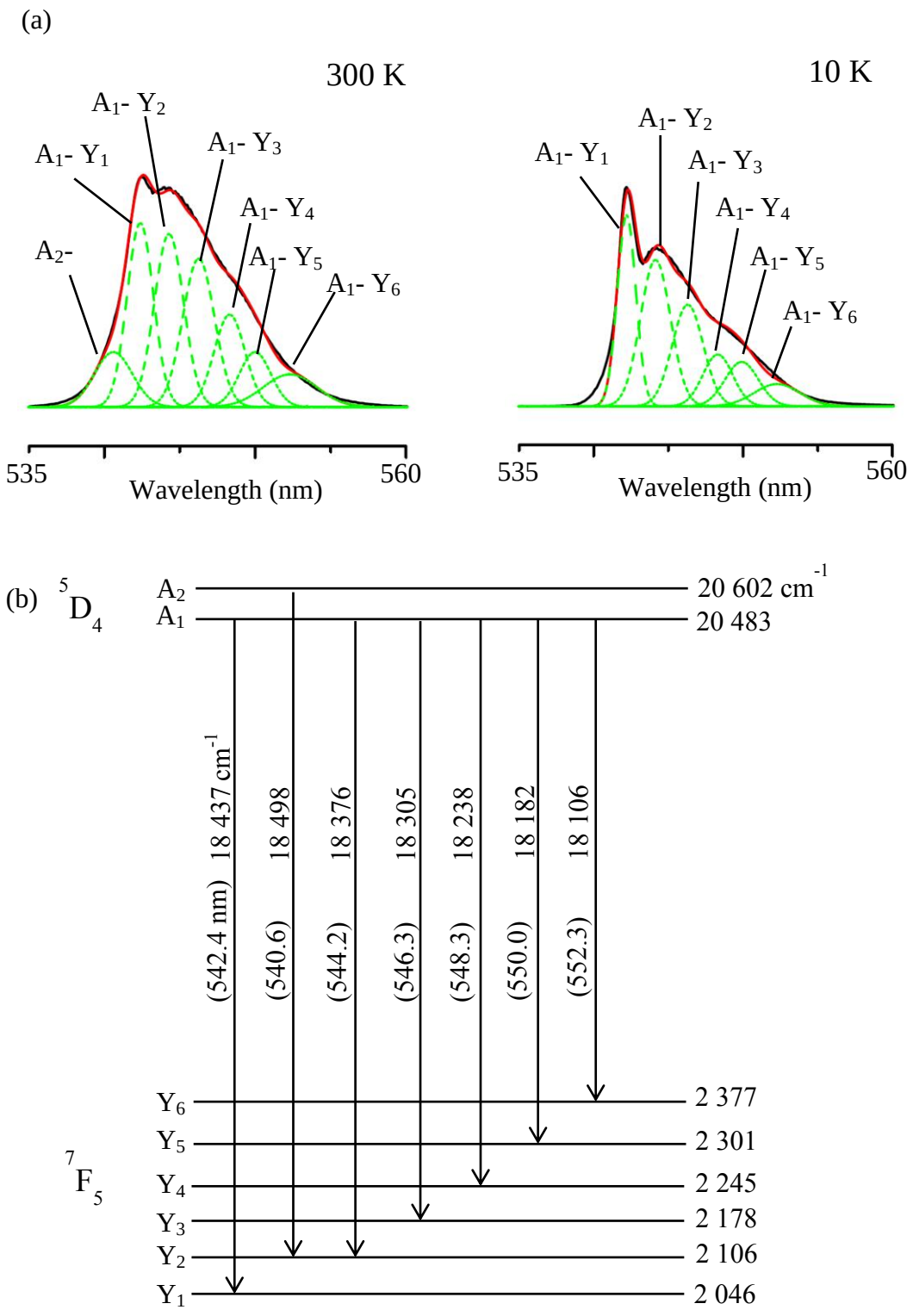

Figure 5.16 (a) Room temperature (300 K) and 10 K Gaussian curve fittings for the $^5D_4 \rightarrow {}^7F_5$ emission band in the 1.0 mol% Tb^{3+} doped ZnO (B) and (b) the corresponding transitions between crystal-field energy levels.

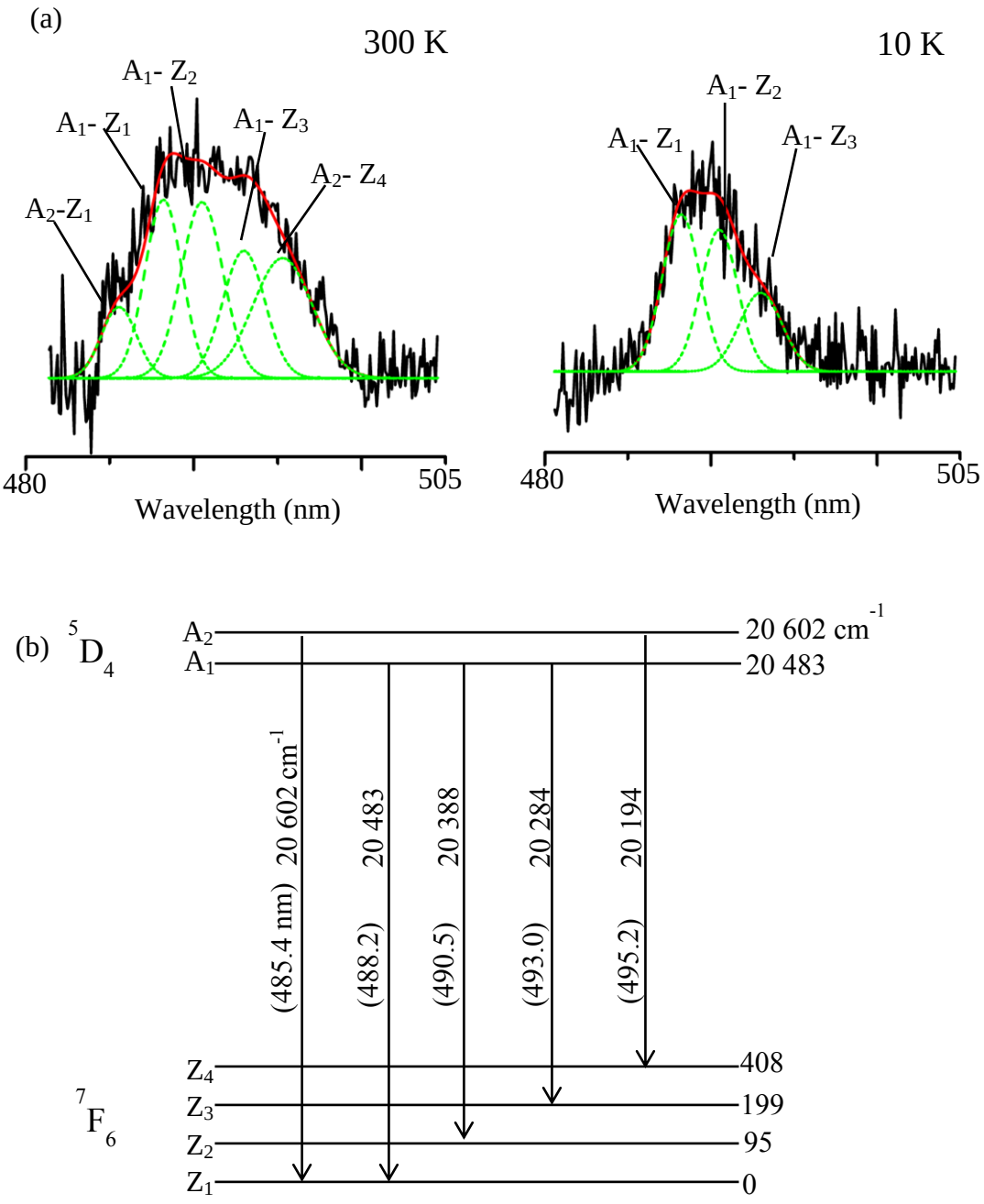

Figure 5.17 (a) Room temperature (300 K) and 10 K Gaussian curve fittings for the 1.0 mol% Tb^{3+} doped ZnO (B) and (b) the corresponding transitions between crystal-field energy levels for the $^5D_4 \rightarrow {}^7F_6$ emission band obtained with 476.5 nm excitation.

At low temperatures (10 K) radiative transitions to the higher X levels such as X_4, X_5 and X_6 are coupled to the ion-lattice relaxations to the lower lying levels (X_1, X_2 and X_3) in accordance with the Boltzmann distribution function $\sim e^{\frac{-\Delta E}{kT}}$ where ΔE is measured from the lowest level. At 300 K, non-radiative relaxation is

reduced for levels in the multiplets within energy kT of the lowest level. This leads to the observed redistribution of intensity with change in temperature. A summary of the crystal-field energy levels determined here for the $^5D_4$ and the ^7F_J (J = 0, 1, 2, 3, 4, 5, 6) multiplets of Tb^{3+} in ZnO is presented in table 5.3.

Table 5.3 Crystal-field energy levels of the Tb^{3+} ion in ZnO in cm^{-1} (± 2 cm^{-1}).

Multiplet	$^7F_6$	$^7F_5$	$^7F_4$	$^7F_3$	$^7F_2$	$^7F_1$	$^7F_0$	$^5D_4$
Levels	0	2 046	3 287	4 330	5 065	5 495	5 794	20 483
	95	2 106	3 340	4 359	5 162	5 571		20 602
	199	2 178	3 398	4 399	5 267			
	408	2 245	3 465	4 439				
		2 301	3 531	4 486				
		2 377	3 597					

5.2.3.6 Energy transfer in ZnO:Tb^{3+}

Similar to the Eu^{3+} ion, excitation of the Tb^{3+} ion in ZnO is via an energy exchange process involving ZnO intrinsic defect level transitions. However of the three blue-laser excitation lines, the 488.0 nm (20 492 cm^{-1}) excitation wavelength is in resonance with the $^5D_4$ multiplet of the Tb^{3+} ion hence direct excitation is expected to be dominant. For this reason, the 488.0 nm excitation line will not be considered in the possible ZnO to Tb^{3+} ion energy transfer process discussed below. On the other hand, the 457.9 nm (21 839 cm^{-1}) and the 476.5 nm (20 986 cm^{-1}) laser line energies are not close to the $^5D_4$ multiplet for direct excitation to occur. Population of the $^5D_4$ multiplet is therefore via energy transfer mechanisms. However the $^5D_4$ multiplet of the Tb^{3+} ion is much higher as compared to the $^5D_{0,1}$ multiplets of the Eu^{3+} ion. As such the transitions responsible for energy transfer from the ZnO defect levels to the Tb^{3+} ion are expected to be of relatively higher energy. Electrons in the VB experience phonon assisted excitation as shown in figure 5.18 to the Zn_i^+ and the V_{Zn}^{2-} defect levels. The excited electrons then undergo non-radiative transitions from the Zn_i^+ and the V_{Zn}^{2-} defect levels to the VB and in the process, transfer energy to the Tb^{3+} ion thereby populating the $^5D_4$ multiplet as shown in figure 5.18. The

$Zn_i^{+} \rightarrow$VB and the $V_{Zn}^{2-} \rightarrow$VB transitions are expected for energy exchange as they match the $^5D_4$ multiplet energy (figure 5.18) instead of the $V_O^{+} \rightarrow$ VB and the $O_i \rightarrow$ VB transitions (figure 5.10) that better match the $^5D_{0,1}$ multiplets of the Eu^{3+} ion.

For this energy transfer mechanism (figure 5.18), excitation with the 457.9 nm

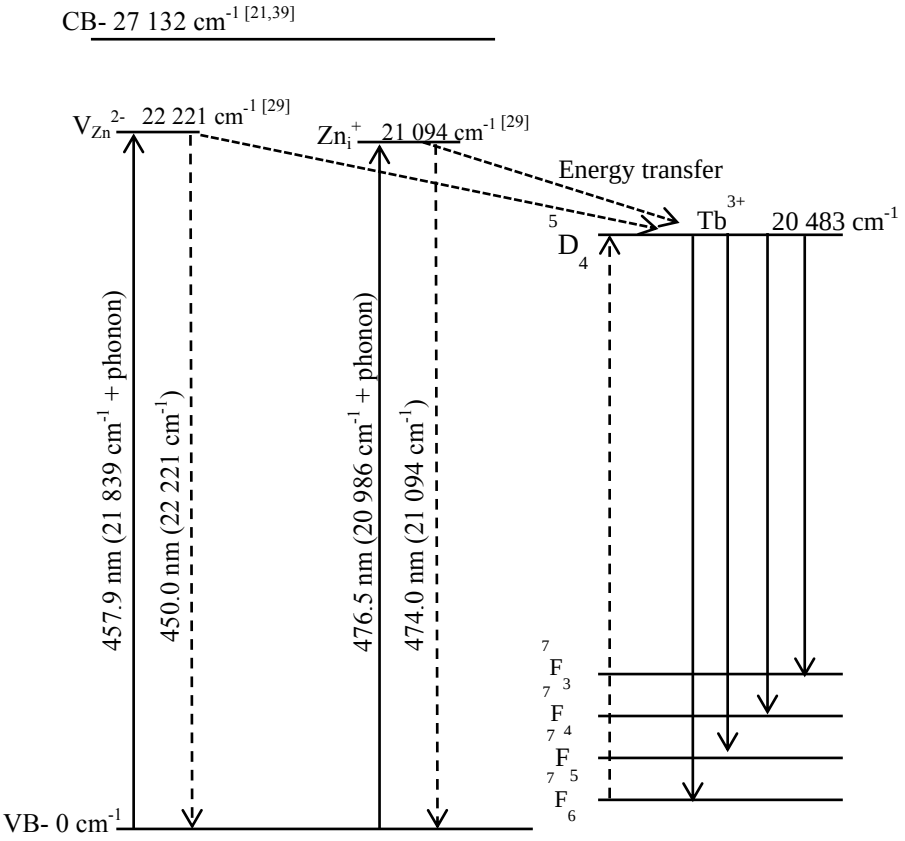

Figure 5.18 Schematic illustrating the possible energy transfer processes from the ZnO host to the Tb^{3+} ions. The dashed lines represent the ZnO to Tb^{3+} ion energy transfer due to defect related transitions. (1 eV = 8 051 cm^{-1}).

laser line requires 382 cm^{-1} of phonon energy to populate the V_{Zn}^{2-} defect level while excitation with the 476.5 nm wavelength needs 108 cm^{-1} of phonon energy to populate the Zn_i^{+} defect level. The V_{Zn}^{2-} defect level is 1 738 cm^{-1} higher than the $^5D_4$ multiplet while the Zn_i^{+} defect level is only 611 cm^{-1} higher than $^5D_4$ multiplet (figure 5.18). Therefore energy transfer from the V_{Zn}^{2-} defect level following 457.9 nm excitation to the $^5D_4$ multiplet would be expected to be less efficient as a large amount of phonon energy has to be lost to match the $^5D_4$ multiplet energy as compared to the Zn_i^{+} route. This is consistent with the

photoluminescence results in figure 5.11 where the spectrum obtained with 457.9 nm excitation line has the least Tb^{3+} emission intensity.

A summary and conclusion of the photoluminescence and characterisation studies for undoped ZnO, Tb^{3+} and Eu^{3+} doped ZnO powders that have been discussed in this chapter is presented in the next section.

5.3 Conclusions

The XRD results showed no changes in the ZnO phase with the introduction of the Tb^{3+} and Eu^{3+} ions. The Tb^{3+} and the Eu^{3+} doped as well as undoped ZnO powders showed only slight compressive microstrain as deduced from the Williamson-Hall analysis. The crystallite sizes of the powders as determined from the Williamson-Hall plots are in agreement with those calculated using the Scherrer formula. The laser excited photoluminescence was consistent with the EDS results as presence of Tb^{3+} and Eu^{3+} in the ZnO powders was observed. In addition the SEM and EDS characterisation together with the photoluminescence results showed that the annealing treatment had no significant influence on the morphology, elemental composition and emission properties of the powders, respectively.

Tb^{3+} and Eu^{3+} emission transitions in the visible region of the electromagnetic spectrum were observed in ZnO powders with excitation from the 457.9 nm, 476.5 nm and 488.0 nm argon laser lines. The photoluminescence spectra show strong green emission for ZnO:Tb^{3+} and strong red emission for ZnO:Eu^{3+}. In general, the Eu^{3+} ion emission was weaker than the Tb^{3+} ion emission for the same excitation conditions. This can be attributed to the much larger energy mismatch of the excitation wavelengths in relation to the excited multiplets of the Eu^{3+} ion as compared to the Tb^{3+} ion. The 457.9 nm excitation line showed to be inefficient for populating the emitting multiplets of the Tb^{3+} and the Eu^{3+} ions while the 488.0 nm wavelength was the most suitable excitation line. From the laser-excited photoluminescence, a total of 29 crystal-field energy levels for Tb^{3+} and 17 for Eu^{3+} were determined. ZnO:Tb^{3+} and ZnO:Eu^{3+} can be useful materials for solid-state laser development and for optoelectronic device applications such as green and red light emitting diodes.

Chapter 6

Conclusions and future work

XRD characterisation and blue-laser excited photoluminescence results for ZnO thin films as well as undoped, Eu^{3+} doped and Tb^{3+} doped ZnO powders have been described and analysed.

For the ZnO thin films, variations in the growth conditions have an effect on the preferred growth orientations of the ZnO thin films. This is shown by the changes in the XRD peak intensities of the 2θ angles for the different deposition parameters. Annealing resulted in enhanced XRD peak intensity showing improved crystallinity of the ZnO thin films. The XRD results confirmed the hexagonal wurtzite ZnO phase.

Photoluminescence emission in the visible region of the electromagnetic spectrum was realized using below band-gap excitation. This is shown by the photoluminescence spectra centred at 656.0 nm obtained with the 457.9 nm, 476.5 nm and 488.0 nm excitation lines. Variations in the ZnO thin film deposition conditions (i.e. deposition power, dc bias voltage, nitrogen/argon gas flow and post-deposition annealing) resulted in changes in the photoluminescence emission intensity with no significant change in the peak position and shape of the broad emission band. The broad emission peak has been attributed to the transitions involving the oxygen interstitial defect level at 17 401 cm^{-1} (575.0 nm) above the valence band. This was related to the annealing treatment which caused oxygen-related defect formation on the surface of the ZnO thin films. From the Gaussian peak fittings in the photoluminescence spectrum, the corresponding native point defects and the defect level transitions responsible for the observed broad emission were identified. Possible direct excitation routes that result in the population of the defect levels were suggested. The ZnO thin films obtained using 150 W deposition power, -25 V substrate bias and an argon gas flow (13.0 sccm) environment has a good film-substrate adhesion and yielded a relatively high photoluminescence emission intensity.

For the ZnO powders, the ZnO hexagonal wurtzite structure was confirmed for the annealed samples while the as-prepared powders showed some unreacted precursor XRD peaks attributable to the zinc acetate precursor. The EDS characterisation of the ZnO powders confirmed the presence of the Eu^{3+} and Tb^{3+} dopants while the SEM images showed that the morphologies of the sample powders depend on both the preparation procedure and the dopant RE^{3+} ions incorporated into the powders. This is shown by the change in particle shape with change in preparation procedure and introduction of the Eu^{3+} and Tb^{3+} ions.

Enhanced luminescence in the visible region of the electromagnetic spectrum was realized on incorporation of the Eu^{3+} and Tb^{3+} ions into the ZnO matrix. This is shown in the blue-laser excited photoluminescence spectra of the ZnO:Eu^{3+} and ZnO:Tb^{3+} pellets obtained with the 457.9 nm, 476.5 nm and 488.0 nm excitation lines at 300 K. The ZnO:Eu^{3+} and ZnO:Tb^{3+} samples yield relatively intense emission bands in the red and green regions of the visible spectrum, respectively. It was determined that the intense red emission from the ZnO:Eu^{3+} sample is due to the overlapping $^5D_1 \rightarrow {}^7F_4$ and $^5D_0 \rightarrow {}^7F_2$ electronic transitions of the Eu^{3+} ion while the $^5D_4 \rightarrow {}^7F_5$ transition in the Tb^{3+} ion is responsible for the intense green emission observed for the ZnO:Tb^{3+} sample. Transitions between crystal-field energy levels for a C_{3v} symmetry site for the Eu^{3+} and Tb^{3+} ions were determined and the corresponding crystal-field energy level schemes deduced. Possible excitation and energy transfer mechanisms from the ZnO defects to the RE^{3+} ion have been identified. The ZnO:Eu^{3+} and ZnO:Tb^{3+} emission transitions and crystal-field energy level schemes are of significance for solid-state laser development and for optoelectronic device applications such as red and green light-emitting diodes.

Further work on ZnO thins films and rare-earth doped ZnO powders would include:

(a) photoluminescence measurements on ZnO thin films deposited in an oxygen/argon gas flow at various gas flow ratios to confirm the relation of oxygen defects to the broad emission band centred at 656.0 nm;

(b) a detailed profiling of the effects of the negative substrate bias voltage to establish the threshold bias voltage where etching of the thin film begins to occur;

(c) detailed profiling of various nitrogen/argon gas flow ratios need to be pursued so as to determine the ratio of nitrogen-to-argon gas flow that results in photoluminescence quenching in the ZnO thin films;

(d) determination of the relation of the defect formation energies and the photoluminescence intensity in ZnO thin films;

(e) a detailed investigation of the chemical bath deposition synthesis technique to determine the optimum conditions and procedures for the incorporation Tb^{3+} into the ZnO powders;

(f) investigation of RE^{3+} doping concentration beyond 1 mol% to establish the concentration at which photoluminescence quenching occurs due to high RE^{3+} doping concentration;

(g) investigate the effects of temperature on the ZnO:Eu^{3+} photoluminescence i.e. low temperature (10 K) measurements;

(h) laser excited photoluminescence of Eu^{3+} and Tb^{3+} doped ZnO thin films for comparison with the results obtained for the ZnO:Eu^{3+} and ZnO:Tb^{3+} powders;

(i) investigate the decay life times of the Eu^{3+} and Tb^{3+} emission to determine the respective transition probabilities;

(j) laser polarisation measurement on Eu^{3+} and Tb^{3+} doped ZnO crystals to determine the exact lattice site location of the RE^{3+} ion in the ZnO matrix, and

(k) Hall-effect and conductivity experiments to characterize the conductivity of ZnO thin films (i.e. n-type or p-type).

References

[1] Li Y L, Lee D Y, Min S R, Cho H N, Kim J and Chung C W, "Effect of oxygen concentration on properties of indium zinc oxide thin films for flexible dye-sensitized solar cell," *Jpn. J. Appl. Phys.*, vol. 47, no. 8, pp. 6896-6899, 2008.

[2] Kumar V, Som S, Kumar V, Kumar V, Ntwaeaborwa O M , Coetsee E and Swart H C, "Tunable and white emission from ZnO: Tb^{3+} nanophosphors for solid state lighting applications," *Chem. Eng. J.*, vol. 255, pp. 541 - 552, 2014.

[3] Reynolds D C, Look D C, and Jogai B, "Optically pumped ultraviolet lasing from ZnO," *Solid State Comm.*, vol. 99, no. 12, pp. 873-875, 1996.

[4] Auret F D, Goodman S A, Hayes M, Legodi M J, van Laarhoven H A and Look D C, "Electrical characterisation of 1.8 MeV proton-bombarded ZnO," *Appl. Phys. Lett.*, vol. 79, no. 19, pp. 3074-3076, 2001.

[5] Triboulet R, "Growth of ZnO bulk crystals: A review," *Progress in Crystal Growth and Characterisation of Materials* , vol. 60 , pp. 1–14, 2014.

[6] Chen Y, Bagnall D M, Koh H, Park K, Hiraga K, Zhu Z and Yao T, "Plasma assisted molecular beam epitaxy of ZnO on c-plane sapphire: Growth and characterisation," *J. Appl. Phys.*, vol. 84, no. 7, pp. 3912-3918, 1998.

[7] Look D C, "Recent advances in ZnO materials and devices," *Mat. Sci. Eng.* , vol. B56, pp. 1-5, 2000.

[8] Ellmer K, "Magnetron sputtering of transparent conductive zinc oxide: relation between the sputtering parameters and the electronic properties.," *J. Phys. D: Appl. Phys.*, vol. 33, pp. R17-R32, 2000.

[9] Koao L F, Dejene F B, Kroon R E, and Swart H C, "Effect of Eu^{3+} on the structure, morphology and optical properties of flower-like ZnO synthesized using chemical bath deposition," *J. Lumin.*, vol. 147, pp. 85-89, 2014.

[10] Xu W Z, Ye Z Z, Zeng Y J, Zhu L P, Zhao B H, Jiang L, Lu J G, He H P and Zhang S B, "ZnO light-emitting diode grown by plasma-assisted metal organic chemical vapor deposition," *Appl. Phys. Lett.* , vol. 88, pp. 173506(1-3), 2006.

[11] Chu S, Olmedo M, Yang Z, Kong J and Liu J, "Electrically pumped ultraviolet ZnO diode lasers on Si," *Appl. Phys. Lett.*, vol. 93, pp. 181106(1-3), 2008.

[12] Kohan A F, Cedar G, Morgan D, and Van de Walle C G, "First-principles study of native point defects in ZnO," *Phys. Rev. B*, vol. 61, no. 22, pp. 15019-15027, 2000.

[13] Park S H, Park S E, Lee J C, Song P K and Lee J H, "Photoluminescence characterisation of Al-doped ZnO films deposited by using dc magnetron sputtering," *J. Korean Phys. Soc.*, vol. 54, no. 3, pp. 1344-1347, 2009.

[14] McCluskey M D and Jokela S J, "Defects in ZnO," *J. Appl. Phys.*, vol. 106, pp. 071101(1-13), 2009.

[15] Podhorodecki A, Nyk M, Misiewicz J, and Strek W, "Optical investigation of the emission lines for Eu^{3+} and Tb^{3+} ions in the GaN powder host," *J. Lumin.*, vol. 126, pp. 219-224, 2007.

[16] Pal P P and Manam J, "Photoluminescence and thermoluminescence studies of Tb^{3+} doped ZnO nanrods," *Mat. Sci. Eng. B*, vol. 178, pp. 400-408, 2013.

[17] Zhang J, Feng H, Hao W, and Wang T, "Luminescent properties of ZnO sol and film doped with Tb^{3+} ion," *Mat. Sci. Eng. A*, vol. 425, pp. 346-348, 2006.

[18] Wang D, Xing G, Gao M, Yang L, Yang J and Wu T, "Defects-mediated energy transfer in red-light-emitting Eu-doped ZnO nanowire arrays," *J. Phys. Chem. C*,

vol. 115, pp. 22729-22735, 2011.

[19] Teke A, Ozgur U, Dogan S, Gu X, Morkoc H, Nemeth B, Nause J and Everitt H O, "Excitonic fine structure and recombination dynamics in single-crystalline ZnO," *Phys. Rev. B*, vol. 70, pp. 195207(1-10), 2004.

[20] Rosa A M, da Silva E P, Amorim E, Chaves M, Catto A C, Lisboa-Filho P N and Bortoleto J R R, "Growth evolution of ZnO thin films deposited by rf magnetron sputtering," *J. Phys.: Conference series*, vol. 370, pp. 012020(1-7), 2012.

[21] Janotti A and Van de Walle C G, "Fundamentals of zinc oxide as a semiconductor," *Rep. Prog. Phys.*, vol. 72, pp. 126501(1-29), 2009.

[22] Lannoo M and Bourgoin J, *Point defects in semiconductors I: theoretical aspects*. Berlin: Springer, 1981.

[23] Vlasenko L S and Watkins G D, "Optical detection of electron paramagnetic resonance in room-temperature electron-irradiated ZnO," *Phys. Rev. B.*, vol. 71, pp. 125210(1-6), 2005.

[24] Pan Z, Ueda A, Xu H, Hark S K, Morgan S H and Mu R, "Photoluminescence of Er-doped ZnO nanoparticle films via direct and indirect excitation," *J. Nanoparticles*, vol. 6, pp. 063508(1-11), 2012.

[25] Lumb M D, *Luminescence spectroscopy*. New York: Academic press, 1978.

[26] Sole J G, Bausa L E, and Jaque D, *An introduction to the optical spectroscopy of inorganic solids*. West Sussex: John Wiley and Sons, 2005.

[27] Callister W D, *Materials science and engineering an introduction*, 7th ed. New York: John Wiley & Sons, Inc., 2007.

[28] Ashcroft N W and Mermin N D, *Solid state Physics*. Tokyo: CBS publishing Japan, LTD, 1976.

[29] Srivastava A K and Kumar J, "Effect of zinc addition and vacuum annealing time on the properties of spin-coated low-cost transparent conducting 1 at% Ga-ZnO thin films," *Sci. Technol. Adv. Mater.*, vol. 14, pp. 1-15, 2013.

[30] Hong R, Huang J, He H, Fan Z, and Shao J, "Influence of different post-treatments on the structure and optical properties of zinc oxide thin films," *Applied Surface Science* , vol. 242 , pp. 346–352, 2005.

[31] Look D C, Hemsky J W, and Sizelove J R , "Residual native shallow donor in ZnO," *Phys. Rev. Lett.*, vol. 82 , no. 12, 1999.

[32] Zhang S B, Wei S H, and Zunger A, "Intrinsic n-type versus p-type doping asymmetry and the defect physics of ZnO," *Phys. Rev. B.* , vol. 63, pp. 075205(1-7).

[33] Ziegler E, Heinrich A, Oppermann H, and Stover G, "Electrical properties and non-stoichiometry in ZnO single crystals," *Phys. Stat. Sol.*, (a) vol. 66, pp. 635-648, 1981.

[34] Kasai P H , "Electron spin resonance studies of donors and acceptors in ZnO," *Phys. Rev.* , vol. 130, no. 3, pp. 989-995, 1963.

[35] Park C H, Zhang S B, and Wei S H, "Origin of p-type doping difficulty in ZnO: The impurity perspective," *Phys. Rev. B* , vol. 66, pp. 073202(1-3) , 2002.

[36] Tan S T, Chen B J, Sun X W, Yu M B, Zhang X H , and Chua S J , "Realization of intrinsic p-type ZnO thin films by metal organic chemical vapor deposition," *J. Elect. Mat.*, vol. 34, no. 8, pp. 1172-1176, 2005.

[37] Dai L P, Deng H, Chen J J, and Wei M , "Realization of the intrinsic p-type ZnO thin film by SSCVD," *Solid State Communications* , vol. 143, pp. 378–381, 2007.

[38] Ilyas U, Rawat R S , Tan T L , Lee P., Chen R, Sun H D, Fengji L, and Zhang S ,

"Oxygen rich p-type ZnO thin films using wet chemical route with enhanced carrier concentration by temperature-dependent tuning of acceptor defects," *J. Appl. Phys.* , vol. 110 , pp. 093522 (1-7), 2011.

[39] Kang H S , Kang J S, Kim J W, and Lee S Y , "Annealing effect on the property of ultraviolet and green emissions of ZnO thin films," *J. Appl. Phys.*, vol. 95, no. 3, pp. 1246-1250, 2004.

[40] Menon R, Gupta V, Tan H H, Sreenivas K , and Jagadish C, "Origin of stress in radio frequency magnetron sputtered zinc oxide thin films," *J. Appl. Phys.*, vol. 109, pp. 064905(1-6), 2011.

[41] Janotti A and Van de Walle C G, "Native point defects in ZnO," *Phys Rev B* , vol. 76, pp. 165202(1-22), 2007.

[42] Kittel C, *Introduction to solid state physics*, 8th ed. New York: Wiley, 2005.

[43] Oba F, Choi M, Togo A, and Tanaka I, "Point defects in ZnO: an approach from first principles," *Sci. Technol. Adv. Mater.* , vol. 12 , pp. 034302(1-14), 2011.

[44] Xu P S , Sun Y M, Shi C S, Xu F Q , and Pan H B, "The electronic structure and spectral properties of ZnO and its defects," *Nucl. Instr. and Meth. in Phys. Res. B.* , vol. 199 , pp. 286–290, 2003.

[45] Montenegro D N , Hortelano V , Martınez O , Martınez-Tomas M C , Sallet V, Munoz-Sanjose V , and Jimenez J , "Non-radiative recombination centres in catalyst-free ZnO nanorods grown by atmospheric-metal organic chemical vapour deposition," *J. Phys. D: Appl. Phys.*, vol. 46 , pp. 235302(1-4), 2013.

[46] Chichibu S F , Uedono A, Tsukazaki A , Onuma T, Zamfirescu M , Ohtomo A, Kavokin A , Cantwell G , Litton C W , Sota T, and Kawasaki M , "Exciton–polariton spectra and limiting factors for the room-temperature photoluminescence efficiency in ZnO," *Semicond. Sci. Technol.* , vol. 20 , pp. S67–S77, 2005.

[47] Stavale F, Nilius N, and Freund H J, "STM luminescence spectroscopy of intrinsic defects in ZnO (0001) thin films ," *J. Phys. Chem. Lett.*, vol. 4, pp. 3972-3976, 2013.

[48] Atkins P W, Overton T L, Rourke J P, Weller M T, and Armstrong F A, *Shriver and Atkins inorganic chemistry*, 5th ed. New York: Oxford university press, 2010.

[49] Hufner S, *Optical spectra of transparent rare earth compounds*. New York: Academic Press, 1978.

[50] Klampaftisa E, Ross D, McIntosh K R, and Richards B S , "Enhancing the performance of solar cells via luminescent down-shifting of the incident spectrum: A review ," *Solar energy materials and solar cells*, vol. 93, pp. 1182-1194, 2009.

[51] Yang J, Li X, Lang J, Yang L, Wei M, Gao M , Liu X, Zhai H, Wang R, Liu Y, and Cao J, "Synthesis and optical properties of Eu-doped ZnO nanosheets by hydrothermal method," *Materials Science in Semiconductor Processing*, vol. 14, pp. 247-252, 2011.

[52] Badalawa W, Matsui H, Osone T, Hasuike N, Harima H, and Tabata H, "Correlation between structural and luminescent properties of Eu^{3+}-doped ZnO epitaxial layers," *J. Appl. Phys.*, vol. 109, pp. 053502(1-7), 2011.

[53] Liu G and Jacquier B, *Spectroscopic properties of rare earths in optical materials*. Berlin: Springer, 2010.

[54] Wybourne B G and Smentek L, *Optical spectroscopy of Lanthanides magnetic and hyperfine interactions*. Boca Raton: CRC Press, 2007.

[55] Atkins P and de Paula J , *Atkins' physical chemistry*, 8th ed. New York: Oxford Press, 2006.

[56] Wybourne B G, *Spectroscopic properties of rare earths*. New York: Interscience, 1965.

[57] Pereira A S, Peres M, Soares M J, Alves E, Neve A, Monteiro T and Trindade T, "Synthesis, surface modification and optical properties of terbuim-doped ZnO nanocrystals," *Nanotechnology*, vol. 17, pp. 834-839, 2006.

[58] Koster G, Dimmock J O, Wheeler R G, and Statz H, *Properties of the thirty-two point groups*. Cambridge: M.I.T press, 1963.

[59] Zhang X L , Hui K N, Hui K S, and Singh J, "Structural and optical characterisation of high-quality ZnO thin films deposited by reactive rf magnetron sputtering," *Materials Research Bulletin*, vol. 48, pp. 1093–1098, 2013.

[60] John R and Rajakumari R, "Synthesis and characterisation of rare earth ion doped nano ZnO," *Nano-Micro Lett.*, vol. 4 , no. 2 , pp. 65-72 , 2012.

[61] Shinde K N , Dhoble S J, Swart H C, and Park K, *Phosphate phosphors for solid-state lighting*. Berlin: Springer, 2012, vol. 174.

[62] Koao L F, Dejene F B, and Swart H C, "Properties of flower-like ZnO nanostructures synthesized using the chemical bath deposition," *Mat. Sci. in semiconductor processing*, vol. 27, pp. 33-40, 2014.

[63] Ohring M, *Materials science of thin films deposition and structure*, 2nd ed. Orlando: Academic press, 2002.

[64] Shan F K, Liu G X, Liu Z F , Lee W J, Lee G H, Kim I S, Shin B C , and Yu Y S, "Optical characterisations of ZnO thin films on Si (100) substrates deposited by pulsed laser deposition," *J. Korean Phys. Soc.*, vol. 45, pp. S771-S775, 2004.

[65] Lupan O, Pauporte T, Chow L, Viana B, Pelle F, Ono L K , Roldan Cuenya B, and Heinrich H, "Effects of annealing on properties of ZnO thin films prepared by electrochemical deposition in chloride medium," *Applied Surface Science* , vol. 256 , pp. 1895–1907, 2010.

[66] Koao L F, "Private communication".

[67] Goldstein J I, Lyman C E, Newbury D E, Lifshin E, Echlin P, Sawyer L, Joy D C, and Michael J R, *Scanning electron micrsoscopy and x-ray microanalysis*. New York: Springer science and bussines media, 2003.

[68] Cullity B D and Stock S R, *Elements of X-ray difraction*, 3rd ed. New jersey: Prentice Hall, 2001.

[69] Milathianaki D, Hawreliak J, McNaney J M , El-Dasher B S , Saculla M D, Swift D C, Lorenzana H E , and Ditmire T , "A Seeman–Bohlin geometry for high-resolution nanosecond x-ray diffraction measurements from shocked polycrystalline and amorphous materials," *Rev. Sci. Instrum.*, vol. 80, pp. 093904 (1-7), 2009.

[70] Dutta P, "Grazing incidence X-ray diffraction," *Current Science*, vol. 78, no. 12, pp. 1478-1483, 2000.

[71] Kumar V , Swart H C, Kumar V, Pandey A, Purohit L P , and Ntwaeaborwa O M , "Effect of doping on ZnO based trasparent conducting oxides and down/up conversion phosphor for solar cell application," in *Third Southern African Solar Energy Conference*, Kruger National Park, South Africa, 2015, pp. 476-480.

[72] Das R , Khichar N , and Chawla S , "Dual mode luminescence in rare earth (Er^{3+}/Ho^{3+}) doped ZnO nanoparticles fabricated by inclusive co precipitation technique," *J. Mater. Sci: Mater. Electron*, vol. 26 , pp. 7174–7182, 2015.

[73] Ahn C H, Kim Y Y, Kim D C, Mohanta S K, and Choa H K, "A comparative analysis of deep level emission in ZnO layers deposited by various methods," *J Appl. Phys.*, vol. 105, pp. 013502(1-5) , 2009.

[74] Nadarajah K, Chee C Y , and Tan C Y , "Influence of annealing on properties of spray deposited ZnO thin films," *Journal of Nanomaterials*, vol. 2013, pp. 1-8, 2013.

[75] Nkhaili L, El kissani A, Ait Ali M, Ijdiyaou Y, Elmansouri A, Elkhalfi A, and Outzourhit A, "Effect of RF power on the structural and optical properties of RF-sputtered ZnO thin films," *Eur. Phys. J. Appl. Phys.* , vol. 66, pp. 30302(1-5), 2014.

[76] Yu H, Wang J, Yan Y, Wang X, Gao B, Liu H, and Du Y, "ZnO thin films produced by the rf magnetron sputtering," in *International Conference on Electronic & Mechanical Engineering and Information Technology*, 2011, pp. 2486-2489.

[77] Kim C, Kim S, and Lee C, "Effects of rf power and substrate temperature during rf magnetron sputtering on crystal quality of ZnO thin films," *Japanese J. Appl. Phys.*, vol. 44, no. 12, pp. 8501–8503, 2005.

[78] Flickyngerova S, Shtereva K, Stenova V, Hasko D, Novotny I, Tvarozek V, Sutta P , and Vavrinsky E, "Structural and optical properties of sputtered ZnO thin films," *Applied Surface Science* , vol. 254 , pp. 3643–3647, 2008.

[79] Ma H L, Hao X, Ma J, Yang Y, Huang S, Chen F, Wang Q, and Zhang D, "Bias voltage dependence of properties for ZnO:Al films deposited on flexible substrate," *Surface and Coatings Technology*, vol. 161, pp. 58–61, 2002.

[80] Lu Y M, Hwang W S, Liu W Y, and Yang J S, "Effect of rf power on optical and electrical properties of ZnO thin film by magnetron sputtering," *Materials Chemistry and Physics*, vol. 72, pp. 269–272, 2001.

[81] Ziani A, Davesnne C, Labbe C, Cardin J, Marie P, Frilay C, Boudin S and Portier X, "Aneealing effects on the photoluminescence of terbium doped zinc oxide films," *Thin Solid Films*, vol. 553, pp. 52-57, 2014.

[82] Morkoc H and Ozgur U, *Zinc oxide fundamentals, materials and device technology*. Weinheim: WILEY-VCH, 2009.

[83] Kisi E H and Elcombe M M, "u parameters for the wurtzite structure of ZnS and ZnO using powder neutron diffraction," *Acta Cryst.*, vol. C45, pp. 1867-1870, 1989.

[84] Wu L, Wu Y, Pan X, and Kong F, "Synthesis of ZnO nanorod and the annealing effect on its photoluminescence property," *Opt. Mat.*, vol. 28, pp. 418-422, 2006.

[85] Tam K H, Cheung C K, Leung Y H, Djurisic A B, Ling C C, Beling C D, Fung S , Kwok W M, Chan W K, Philips D L, Ding L, and Ge W K, "Defects in ZnO nanrods prepared by hydrothermal method," *J. Phys. Chem. B*, vol. 110, pp. 20865-20871, 2006.

[86] Liu M, Kitai A H, and Mascher P, "Point defects and luminescence centres in zinc oxide and zinc oxide doped with manganese," *J. Lumin.*, vol. 54, pp. 35-42, 1992.

[87] Kim J, Meng J, Lee D, Yu M, Yoo D, Kang D W, and Jo J, "ZnO thin-film transistor grown by rf sputtering using carbon," *Journal of Nanomaterials*, vol. 2014, pp. 1-7, 2014.

[88] Tu M, Su Y, and Ma C, "Nitrogen-doped p-type ZnO films prepared from nitrogen gas radio-frequency magnetron sputtering," *J. Appl. Phys.*, vol. 100, pp. 053705(1-4), 2006.

[89] Yang L, Tang Y, Hu A, Chen X, Liang K and Zhang L, "Raman scattering and luminescence study on arrays of ZnO doped with Tb^{3+}," *Phys. B*, vol. 403, pp. 2230-2234, 2008.

[90] Luo L, Huang F Y, Dong G S, Fan H H, Li K F, Cheah K W, and Chen J, "Strong luminescence and efficient energy transfer in Eu^{3+}/Tb^{3+}-codoped ZnO nanocrystals,"

Opt. Mat., vol. 37, pp. 470–475, 2014.

[91] Koao L F, Dejene F B, Swart H C, and Botha J R, "The effect of Ce^{3+} on structure, morphology and optical properties of flower-like ZnO synthesized using the chemical bath method," *J. Lumin*. vol. 143, pp. 463-468, 2013.

[92] Mote V D, Purushomtham Y, and Dole B N, "Williamson-Hall analysis in estimation of lattice strain in nanometer-sized ZnO particles," *J. Theoretical and App. Phys.* , vol. 6, no. 6, pp. 1-8, 2012.

[93] Goncalves N S, Carvalho J A, Lima Z M, and Sasaki J M, "Size-strain study of NiO nanoparticles by x-ray powder diffraction line broadening," *Mat. lett.*, vol. 72, pp. 36-38, 2012.

[94] Zhang Y, Liu Y, Wu L, Xie E, and Chen J, "Photoluminescence and ZnO→Eu^{3+} energy transfer in Eu^{3+}-doped ZnO nanospheres," *J. Phys. D: Appl. Phys.*, vol. 42, pp. 085106(1-6), 2009.

[95] Kushida T, "Site-selective flourescence spectroscopy of Eu^{3+} and Sm^{2+} ions in glasss," *J. Lumin.*, vol. 100, pp. 73-88, 2002.

[96] Gruber J B, Vetter U, Taniguchi T, Burdick G W, Hofsass H, Chandra S and Sardar D K, "Spectroscopic analysis of Eu^{3+} in single-crystal hexagonal phase AIN," *J. Appl. Phys.*, vol. 110, pp. 023104(1-7), 2011.

[97] Davesnne C, Ziani A, Labbé C, Marie P, Frilay C, and Portier X, "Energy transfer mechanism between terbium and europium ions in zinc oxide and zinc silicates thin films," *Thin Solid Films*, vol. 553 , pp. 33–37, 2014.

[98] Lima S A M, Sigoli F A, Jafelicci Jr M, and Davolos M R, "Luminescent properties and lattice defects correlation on zinc oxide," *International Journal of Inorganic Materials*, vol. 3, pp. 749–754, 2001.

Publication

Bhebhe N A, Mujaji M, Wamwangi D, Koao L F and Dejene F B, Laser excitation studies and crystal-field analysis of ZnO:Tb^{3+} and ZnO:Eu^{3+} powders, *in The Proceedings of the 60th Annual Conference of the South African Institute of Physics (SAIP2015)*, edited by Makaiko Chithambo (RU) and André Venter (NMMU) (2015), pp. 14-19. ISBN: 978-0-620-70714-5.

Conference presentations

1. "Laser excitation studies and crystal-field analysis of ZnO:Tb^{3+} and ZnO:Eu^{3+} powders" (Oral), *DST-NRF Centre of Excellence in Strong Materials annual students workshop*, University of the Witwatersrand, Johannesburg , South Africa, 2015.
2. "Laser excitation studies and crystal-field analysis of ZnO:Tb^{3+} and ZnO:Eu^{3+} powders" (Poster), *60^{th} South African Institute of Physics Conference*, Port Elizabeth, South Africa, 2015.